Vertical Axis Wind Turbine Acoustics

Charlie Pearson

Corpus Christi College

Cambridge University Engineering Department

A thesis submitted for the degree of

Doctor of Philosophy

September 2013

Declaration

Described in this dissertation is work performed in the Acoustics Laboratory of the Department of Engineering, University of Cambridge between October 2010 and September 2013. I hereby declare that no part of this work has been submitted as an exercise for a degree at this or any other university. This dissertation is entirely the result of my own work and includes nothing which is the outcome of collaboration. This dissertation contains approximately 80 figures and 45,000 words.

Signed:

Dated:

Acknowledgements

First and foremost I would like to thank my supervisor, Dr Will Graham, for the help he has provided over the last three years. I have learnt a great deal about how to do quality, robust research work during my PhD and this is almost entirely thanks to his input. The duration of my PhD has been greatly shortened by having sat next to Sam Sinayoku who knows the answers to many questions about acoustics, computing, LaTeX and all manner of other topics. Ulf Narloch also needs to be thanked for his first hand demonstration of how German efficiency can be applied to the writing of PhDs.

Tamás Bertényi has to be mentioned as he helped to set up this project, and without his input my wind tunnel model would never have worked. Despite having left my sponsor, QuietRevolution Ltd, he has continued to help me out with his invaluable wealth of knowledge about VAWTs. Another group of people who have helped make this project happen are the CUED technicians. They have helped to solve a whole range of practical problems, and put up with my periodic incompetence.

I also need to thank my parents for all their support over the last 26 years. I hope that Dad feels that this thesis, which could be considered to be the culmination of my education, constitutes a suitable return on investment.

Finally I need to thank Breeshey Harkin for putting up with me for the last three years, and for at least pretending to listen to my enthusiastic lectures about a whole range of engineering topics. She has also battled her way through the proof reading of a number of the chapters in this thesis, which is no mean feat.

Abstract

Increasing awareness of the issues of climate change and sustainable energy use has led to growing levels of interest in small-scale, decentralised power generation. Small-scale wind power has seen significant growth in the last ten years, partly due to the political support for renewable energy and the introduction of Feed In Tariffs, which pay home owners for generating their own electricity.

Due to their ability to respond quickly to changing wind conditions, small-scale vertical axis wind turbines (VAWTs) have been proposed as an efficient solution for deployment in built up areas, where the wind is more gusty in nature. If VAWTs are erected in built up areas they will be inherently close to people; consequently, public acceptance of the turbines is essential. One common obstacle to the installation of wind turbines is noise annoyance, so it is important to make the VAWT rotors as quiet as possible.

To date, very little work has been undertaken to investigate the sources of noise on VAWTs. The primary aim of this study was therefore to gather experimental data of the noise from various VAWT rotor configurations, for a range of operating conditions. Experimental measurements were carried out using the phased acoustic array in the closed section Markham wind tunnel at Cambridge University Engineering Department. Beamforming was used in conjunction with analysis of the measured sound spectra in order to locate and identify the noise sources on the VAWT rotors.

Initial comparisons of the spectra from the model rotor and a full-scale rotor showed good qualitative agreement, suggesting that the conclusions from the experiments would be transferable to real VAWT rotors. One clear feature observed in both sets of spectra was a broadband peak around 1-2kHz, which spectral scaling methods demonstrated was due to laminar boundary layer tonal noise. Application of boundary layer trips to the inner surfaces of the blades on the model rotor was found to eliminate this noise source, and reduced the amplitude of the spectra by up to 10dB in the region of the broadband peak. This method could easily be applied to a full-scale rotor and should result in measurable noise reductions.

At low tip speed ratios (TSR) the blades on a VAWT experience dynamic stall and it was found that this led to significant noise radiation from the upstream half of the rotor. As the TSR was increased the dominant source was seen to move to the downstream half of the rotor; this noise was thought to be due to the

interaction of the blades in the downstream half of the rotor with the wake from the blades in the upstream half. It was suggested that blade wake interaction is the dominant noise source in the typical range of peak performance for the full-scale QR5 rotor. Different solidity rotors were investigated by using 2-, 3- and 4-bladed rotors and it was found that increasing the solidity had a similar effect to increasing the TSR. This is due to the fact that the induction factor, which governs the deflection of the flow through the rotor, is a function of both the rotor solidity and the TSR.

With a large body of experimental data for validation, it was possible to investigate computational noise prediction methods. A harmonic model was developed that aimed to predict the sound radiated by periodic fluctuations in the blade loads. This model was shown to agree with similar models derived by other authors, but to make accurate predictions very high resolution input data was required. Since such high resolution blade loading data is unlikely to be available, and due to the dominance of stochastic sources, the harmonic model was not an especially useful predictive tool. However, it was used to investigate the importance of the near-field components of the sound radiated by the wind tunnel model to the acoustic array. It was shown that the near-field terms were significant over a wide range of frequencies, and the total spectrum was always greater than that of the far-field component. This implied that the noise levels measured by the acoustic array represented an upper bound on the sound radiated to the far-field, and hence that the latter would also be dominated by stochastic components.

An alternative application of the harmonic model, which attempted to determine the blade loading harmonics from the harmonics in the sound field was proposed. This inversion method utilised a novel convex optimisation technique that was found to generate good solutions in the simulated test cases, even in the presence of significant random noise. The method was found to be insensitive at low frequencies, which made it ineffective for inverting the real microphone data, although this was shown to be at least partly due to the limitations imposed by the array size.

In addition to the harmonic models, an empirical noise prediction method using the spectral scaling laws derived by Brooks, Pope, and Marcolini [1989] was trialled, and was found to be capable of making predictions that were in agreement with the measured data. The model was shown to be sensitive to the exact choice of turbulence parameters used and was also found to require good quality aerodynamic data to make accurate noise predictions. If such data were available however, it is expected that this empirical model would be able to make useful predictions of the noise radiated by a VAWT rotor.

Contents

List of Figures

List of Tables

Nomenclature

Roman Symbols

A Rotor swept area

a Induction factor

a_0 Speed of sound

B Number of blades on rotor

c Blade chord length (m)

C_p Turbine power coefficient

C_{mn} Cross spectral matrix of microphones m and n

$\bar{D}_h$ High-frequency directivity function

$\bar{D}_l$ Low-frequency directivity function

f Frequency

F_i Force in Cartesian coordinates ($i = 1, 2, 3$)

F_s Sampling frequency

g_m Steering function for microphone m

J_n Bessel function of order n

k Reduced frequency, $k = \pi f c / U_\infty$

L Blade span

M_B Absolute blade Mach number

M_r Mach number in the direction of the observer

p Air pressure

P_m Complex spectrum of microphone m

p_{ij} Fluid stress tensor

r Distance from source to observer

R_0 Rotor radius

r_e Distance from source emission location to observer

Re_c Chord based Reynolds number

St Strouhal number

t Observer time coordinate

T_{ij} Lighthill's stress tensor

U Fluid velocity

u_i Unsteady component of the velocity

x_i Cartesian observer coordinates $(i = 1, 2, 3)$

$\underline{x}_m$ Location of microphone m

y_i Cartesian source coordinates $(i = 1, 2, 3)$

Greek Symbols

α Blade angle of attack

β Blade preset pitch angle

δ_p Pressure surface boundary layer thickness

δ_{ij} Kronecker delta function, $\delta_{ij} = 0$ if $i \neq j$, else $\delta_{ij} = 1$

θ Blade azimuth

ν Kinematic viscosity

ξ Location of scanning grid point

ρ Density

σ Rotor solidity, $\sigma = Bc/R_0$

τ Source time, also known as retarded time

ϕ Observer azimuth

Ω Rotor angular velocity (rad/s)

Subscripts

∞ Free-stream value

B Blade absolute value

rel Blade relative value

Acronyms

BPM   Brooks, Pope and Marcolini

BVI   Blade Vortex Interaction

CSM   Cross Spectral Matrix

CVX   ConVeX optimisation functions

FFT   Fast Fourier Transform

HAWT Horizontal Axis Wind Turbine

LBL-VS Laminar Boundary Layer - Vortex Shedding

SPL   Sound Pressure Level

TBL-TE Turbulent Boundary Layer - Trailing Edge

TEB-VS Trailing Edge Bluntness - Vortex Shedding

TSR   Tip Speed Ratio

TV-FORM Tip Vortex FORMation

VAWT Vertical Axis Wind Turbine

VTM   Vorticity Transport Model

Chapter 1

Introduction

The world is currently facing major energy challenges. With growing pressure on resources and concerns about global climate change, there is a strong urge to move away from fossil fuel driven economies to a more sustainable energy supply with renewable power at its core. The UK has embodied its ambition for more green power generation in a series of legally binding obligations to reduce emissions and increase the use of low carbon energy sources. The 2008 Climate Change Act established the world's first ever legally binding climate change targets and committed the UK to reducing its carbon emissions by 2050 by at least 80% relative to 1990 levels [UK Government, 2008]. In addition, the UK is now also legally committed to generating 15% of its electricity from renewable sources by 2020.

In 2011 27% of the UK's carbon emissions were from electricity generation and it is forecast that, with increased electrification of transport and heating, the demand for electricity will increase by up to 60% by 2050 [UK Department of Energy and Climate Change, 2011, p.9]. To meet the anticipated demand for electricity, whilst simultaneously reducing carbon emissions, will require substantial changes in way that the UK generates its electricity and this will almost certainly imply a large role for renewable generation.

It has long been understood that the wind contains a significant amount of energy. Sailing boats have used this energy for millennia, and simple wind turbines for the grinding of grain or the pumping of water have existed for centuries. Extending this technology to the generation of electricity was a natural step, and the pre-existing knowledge of wind power has helped wind turbines to become one of the dominant sources of renewable power generation. In the UK in 2011, wind power contributed 47.8% of the renewable electricity supplied to the grid, although it is important to recognise that this still only constituted 4.45% of total electricity generation in the UK [UK Department of Energy and Climate Change, 2012].

Figure 1.1: Growth in installed wind generating capacity in the UK over the last 12 years [Renewable UK, 2012b].

The UK has the best wind resource of any country in Europe [Renewable UK, 2012a, p.3] and, with the support of government subsidies, has seen rapid growth in the amount of installed wind generating capacity (see figure 1.1). Virtually all of this growth has been from large wind farms: at the end of 2012 there was only 65MW of installed capacity from wind turbines smaller than 500kW. This equates to nearly 20,000 small turbines [Renewable UK, 2012a], however, which is far more than the 5000 large scale turbines currently operating in the UK [Renewable UK, 2013]. This means that, in terms of public perception, small wind turbines may have a disproportionately high profile.

Small scale wind turbines are typically designed for local or domestic use, which tends to mean that they are installed in close proximity to people's homes or places of work; it is also not unusual for these turbines to be directly mounted on buildings. Public acceptance is essential to make such installations possible, which is why it is necessary to have a good understanding of the noise radiated by small wind turbines.

1.1 Extracting Energy From the Wind

Before considering the noise output from a wind turbine, it is necessary to have an appreciation of the aerodynamic performance, since this is often the primary objective in the design of a wind turbine rotor. The detail of the flow through the rotor is also directly responsible for the noise radiation. The discussion of exactly how the aerodynamic noise is generated is a lengthy subject and is addressed in chapter 2.

It has long been understood that a moving fluid contains energy that, with

Figure 1.2: Schematic of the parameters used in the derivation of the Betz limit

the correct machinery, can be converted into useful work. Exactly how much power is contained in the wind can be determined by considering the flow of air through a control surface of area A. Kinetic energy per unit volume in the flow is defined as in equation 1.1.

$$E_{kinetic} = \frac{1}{2}\rho U_\infty^2 \qquad \text{Kinetic Energy per unit volume} \qquad (1.1)$$

$$P_{kinetic} = \frac{1}{2}\rho A U_\infty^3 \qquad \text{Energy flux of fluid passing through } A \qquad (1.2)$$

The kinetic energy flux through area A is therefore given by equation 1.2, and the power of fluid passing through A can be found by integration over this area. Equation 1.2 shows that the energy is proportional to the cube of the velocity, meaning that the amount of available energy in the wind is strongly dependent on the wind speed. As such the siting of turbines in windy locations is essential if they are to produce worthwhile amounts of energy. A further implication of this result is that a high proportion of the energy in a gusty wind may be contained in the high speed, short duration gusts. McIntosh [2009] found that in a typical urban environment, where the winds are gusty in nature, up to 23% of the energy is contained in these short period fluctuations in the wind speed.

By modelling a wind turbine as an actuator disc that extracts energy from the flow (see figure 1.2), Albert Betz showed that there is an upper limit on the amount of energy that can be extracted from a moving fluid [Betz, 1926]. By applying Bernoulli's equation between a point far upstream and the front of the disk and then also between the back of the disk and a point far downstream, one can calculate the pressure drop across the disk. Analysis of a control volume containing the disk then allows the thrust on the rotor to be calculated by considering the momentum loss of the fluid passing through the disk. Equating

this thrust with the pressure drop across the disk, found using Bernoulli's equation, an expression can be derived relating the downstream wind speed to the free stream velocity, in terms of the induction factor a. These results allow an expression to be derived for the power extracted by the actuator disk in terms of the free stream velocity and the induction factor.

$$U_1 = (1-a)U_\infty \qquad \qquad \text{Definition of induction factor, } a \quad (1.3)$$

$$p' = \frac{1}{2}\rho(U_\infty^2 - U_2^2) \qquad \qquad \text{Pressure drop from Bernoulli} \quad (1.4)$$

$$T = \rho A U_1 (U_\infty - U_2) \quad \text{Thrust calculated from momentum balance} \quad (1.5)$$

$$U_2 = (1-2a)U_\infty \qquad \qquad (1.6)$$

$$P_{disk} = 2\rho U_\infty^3 a(1-a)^2 A \qquad \text{Power extracted by actuator disk} \quad (1.7)$$

The actuator disk power can then be normalised by the total available power in the wind to give a power coefficient expressed simply in terms of the induction factor (equation 1.8). Differentiation yields a limit on the power coefficient of $16/27 = 0.59$, which occurs when the induction factor is $a = 1/3$ i.e. when the wind speed at the rotor disk is $2/3$ of the free stream velocity.

$$C_p = \frac{P_{disk}}{1/2\rho U_\infty^3 A} = 4a(1-a)^2 \qquad \qquad (1.8)$$

Wind power devices rotate, and extract power by virtue of the torque exerted by the wind. Both horizontal and lift-type vertical axis wind turbines generate torque by utilising the forces produced when a fluid is deflected by an aerofoil. An appreciation of the aerodynamics of both types of turbine is essential for the discussion of noise generation that follows. As such the details of how each type of rotor produces torque are outlined below.

1.1.1 Horizontal Axis Wind Turbines - HAWTs

A diagram of how an HAWT generates torque is presented in figure 1.3(b). The inflow is assumed to be uniform across the whole rotor disk but the blade velocity is seen to be a function of radius. By setting the blades at an angle of attack to the relative flow velocity a lift force is produced, a component of which is in the direction of motion of the blades, thereby generating torque.

Due to the fact that the blade velocity varies with radius the blade twist angle needs to be continuously varied to maintain a suitable angle of attack along the whole span of the blade. Since the blade is travelling much faster at the tip than near the hub, the blade generates much more force per unit area at the tip. In order to avoid excessive bending moments, the blades are therefore tapered

(a)   RE Power 5MW HAWT   (b)   Diagram of the blade loading on a HAWT rotor showing how torque is generated.
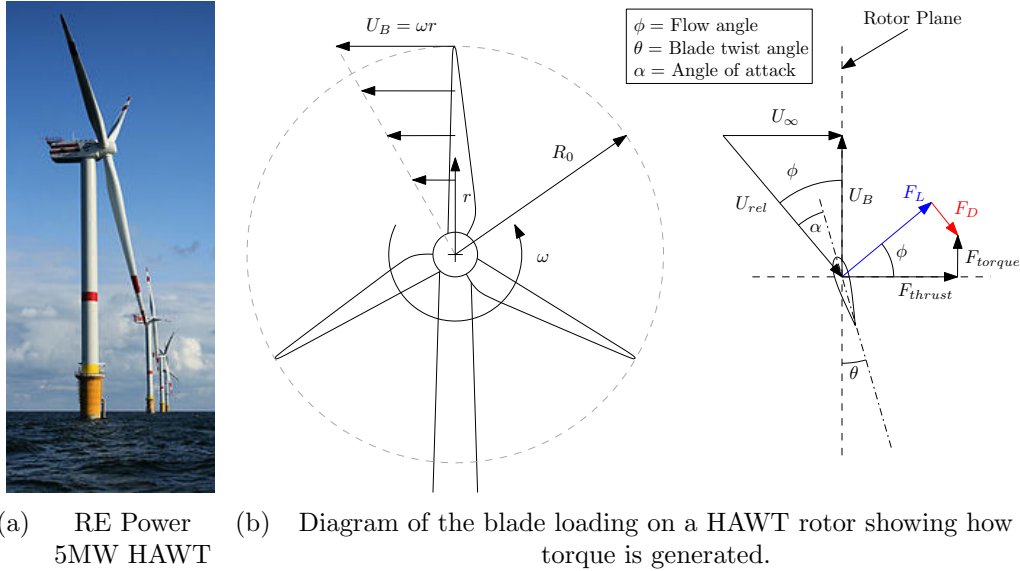
Figure 1.3: Image of a HAWT rotor and a schematic of how torque is generated.

towards the tips. Tapering also helps to reduce the centrifugal loading at the blade root.

It can be assumed that blade angle of attack on a HAWT does not vary as a function of azimuth. It is therefore possible to set the blade twist angle at the optimal angle for maximum power generation at a given wind speed. On most modern rotors this blade pitch angle can be varied during operation to allow the rotor to spin at the best angular velocity for the gearbox and generator. One disadvantage of HAWT rotors is that to increase the rotor power output the blades have to be made increasingly long, and hence increasingly heavy. The high blade mass means that the cyclic fatigue loading due to the blade's self weight can become a major problem. In addition, longer blades tend to have higher tip speeds, which is significant from the point of view of noise generation, as will be discussed later.

1.1.2   Vertical Axis Wind Turbines - VAWTs

There are two principal types of VAWT rotor: lift-type and drag-type. Drag type rotors work by having greater drag on one side of the rotor axis than the other. A well known example of this type of rotor is a cup anemometer. Drag-type rotors are very simple, but the high drag on the half of the rotor which is travelling upstream limits their efficiency. In addition the rotors experience a high level of thrust in the wind direction, which limits their maximum size.
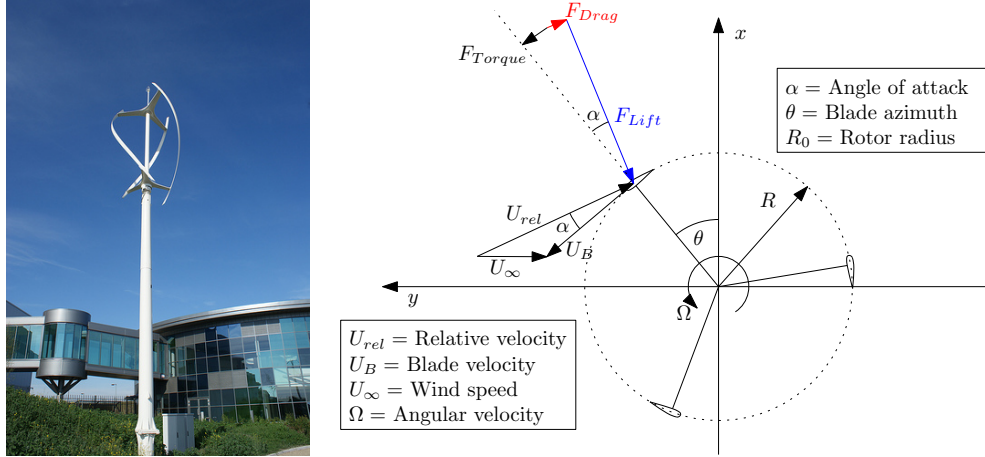
(a) QuietRevolution Ltd
QR5, 7.5kW VAWT

(b) Diagram of the blade loading on a VAWT rotor showing how torque is generated.

Figure 1.4: Image of a VAWT rotor and a schematic of how torque is generated.

Lift-type rotors use aerofoil shaped blades to generate lift, a component of which is in the direction of rotation, thereby producing torque. A diagram showing how this torque is produced is presented in figure 1.4(b). These rotors do not have the problems of drag-type rotors and have been shown to be able to achieve power coefficients similar to HAWTs [Paraschivoiu, 2002].

Unlike HAWT rotors, the angle of attack experienced by the blades on a VAWT is a function of azimuth, with the peak in angle of attack occurring near the most upstream point of the rotation. The fluctuation of the angle of attack is a function of the tip speed ratio (TSR), which is defined as the ratio of the blade tip speed to the wind speed. At lower TSR the angle of attack can exceed the static stall angle, which has a significant impact on rotor performance due to the occurrence of dynamic stall on the blades.

A second important feature of VAWT performance is the influence of the wake from the upstream blades. As the lift on the blades fluctuates they shed vorticity, and this is exacerbated by dynamic stall. At the same time the spanwise variation in the pressure distribution results in a strong tip vortex being formed (see Ferreira [2009]; Scheurich [2011]). The vortical wake is then advected through the rotor volume and subsequently interacts with the blades in the downstream half of the rotation, reducing the blade performance in this region.

6
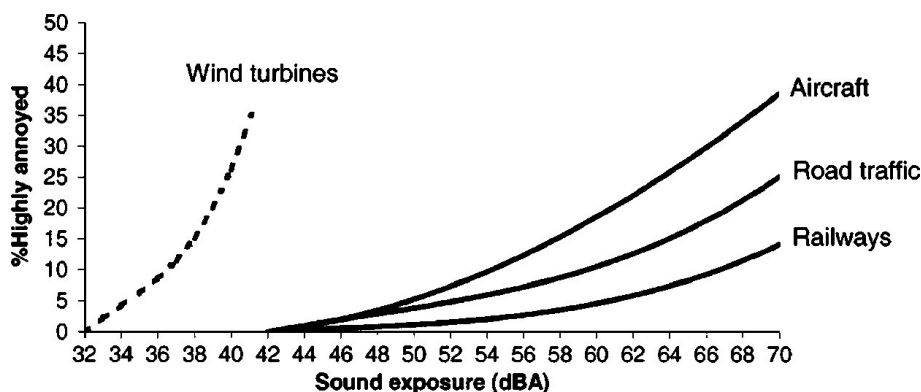
Figure 1.5: Plot showing the proportion of people 'highly annoyed' by different noise sources as a function of the loudness of the sound [Pederson and Waye, 2004]

1.2 Noise Annoyance

In the field of wind turbine noise it is necessary to have an appreciation of the concept of noise annoyance. Measurements of wind turbine noise have often indicated that the sound levels radiated by wind turbines are lower than other sources yet still result in greater annoyance (see figure 1.5, Pederson and Waye [2004]). Studies have generally suggested that the increased annoyance is not related to the noise itself, but to a range of other factors [Bakker et al., 2012; Taylor, 2011]. In particular, an individual's pre-existing attitude towards wind turbines in general was found to be significant, with those having more negative attitudes experiencing greater levels of annoyance. Being able to see the turbine is also an important factor, with people experiencing the same noise level being more likely to complain if they can see a wind turbine.

Perhaps more interestingly, it has been found that those individuals who economically benefit from a wind turbine or wind farm are very unlikely to be annoyed by its noise [Taylor, 2011]. Some wind farm developers in the USA have recognised this effect and have entered into contracts with local residents, known as 'noise easements', to effectively pay for their cooperation [Schiff et al., 2012].

This research tends to suggest that the absolute noise level is not necessarily significant in terms of annoyance. If the noise can be reduced further, however, so that fewer people can hear it at all, the levels of annoyance must surely also be reduced.

1.3 Thesis Objectives

The principal objectives of this study are as follows:

1. At present there is very little experimental data about the noise from VAWTs. The first aim of this study is therefore to fill this gap by collecting noise data from a model-scale VAWT for a range of operating conditions and rotor designs. This data will be collected using an acoustic phased array, which should allow the dominant sources of noise to be located using beamforming methods. From this data set, it is hoped that it will be possible to identify the dominant mechanisms of noise generation.

2. By gaining a better understanding of the noise output from VAWT rotors, it is hoped that a set of design guidelines can be developed. These guidelines will suggest what impact changes in the rotor design and operating condition might have on the levels of noise radiated.

3. A simple computational method for predicting the noise from a VAWT rotor would be an extremely useful design tool. Using the data from the experimental work for model validation, different noise prediction methods will be investigated to establish whether such a tool can be easily developed.

1.4 Thesis Outline

The structure of this thesis is as follows:

Chapter 2 describes the work carried out in the field of aeroacoustics that is relevant to the investigation of the noise from VAWTs. The essential aeroacoustic theory is presented first, followed by a summary of key results from studies of both HAWT noise and helicopter noise.

Chapter 3 explores the available literature relating to the design and performance of VAWT rotors. The potential implications for noise generation are highlighted and the key parameters for investigation in the experimental program are identified.

Chapter 4 details the experimental procedures carried out. The design of the model-scale VAWT rotor is described and the key features of the wind tunnel facility, including the acoustic array, are presented; in particular the beamforming algorithm used is described. The chapter concludes by defining the program of experimental measurements to be carried out.

Chapter 5 presents the results of the experiments, including detailed analysis of both the sound spectra and the beamforming plots. The analysis attempts to identify the mechanisms of noise generation for the different rotor configurations and operating conditions examined.

Chapter 6 describes the computational modelling undertaken. A semi-empirical harmonic method and a fully empirical method are investigated, and their ability to predict the noise from a VAWT rotor is assessed.

Chapter 7 summarises the key conclusions from the study and suggests possible areas for future work in the field of VAWT noise.

Chapter 2

Aeroacoustics Background

The body of existing work relating to VAWT acoustics, and small wind turbine acoustics in general, is very limited. The majority of the work undertaken in the field of aeroacoustics relates to aircraft, of which the most relevant studies are those looking at propeller and helicopter noise. More recently there has been significant interest in noise from horizontal axis wind turbines (HAWTs). This section initially introduces the fundamental elements of aeroacoustic theory relating to the sound field generated by moving surfaces. The key results from investigations of HAWT noise are then presented followed by a summary of the relevant results from studies of helicopter noise. The background theory relating to VAWT performance and noise generation requires more detailed examination and so is presented separately in chapter 3.

2.1 Fundamental Theory

Early work in the field of aeroacoustics principally focused on the characterisation of the frequency components of a sound field. The conclusion of this work was that the frequencies that characterised the flow are the same as those of the resulting sound field. The question of determining the intensity of a sound field was not addressed until 1952 when MJ Lighthill wrote his seminal paper on the prediction of aerodynamic noise.

2.1.1 Lighthill's Acoustic Analogy

Lighthill's key contribution was to reformulate the Navier-Stokes equation as a wave equation with a distinct source term on the right hand side [Lighthill, 1952]. This derivation, known as 'Lighthill's acoustic analogy', is the foundation of virtually all subsequent work in the field of theoretical aeroacoustics:

$$\frac{\partial^2 \rho}{\partial t^2} - a_0^2 \frac{\partial^2 \rho}{\partial x_i^2} = \frac{\partial^2 T_{ij}}{\partial x_i \partial x_j} \qquad (2.1)$$

where $T_{ij} = \rho u_i u_j + p_{ij} - a_0^2(\rho - \rho_0)\delta_{ij}$ is Lighthill's stress tensor.

Lighthill describes three mechanisms by which kinetic energy can be converted into acoustic energy. These are:

1. By forcing the mass in a fixed region of space to fluctuate, as in a loudspeaker diaphragm embedded in a large baffle.

2. By forcing the momentum in a fixed region of space to fluctuate, or, which is the same thing, forcing rates of mass flux across fixed surfaces to vary. Both of these occur when a solid object vibrates after being struck.

3. By forcing the rates of momentum flux across fixed surfaces to vary, as when sound is generated aerodynamically with no fixed boundaries.

These three sources are listed in order of decreasing efficiency of acoustic radiation. Lighthill's original equation (equation 2.1) only deals with the third mechanism, which does not involve any fixed boundaries; this type of source is found to be quadrupole in nature. Since solid boundaries are more efficient radiators of sound, a new formulation that includes their impact must be used when considering the sound generated by a moving, solid body.

2.1.2   Sound Field Generated by a Rigid Body

Curle [1955] used the Kirchoff boundary solution to the inhomogeneous wave equation to develop a method for determining the sound field produced by a rigid body within a flow. A static body can influence a flow in two ways:

1. The sound generated by the free-field quadrupoles can be reflected and diffracted at a solid boundary.

2. The quadrupoles no longer extend over the whole of space but only in that region external to the body. The boundary itself will behave like a combination of dipoles and sources.

Curle's result showed that the sound field could be exactly described by splitting the sources into the quadrupole term derived by Lighthill (assuming no solid boundaries) and a dipole field, which represents the fluctuating force with which the solid boundary acts on the fluid. Curle then used dimensional analysis to

investigate the relative magnitude of Lighthill's quadrupole source and the dipole surface source. The dimensional dependence of the two sound intensities is given below,

$$Quadrupole \propto \rho_0 U_0^8 a_0^{-5} L^2 r^{-2} f(R) \tag{2.2}$$

$$Dipole \propto \rho_0 U_0^6 a_0^{-3} L^2 r^{-2} g(R) \tag{2.3}$$

where U_0 is a typical velocity and L is a typical length scale. The observer is at a distance r from the source.

It can be seen that for flows where the Mach number is low and subsonic, the dipole source is likely to dominate the sound field. The exact definition of what a 'low' Mach number is will depend on the flow in question. In a mathematical sense this is the determined by the relationship between the two functions $f(R)$ and $g(R)$ in equations 2.2 and 2.3.

2.1.3 Sound Field of a Moving Point Source

Lighthill [1962] began investigating the sound generated by moving bodies by modelling the sound field of a point source in uniform rectilinear motion. This yielded the result given below for the fluctuating point force F_i:

$$\rho - \rho_0 = \left[\frac{x_i - y_i}{4\pi a_0^2 r^2 (1 - M_r)^2} \frac{\partial F_i}{\partial t} \right]_{ret} \tag{2.4}$$

where x is the source location, y is the observer location, and M_r is the Mach number in the direction of the observer. ($i = 1, 2, 3$ and the Einstein summation convention is assumed.) A key feature of this expression is the square brackets, which indicate that the terms inside are to be evaluated at the retarded source time. Square brackets are commonly used in this way in aeroacoustic theory and this notation is applied from here on.

Lowson [1965] then extended this work to allow for general motion, which introduced a further term into the equation due to the acceleration of the source. Lowson's result is particularly useful for preliminary investigations of the sound field of a moving source as it maintains many of the key features of the sound field while avoiding unnecessary complexity. This result can only be applied unambiguously for low-subsonic speeds, which is satisfactory in the case of small wind turbines. The equation below is used as the basis of the aeroacoustic model described in chapter 6.

$$\rho - \rho_0 = \left[\frac{x_i - y_i}{4\pi a_0^2 r^2 (1 - M_r)^2} \left\{ \frac{\partial F_i}{\partial t} - \frac{F_i}{1 - M_r} \frac{\partial M_r}{\partial t} \right\} \right]_{ret} \tag{2.5}$$

This equation contains only the far-field terms, which are defined as those terms that decay as $1/r$ rather than $1/r^2$. In order to determine when the far-field terms become dominant it is necessary to understand the near-field terms as well. In the derivation by Lowson [1965], the near-field component was found to be described by equation 2.6.

$$\rho - \rho_0 = \left[\frac{1}{4\pi a_0^2 r^2 (1-M_r)^2} \left\{ \frac{F_i(x_i - y_i)}{r} \frac{(1-M^2)}{(1-M_r)} - F_i M_r \right\} \right]_{ret} \tag{2.6}$$

The overall sound field is simply the sum of the near- and far-field components.

2.1.4 The Ffowcs Williams-Hawkings Equation

The next key contribution to aeroacoustic theory was from Ffowcs Williams and Hawkings [1969] who developed a method for modelling the sound generated by surfaces in arbitrary motion. By defining a generalised function f such that $f = 0$ on the surface of the body and using the conservation equations of fluid mechanics the following result was derived:

$$
\begin{aligned}
\frac{\partial^2 H(f)\rho}{\partial t^2} - a_0^2 \frac{\partial^2 H(f)\rho}{\partial x_i^2} = & \frac{\partial^2}{\partial x_i \partial x_j}[H(f)T_{ij}] - \\
& \frac{\partial}{\partial x_i}\left(p_{ij}\delta(f)\frac{\partial f}{\partial x_j} \right) + \\
& \frac{\partial}{\partial t}\left(\rho_0 v_i \delta(f)\frac{\partial f}{\partial x_i} \right)
\end{aligned}
\tag{2.7}
$$

This is the well-known Ffowcs Williams Hawkings (FW-H) equation and is one of the most commonly used results in aeroacoustic theory. Each of the source terms corresponds to one of the mechanisms of noise generation described by Lighthill [1952].

$\frac{\partial^2}{\partial x_i \partial x_j}[H(f)T_{ij}$ This is the source term due to momentum flux across a fixed surface and does not involve any solid boundaries. This is a quadrupole source as implied by the double space differential.

$\frac{\partial}{\partial x_i}\left(p_{ij}\delta(f)\frac{\partial f}{\partial x_j} \right)$ This is the source term due to fluctuating forces and is often referred to as the loading noise. This is a dipole source as indicated by the single space differential.

$\frac{\partial}{\partial t}\left(\rho_0 v_i \delta(f)\frac{\partial f}{\partial x_i}\right)$ This is the source term due to the displacement of a volume of fluid and is commonly referred to as the thickness noise. This is a monopole source.

It is worth noting that for moving surfaces the definition of monopole and dipole sources can be misleading. It can be shown that the thickness noise from a moving surface is equivalent to the loading noise from a uniform surface pressure distribution of $\rho_0 a_0^2$ [Farassat, 2007]. Some care is therefore required when discussing monopole and dipole sources.

2.1.5 Solutions of the Acoustic Wave Equations

The solution of wave equations, such as the FW-H equation, often relies on the use of generalised functions. A good explanation of how generalised functions can be employed to solve these equations can be found in Jones [1964, p.38 onwards]. In aeroacoustics the general approach to solving the wave equation is to break the source down into a number of discrete point sources. The generalised function that is employed to solve the FW-H equation is then the Green's function of the wave equation in unbounded three-dimensional space. The Green's function for zero mean flow is presented in equation 2.8, with more specialised versions used for more complex cases.

$$G(x_i, t; y_i, \tau) = \delta(\tau - t + r/a_0)/4\pi r \qquad (2.8)$$

where $r = x_i - y_i$. To understand what this function represents, consider the condition $g = \tau - t + r/a_0 = 0$. Rewriting this as $a_0(t - \tau) = |\mathbf{x} - \mathbf{y}|$, the surface can be seen to be a sphere with its centre at the observer location x_i. As the source time increases from $\tau = -\infty$ to $\tau = t$ the radius of the sphere decreases from infinity to zero, with a rate of contraction equal to the speed of sound, a_0. What this collapsing sphere represents is the locus of all the possible sources that could produce a sound that arrives at the observer at observer time t [Farassat, 2007].

The most regularly used solutions of the FW-H equation are formulations 1 and 1A of Farassat and Succi [1975] and Farassat and Succi [1980]. Formulation 1 was the first solution and was subsequently updated to the 1A version, which reorganises the result into a form that can be solved both faster and more accurately by computational methods. It should be noted that the results derived by Farassat only apply to surfaces that are moving subsonically.

Both of these solutions neglect the quadrupole term in the FW-H equation since when a solid boundary is present the monopole and dipole sources are dominant. A detailed and very clear description of how to derive the Farassat

results is given in Farassat [2007]. The solutions themselves do not greatly add to the understanding of the problem so the reader is directed to examine the references if required.

Developing a methodology for predicting the sound using the FW-H equations might yield useful results but, without detailed experimental measurements for validation, would be of little utility. Even if these data were available, a high-resolution aerodynamic simulation would be required to generate the necessary input data, and a version of the Farassat result would have to be implemented to solve the propagation problem for a VAWT. This type of simulation would be a serious undertaking and is beyond the scope of the present study.

2.2 Empirical and Semi-Empirical Noise Prediction Methods

Predicting sound generation by direct computational methods is a challenging problem. For a VAWT it would be necessary to model the global flow through the whole rotor while also resolving the flow over the blades to high enough accuracy to predict the unsteady pressure loading on the blades. The temporal resolution would also have to be sufficiently high to capture the short period fluctuations responsible for high frequency sound. The necessarily high spatial and temporal resolutions make this a computationally expensive process. This scenario is common for many aeroacoustic problems.

In addition to the computational cost, the unsteady pressures are often the result of turbulent flow, which is extremely hard to predict with any accuracy. Consequently it is often impractical to predict noise generation by direct, time domain simulations. As a result of these difficulties, a number of empirical and semi-empirical methods have been developed that attempt to describe the radiation of aerodynamic sound.

2.2.1 Trailing Edge Noise

As turbulence in the flow around an aerofoil passes over the trailing edge, the pressure fluctuations are scattered as noise. This interaction produces a broadband sound, which is believed to be one of the dominant sources of aeroacoustic noise on HAWTs [Oerlemans et al., 2007]. This noise source can be modelled in the time domain using the FW-H equation but accurate predictions require very high resolution aerodynamic inputs. Simulating the turbulence is both difficult and computationally expensive, so other frequency domain methods that attempt to model this sound source have been developed.

The initial analysis of the scattering of sound by a sharp edge was by Ffowcs Williams and Hall [1970]. This derivation employed a Green's function with

no mean flow, but established the key concepts of a trailing edge noise model. The main contribution of this paper was to determine that the amplitude of the noise scattered from the trailing edge scales as the fifth power of the blade Mach number. Another interesting result was that the sound intensity is related to the angle that the mean flow makes with the trailing edge, $\bar{\theta}$, by the factor $\sin^2 \bar{\theta}$. It was therefore suggested that the sound scattered by a sharp edge could be reduced by sweeping the edge relative to the mean flow direction.

The most extensively used trailing edge noise model is that developed by Amiet [1976], which analytically models the far-field power spectral density (PSD) propagated by a known turbulent flow past a sharp edge. A key assumption of this model is that the turbulence is frozen, in that it simply convects over the trailing edge at the mean velocity. This method has proved to be a useful design tool, and has been used in a variety of applications, including the modelling of helicopter noise (e.g. Schlinker and Amiet [1981]) and HAWT noise (e.g. Glegg et al. [1986]).

The key input for this model, and those like it, is the spectrum of the turbulent pressure fluctuation in the flow, and it is common to use a spectrum that represents the self-induced boundary layer turbulence. The estimation of the turbulence spectrum is a purely empirical step and many different forms that attempt to represent different flow conditions have been developed (see Blandeau [2011, section 3.2]).

Amiet [1976] noted that this self-induced boundary layer turbulence is likely to generate a sound that is much quieter than an inflow with 1% turbulence intensity, unless the aerofoil is stalled. The flow around a VAWT blade is likely to be stalled at some point, so it is possible that the scattering of turbulent pressure fluctuations at the trailing edge could significantly contribute to the radiated sound. It is also likely, however, that the blades will experience significant inflow turbulence and it is difficult to say which of these two sources would be stronger. A further assumption of the trailing edge model described above is that the flow is steady, which is definitely not the case for a VAWT blade. Application of this type of model to VAWT noise would therefore require careful implementation. It would probably also be necessary to obtain a specific model for the turbulence spectra passing over the trailing edge during dynamic stall.

2.2.2 Laminar Boundary Layer Tonal Noise

The preceding discussion of trailing edge noise assumed that the flow was turbulent as it passed over the trailing edge of the aerofoil. If the flow on the pressure surface remains laminar at the trailing edge it has been shown that a tonal noise is radiated [Paterson et al., 1973]. Tam [1974] suggested that the tonal noise was generated by a feedback mechanism whereby the frequency of the Tollmein-
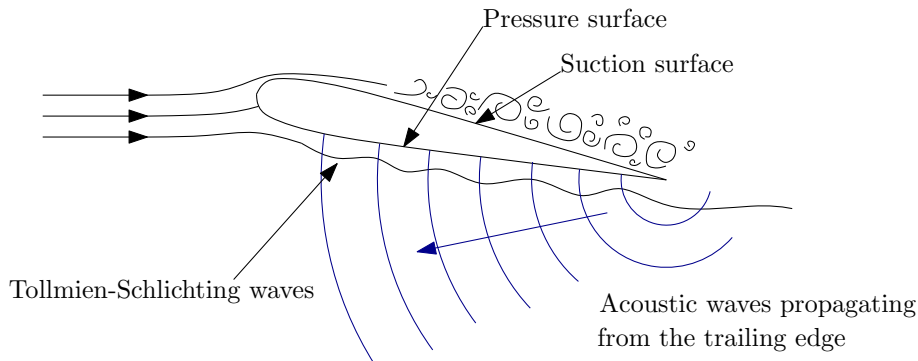
Figure 2.1: Schematic of the mechanism by which laminar boundary layer tonal noise is generated (adapted from Arbey and Bataille [1983]).

Schlichting waves in the laminar boundary layer is influenced by acoustic waves from the blade wake, which reinforce certain frequency components in the flow (see figure 2.1).

Empirical methods were developed by Paterson et al. [1973] and Tam [1974] to predict the frequencies of the tonal components radiated by this mechanism. The frequency of the strongest peak can be estimated from equation 2.9 and the separation between the tonal peaks is given by equation 2.10. Arbey and Bataille [1983] suggested that the exponent in equation 2.10 should be changed to 0.85 since they found this gave better correlation with the experimental data. Their explanation for this change was that the source of the acoustic waves in the feedback mechanism was in fact the trailing edge of the blade rather than a point in the blade wake, as had been previously assumed.

$$f_{n,max} = \frac{KU_\infty^{1.5}}{\sqrt{c\upsilon}} \tag{2.9}$$

$$f_{sep} = AnU_\infty^{0.8} \tag{2.10}$$

More recently, simulations have used the feedback mechanism proposed by Arbey and Bataille [1983] to perform linear stability analysis of low Reynolds number flow over aerofoils [Chong et al., 2013; Kingan and Pearse, 2009]. These simulations have confirmed the relationship $f_{n,max} \propto U_\infty^{1.5}$ and have suggested that the exponent in equation 2.10 should in fact be 0.80 as initially proposed. These simulations have also indicated that this tonal sound is normally solely dependent on the pressure surface flow and is not influenced by the suction surface flow.

The study of McCroskey [1971] showed that boundary layer transition on the pressure surface of an aerofoil at between 4° - 6° angle of attack occurs at a chord based Reynolds number of $Re_c = 1.2 \times 10^6$ and does not occur until $Re_c = 1.7 \times 10^6$

when the angle of attack is between 6° - 8°. Paterson et al. [1973] confirmed that maintaining the laminar boundary layer did mean that tonal noise was radiated at higher Reynolds numbers when the angle of attack was increased. The chord based Reynolds number on the full scale QR5 rotor is $Re_c = 4.1 \times 10^5$ even at the relatively high wind speed of 10m/s. If the inflow is sufficiently smooth it is therefore likely that the flow over the pressure surface of the blades will remain laminar for at least part of the blades' rotation.

2.2.3 Aerofoil Self Noise

Aerofoil self-noise is the noise generated by the interaction between an aerofoil and the flow disturbances produced in its own boundary layer and near wake. Brooks, Pope, and Marcolini [1989] wrote the definitive work on empirical self-noise modelling where they grouped these interactions into five categories (see Figure 2.2) and developed correlations for predicting the sound radiated by each source. The five source terms are:

1. Turbulent boundary layer trailing edge noise (TBL-TE).

2. Separation/stall noise.

3. Laminar boundary layer vortex shedding noise (LBL-VS)[1].

4. Trailing edge bluntness vortex shedding noise (TEB-VS).

5. Tip vortex formation noise (TV).

Extensive measurements of the noise generated by a NACA0012 aerofoil were made in a low-turbulence, acoustically treated, free jet wind tunnel. Measurements were made at a range of Mach numbers and angles of attack. One of the important parameters for determining the noise is the boundary layer thickness, and this was measured using a hot-wire probe 0.64mm from the trailing edge of the aerofoil.

From the results of these measurements a spectral scaling law was derived for each of the five noise sources. The scaling process requires a number of inputs but the most significant are the free stream Mach number, boundary layer displacement thickness and angle of attack along with the aerofoil's geometric parameters. Provided these input parameters are accurately specified the correlations can be used to make predictions of the noise generated by moving aerofoils[2].

---

[1]This is the same as the source mechanism described earlier as laminar boundary layer tonal noise.

[2]Predictive models based on the correlations defined by Brooks, Pope, and Marcolini [1989] will subsequently be referred to as 'BPM' models
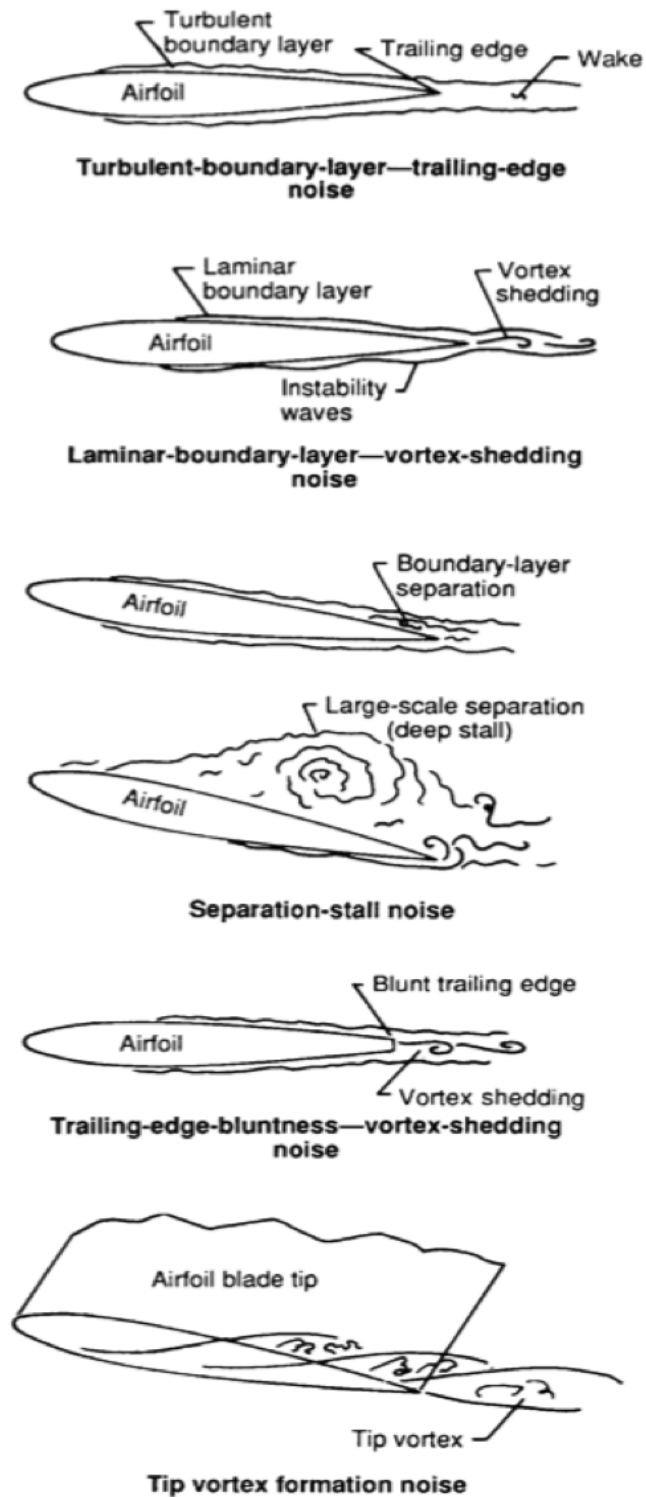
Figure 2.2: Schematics of the five self-noise sources identified by Brooks et al. [1989]

The relative magnitude of these sources is dependent on the exact flow conditions over the aerofoil. In many practical applications, where the boundary layer is turbulent, the LBL-VS noise can be ignored since it is much quieter than the TBL-TE noise. Fink and Bailey [1980] also noted that during stall the noise level can be up to 10dB greater than the noise due to TBL-TE noise at low angles of attack. At moderate angles of attack the noise was still found to be due to the passage of turbulent, separated flow over the trailing edge, while at higher angles of attack the noise was radiated from the chord as a whole [Paterson et al., 1973]

A number of studies have used this model to make predictions of HAWT noise (e.g. Boorsma and Schepers [2011]; Fuglsang and Madsen [1996]; Moriarty and Migliore [2003]), with some success. The generally accepted procedure is to divide the blades into a number of sections along the span and then calculate the noise produced by each element independently. Acquiring the necessary input data for each blade element is achieved by first calculating the large scale flow parameters such as the relative flow speed and angle of attack for each blade segment. A more detailed simulation is then performed to compute the boundary layer parameters for each segment before applying the self-noise scaling laws. In the case of the prediction tool SILANT, described by Boorsma and Schepers [2011], the boundary layer parameters are calculated for a wide range of cases and then inserted into a database in order to reduce the computation time.

One major limitation of this method is that all of the correlations assume that the flow is steady. While this may be approximately true for a HAWT, it is definitely not the case for a VAWT. A further limitation is that all of the data are for a NACA0012 aerofoil. In all of the studies mentioned above it is assumed that the impact of a different aerofoil shape is not significant. It is taken to be sufficient to compute the flow field for the aerofoil profile in question and then simply insert those values into the existing scaling laws.

2.2.4 Inflow Turbulence

The loads on an aerofoil are strongly dependent on the flow conditions. If the oncoming flow is turbulent this will generate fluctuating loads on the blades, which will result in noise being radiated (see Amiet [1975]). As with the aerofoil self-noise, the radiated sound is highly dependent on the exact nature of the turbulent inflow. Unfortunately it is very challenging to accurately characterise the turbulence in the wind, since it is governed by a wide range of parameters such as the surface roughness and the atmospheric temperature gradient. Detailed descriptions of some of the relationships that govern the levels of large scale atmospheric turbulence are presented in the thesis by McIntosh [2009]. There is very little published information about the small scales of atmospheric turbulence and this is for two reasons. Firstly, the vast majority of the energy in the wind

is contained in the larger structures, commonly known as gusts, so from the perspective of power generation the small scales are irrelevant. Secondly, the local surface roughness will affect the turbulence spectra [McIntosh, 2009, section 2.2.4], meaning the small scales are likely to be strongly site specific.

A scaling relationship for turbulent inflow noise was derived by Amiet [1975] and subsequently adapted by Glegg et al. [1986] and Lowson [1994] for use in wind turbine noise simulations. Fuglsang and Madsen [1996], Glegg et al. [1986] and Lowson [1994] all note that the predicted noise due to inflow turbulence is very sensitive to the turbulence length scale used in the scaling relationship. Fuglsang and Madsen [1996] quantitatively investigated this relationship and showed that, for their model, if the turbulence length scale was increased from 25m to 200m the sound pressure level (SPL) rose by around 10dB. This variation was particularly significant because it changed the dominant noise source from being aerofoil self-noise to inflow turbulence noise. Glegg et al. [1986] found however, that the best fit between the measured data and the turbulent inflow model occurred with a turbulence length scale equal to the blade chord. This is much smaller than the scales that are typically modelled or measured in the atmospheric boundary layer.

2.2.5 Directivity and Retarded Time Effects

The analytical source models, such as the moving point force model of Lowson [1965], directly encompass directivity and the retarded time effects for moving sources. Completely empirical source models do not include either of these features so they have to be accounted for separately. The semi-empirical trailing-edge noise prediction method of Amiet [1975] includes directivity effects, but care must be taken to correctly account for the retarded time when computing the average spectrum radiated from a moving source.

In the fully empirical method of Brooks et al. [1989] the source directivity is modelled using the equation derived by Schlinker and Amiet [1981], which is split into the separate high- and low-frequency terms given in equations 2.11 and 2.12, with the angles as defined in figure 2.3. In these equations, a high-frequency is defined as being greater than that given by the flow speed divided by the aerofoil chord length. In addition, Brooks et al. [1989] found that in stalled flow conditions the low-frequency directivity expression was better over all frequencies.

$$\overline{D_h}(\Theta_e, \Phi_e) \approx \frac{2\sin^2(\Theta_e/2)\sin^2\Phi_e}{(1 + M\cos\Theta_e)\left[1 + (M - M_c)\cos\Theta_e\right]^2} \quad \text{High Frequency} \quad (2.11)$$

$$\overline{D_l}(\Theta_e, \Phi_e) \approx \frac{\sin^2(\Theta_e)\sin^2\Phi_e}{(1 + M\cos\Theta_e)^4} \quad \text{Low Frequency} \quad (2.12)$$
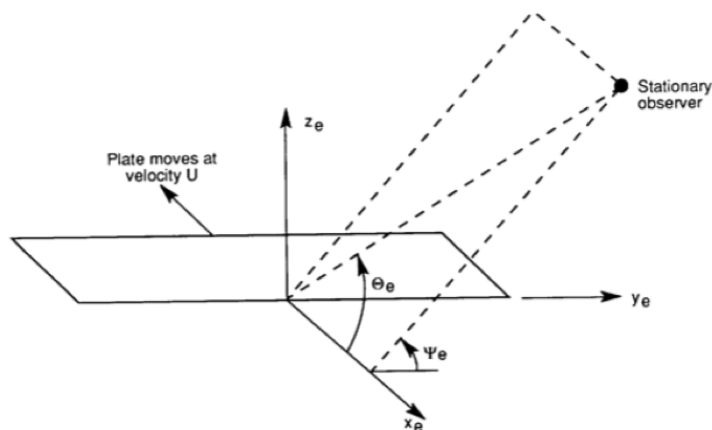
Figure 2.3: Schematic illustrating the angles required for calculating the trailing edge noise directivity

The empirical and semi-empirical model sound fields are all derived relative to the source at its emission position, $\mathbf{x_e}$, and the blade is assumed to be in uniform, rectilinear motion. In order to find the mean spectrum radiated to an observer from a rotating source it is necessary to integrate over a complete revolution of the blades. This integration needs to account for the effects of retarded time, the curvature of the blade's trajectory, and Doppler shift and amplification. This is not a straightforward process, but a clear, detailed description of the necessary calculations is given by Sinayoko et al. [2013]. The method they described was applied to the VAWT noise prediction model developed in this study, as detailed in section 6.3.1.

2.3 Horizontal Axis Wind Turbines

The ways in which HAWTs and VAWTs produce torque are substantially different, and this has a bearing on the mechanisms of noise generation. It is nevertheless worthwhile to consider the methods which have been used to investigate HAWT noise, since they can inform the methods used for the current study.

2.3.1 Computational Studies

Despite recent increases in computational power, direct numerical simulation of the flow through a full HAWT rotor is still a distant prospect. As such, simplified models are used to estimate the noise radiated from the blades of a HAWT. Earlier investigations, such as that conducted by Glegg et al. [1986], did not use

any CFD simulations, and relied entirely on theoretical formulations and semi-empirical methods such as that of Amiet [1975]. This type of approach is capable of predicting spectra that are in line with measured data, but it is heavily reliant on estimates of input parameters like the turbulence intensity and length scale of the incoming wind. Glegg et al. [1986] found that the turbulence length scale predicted by the ESDU model of anisotropic atmospheric turbulence [ESDU, 1974] resulted in the noise radiation being underpredicted by up to 10dB. When the turbulence length scale was set to the blade chord length the predicted spectra matched the measured spectra to a much better degree. The turbulence inflow noise was then found to be the dominant source for the two rotors examined.

More recently there have been a number of attempts to model the noise radiation from HAWTs using the spectral self-noise predictions of Brooks et al. [1989] (see Boorsma and Schepers [2011]; Fuglsang and Madsen [1996]; Lowson [1994]). These methods typically use a simplified 2D CFD simulation to calculate the flow properties over the blades at a series of spanwise locations. The aerodynamic data from these calculations is then used as the input for the empirical model. As with the method of Glegg et al. [1986], this approach is capable of generating spectra that are in agreement with measured data. It is still heavily dependent, however, on certain input parameters, particularly the properties of the inflow turbulence.

The approaches using self-noise predictions do not come to uniform conclusions regarding the dominant sources of noise. The simulations of both Lowson [1994] and Boorsma and Schepers [2011] suggest that turbulence inflow noise is only greater than trailing edge noise below 100Hz, while Fuglsang and Madsen [1996] found it to be dominant up to around 500Hz. This may be because the first two studies were comparing their predictions against turbines with rotor diameters of greater than 90m and the third study only compared with 30m rotors. Larger rotors necessarily have greater hub heights, meaning that they sit further out of the atmospheric boundary layer where the turbulence intensity is less. This fact could explain the observed discrepancy in the conclusions of these studies.

Growing computational power has made it possible to simulate the flow over the blades of an HAWT in ever-increasing detail. This has led to a number of approaches that use advanced CFD methods (e.g. Reynolds Averaged Navier Stokes) to compute the flow over the blades and then use the Ffowcs Williams-Hawkings equation to model the sound propagation (see Morris et al. [2004]; Ramachandran and Raman [2011]; Tadamasa and Zangeneh [2011]; Xue et al. [2011]). These methods are less reliant on estimates of the turbulence statistics and are instead, dependent on the turbulence modelling approach used in the CFD. The study of Kamruzzaman et al. [2011] examined the spectra predicted by this type of approach and, while their method approximately predicted the correct spectral shape, their implementation of the BPM model still yielded better

results.

These studies highlight one of the major problems with any aeroacoustic prediction program: the quality of the input data. The propagation of sound can be exactly modelled using analytical formulations such as the Ffowcs Williams-Hawkings equation. The aerodynamic inputs required for these propagation models are however, difficult to determine with any real certainty. This does not render the prediction codes useless, but may slightly alter their application. If a prediction model can be made to generate a spectrum that matches well with data measured for a given wind turbine, it may be possible to investigate the impact of certain incremental rotor design changes on the radiated sound. This is the objective of the simple noise prediction models described in chapter 6 of this report.

2.3.2 Experimental Investigations

Accurately determining the noise from an operating, full-scale wind turbine is not a simple task. The variations in wind speed and direction require a large number of measurements to be made which are then grouped according to the wind condition before being averaged. There are also problems regarding how to account for the background noise. The standard methodologies for measuring the noise from wind turbines, such as the BS-EN-61400 or IEC-61400-11, do attempt to account for these effects, but there is a degree to which these standards need further development (see, for example Sondergaard [2011]). In terms of identifying the mechanisms of noise generation, the most interesting experimental studies are those carried out by Oerlemans et al. [2007], which used phased array measurements to not only quantify the noise radiation from wind turbines, but also to locate the dominant noise sources.

Oerlemans et al. [2007] found that the dominant source was in the outer portion of the blade and indicated that there is significantly more noise radiated to the observer during the downward motion of the blades (see figure 2.4). This was demonstrated to be the result of a combination of convective amplification (6dB) and the directivity (9dB) of the source. By comparison with the expression for directivity of trailing edge noise derived by Brooks and Burley [2001], it was found that the directivity amplification was consistent with the sound being radiated from the trailing edge.

Work by Sijtsma et al. [2001] used a phased array to measure the noise radiated from a model HAWT and a model helicopter in the open-jet wind tunnel at DNW-LLF. The beamforming algorithm was extended to detect rotating sources. This involved deriving a method to account for the Doppler amplification and modulation resulting from the fact that the source was moving. Since the array was outside the wind tunnel's jet, a correction was also required to deal with
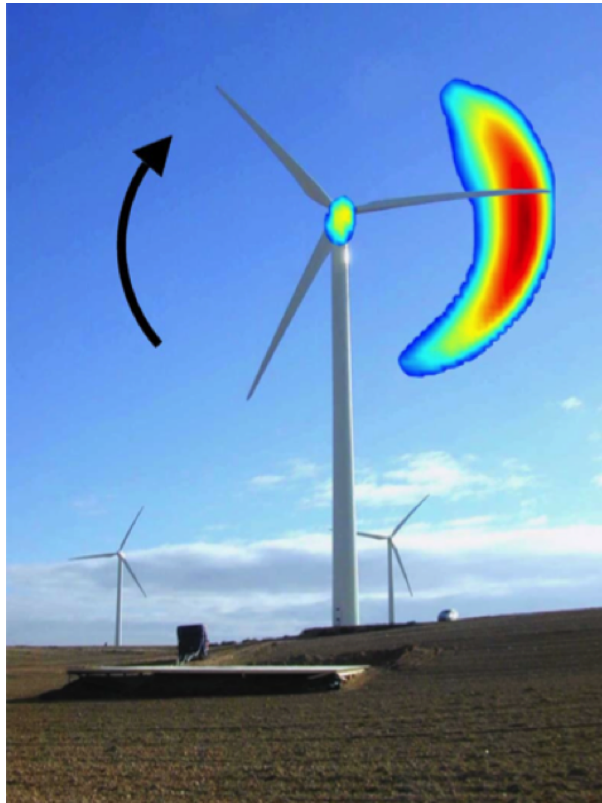
Figure 2.4: Result of the acoustic array measurements carried out by Oerlemans et al. [2007] on a G58 wind turbine. The horizontal platform in the foreground is the acoustic array used. The coloured regions of the plots indicate the source strength estimated by the acoustic array in decibels, defined as $10 \log_{10}(P_{source}^2/P_{ref}^2)$.
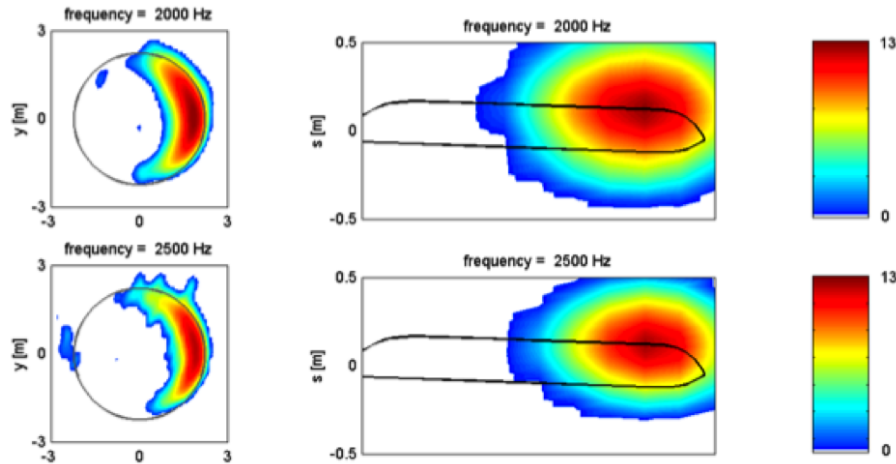
Figure 2.5: Example of the source maps from Sijtsma et al. [2001]. The left hand plots are the conventional time-averaged maps while those on the right were generated using the ROSI algorithm

the refraction of the sound at the shear layer. The resulting algorithm, 'ROSI' (ROtating Source Identifier), was used to examine the individual noise sources on each blade while they were moving. An example of the output is presented in figure 2.5, which shows that the noise was generated at the trailing edge of the blades near the tips. This result is consistent with the data presented by Oerlemans et al. [2007].

2.3.3 Trailing Edge Noise Mitigation

There is a growing consensus that trailing edge noise is the dominant noise source on HAWTs and, as such, there has been significant interest in methods for mitigating trailing edge noise radiation. One method that has been widely tested is to add a serrated trailing edge to the blades. Oelermans et al. [2009] used an acoustic array with the ROSI algorithm to measure the sound field from a HAWT rotor with different blades, including one with a serrated trailing edge. It was found that the serrated trailing edge reduced the overall sound radiation by 3.2dB on average. The modified blades did however, increase the high frequency noise radiated from the blade tips on the upward portion of the rotation.

Chong et al. [2013] performed wind tunnel measurements of blades with serrated trailing edges that were not simply flat plates inserted into the trailing edge, but were tapered in line with the blade profile. They found that these blades did not generate the high frequency noise seen for the serrated, flat plate trailing edges, but instead generated low frequency noise from the blunt sections of the

trailing edge. Research to find the optimal design of serrated trailing edges for a range of applications, including HAWTs, is ongoing.

2.4 Helicopter Noise

In many ways, the aerodynamics of VAWT rotors has more in common with helicopters than with HAWTs. During the early work on helicopter noise it was found that, when helicopter rotors operate in sideslip mode, they experience unsteady blade loads generated by interaction with the wake from previous blade passages. These blade loads occur at frequencies up to many harmonics of the rotor angular velocity [Lowson and Ollerhead, 1969]. This is very different from the situation for propellers or HAWTs, which have an approximately uniform inflow and therefore relatively constant blade loads.

Unsteady loading on the blades is a potentially strong noise source and can be simply modelled using the unsteady point force model of Lowson [1965]. This model highlights the fact that the noise is proportional to the rate of change of force, meaning that, if the fluctuation is rapid enough, even a small amplitude fluctuation in the blade load can radiate a significant amount of sound. This has led to a great deal of work on impulsive blade loading in helicopter rotors.

Studies of helicopter noise have found that, when a helicopter rotor generates impulsive noise, it is the dominant source [Schmitz and Yu, 1986]. Two mechanisms have been identified that produce impulsive noise, and they are known as high-speed impulsive noise and blade-vortex interaction (BVI). High-speed impulsive noise is due to compressibility effects at the blade tips, associated with high blade Mach numbers. This effect is not going to be significant for VAWTs, where the blade Mach number is always sufficiently low that the flow can be treated as incompressible. The aerodynamics of VAWTs however, mean that BVI is very likely to occur, so this noise source mechanism is discussed in detail below.

2.4.1 Blade-Vortex Interaction Noise

As a VAWT rotates, the lift, and therefore the circulation, on the blades fluctuates, meaning that they will shed vorticity. At lower tip speed ratios, the blades may also experience dynamic stall, during which strong vortices are shed (see section 3.1.2). The downstream blades will interact with the vortical wake from the upstream blades and this may generate impulsive blade loads by blade-vortex interaction.

As the blade passes a vortex generated by a previous blade passage it experiences a change in angle of attack due to the vertical velocity component induced by the vortex. This in turn causes a change in lift on the blade. If one then con-
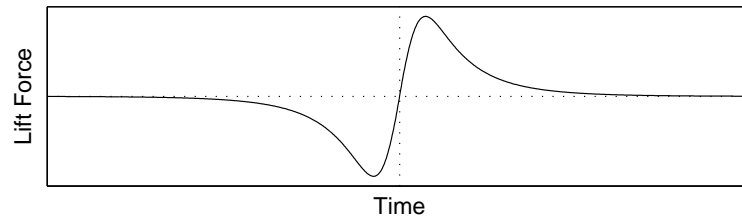
(a) Blade loads resulting from a BVI
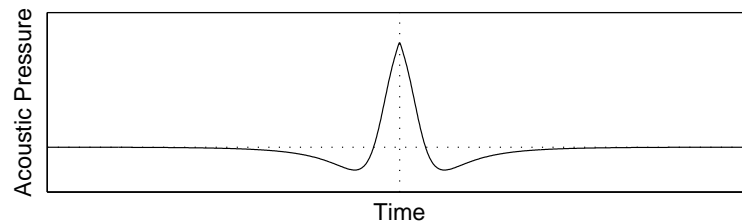
(b) Acoustic pressure generated by a BVI

Figure 2.6: (a) An approximation of the blade loads during a blade vortex interaction and (b) the resulting acoustic pressure.

siders the noise radiated by a fluctuating force, as given by Lowson in equation 2.5, the expected acoustic pressure fluctuation can be derived. Figure 2.6 shows the results of a basic calculation of the fluctuations in lift and acoustic pressure as the result of a 2D BVI. Schmitz and Yu [1986] present some equivalent plots and identify the positive pressure spike as the signature of BVI in helicopter rotor noise measurements. Whether the spike is positive or negative will depend on the direction in which the vortex is rotating.

The strength of the sound radiated by BVI from helicopter rotors was found to be dependent on four factors [Schmitz and Yu, 1986]:

1. Local strength of the tip vortex.

2. Core size of the tip vortex.

3. Local interaction angle of the blade and the vortex line.

4. Vertical separation between the vortex and the blade.

The interaction angle of the blade and the vortex line presents a particularly interesting problem, relating to the speed at which the interaction location moves along the span of the blade. When the interaction angle is small it is possible, even for blades with low velocities, that the interaction location will travel along
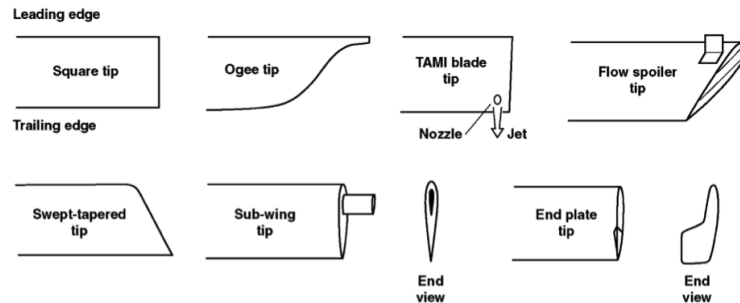
Figure 2.7: Blade tip geometries investigated by Brooks [1993]

the span at close to the speed of sound. This has significant implications for both the magnitude and directivity of the radiated sound [Lowson, 1996].

The speed of the interaction location is commonly referred to as the phase or trace Mach number. It can be straightforwardly calculated by considering the relative velocity of the blade and vortex, and the angle between them. If the interaction location moves at greater than the speed of sound then a Mach cone is formed and the intensity of the sound in the direction perpendicular to the resultant weak shock is greatly increased. It was reported by Lowson and Ollerhead [1969] that when the phase speed becomes supersonic the noise level due to the intercation of a blade with a sinusoidal wave could increase by up to 90dB in certain directions. For the case of small VAWTs however, where the blade speed is usually less than 25m/s, the blade and vortex would need to be very nearly parallel for the phase Mach number to reach 1. While it is possible that this could occur it is unlikely to be a common problem.

2.4.2 BVI Noise Mitigation

In order to reduce the noise generated by BVI, one of the four variables listed above needs to be altered. The most common method used on helicopters is to change the shape of the blade tip so that the tip vortex is either weaker, more diffuse or both. The key is to achieve this objective without reducing the overall performance of the blade.

Experimental measurements using the tip geometries shown in figure 2.7 found that the tip vortices were more diffuse, but there was no significant reduction in BVI noise [Brooks, 1993]. More complex tip shapes including small vanes (see figure 2.8) have been investigated, and were found to reduce BVI noise by up to 5.6dB, while having no adverse effects on the blade performance [Brocklehurst and Pike, 1989]. All of these measurements were carried out for helicopter rotors with much higher blade tip speeds than VAWTs. The relative impact of these tip shapes at lower speeds will probably be different and therefore would require
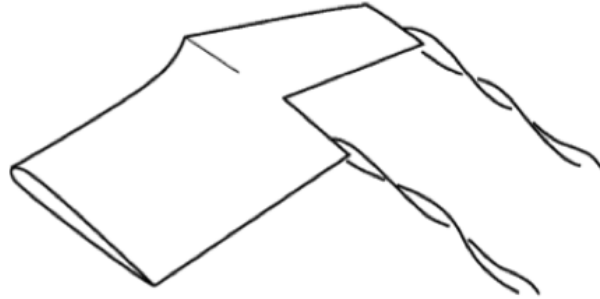
Figure 2.8: Vane-tip geometry investigated by Brocklehurst and Pike [1989]

further investigation. It is also uncertain whether the tip vortices from the VAWT blades would dominate the wake to the same extent as they do on a helicopter rotor.

In their survey of helicopter structural loads Shockey, Williamson, and Cox [1976] measured the blade loading during BVI and found that it is predominantly a leading edge phenomenon. One possible method for reducing the impact of impulsive loading at the leading edge is to use a passive porous system. This involves the blade having a porous surface with a plenum underneath. This allows the local high pressure at the leading edge to be redistributed to other areas of the blade by small levels of mass flow into and out of the plenum. Ultimately this has the effect of increasing the time period over which the change in pressure on the blade surface takes place. The magnitude of the peak change in lift is also reduced [Tinetti, 2001]. Since the noise is proportional to the rate of change of force, this should result in a less intense pressure fluctuation and hence a quieter sound. Tinetti [2001] showed that, for the unsteady blade loading experienced on the stator vanes in turbo-machines, porous leading edges could reduce the peak noise level by up to 2.5dB.

A further way in which helicopter blade loads can be altered to reduce BVI is by active blade control, which involves using actuators that adjust the blade pitch at certain azimuthal locations. This method works by causing the blade to be physically deflected such that there is a greater vertical separation between the tip vortex and the blade. This technique has been employed in two forms known as higher harmonic control (HHC) and individual blade control (IBC). These methods were originally developed to reduce physical vibrations in order to improve comfort for helicopter passengers, but, by lowering the impulsive aerodynamic loads, the radiated noise was also reduced [Yu et al., 1997].

HHC was found to decrease overall noise levels but potentially increase the low frequency noise. IBC was shown to yield significant reductions in both vibration and noise. In the optimal configuration, IBC reduced vibrations at the blade

passage frequency by 90% and reduced the noise levels by 12dB [Swanson et al., 1995].

The noise mitigation methods presented here each have their own pros and cons. Active blade control potentially yields greater noise reduction but the increased complexity of design and operation would probably make it impractical and costly to implement. Also, given the long operating lifetime of wind turbines, the robustness and reliability of such a system could be problematic. For porous leading edges the most likely problem would be keeping the pores clear of dirt. The potential reduction in noise is also much smaller than the other two methods. Modifying the blade tip shape is a relatively simple design change, which would not present any of the reliability and complexity problems of the other two methods. The relative significance of the tip vortices on the aeroacoustics of a VAWT is currently uncertain. If it is found that interaction of the downstream blades with the tip vortices shed upstream is generating noise, then altering the blade tip geometries could be an efficient solution.

2.4.3 Harmonic Noise Modelling

If a helicopter is experiencing BVI in steady flight then the interactions between the blades and the vortices in the wake would be expected to occur at a fixed blade azimuth. For the purposes of modelling this means that a simplifying assumption can be made, that the blade loads are perfectly periodic. This allows the sound field to be straightforwardly modelled in the frequency domain by deriving a relationship between the blade loading harmonics and the radiated sound harmonics.

This approach has been developed using two slightly different methods by Lowson and Ollerhead [1969] and Wright [1969], although they both come to similar conclusions. Using these theoretical models, and by comparison with experimental measurements, both methods identified some key features of the noise generated by rotating harmonic sources.

1. Lowson [1965] observed that there is significant scattering of the blade loading harmonics to a wide spectrum of sound harmonics. For instance, to correctly predict the sound level at the 10th harmonic of the rotor angular velocity, blade loading data up to the 60th harmonic were required. Accurate prediction of the sound field therefore requires very high fidelity blade loading information.

2. Wright [1969] showed that, if the steady loading component of the blade loading was low, or if there were a large number of blades, then the fluctuating loading component would dominate the sound field. In a later paper

Wright [1971] found that fluctuating forces weaker than one-thousandth of the steady loading component can dominate the radiation due to the steady component.

3. Wright [1971] found that, while the steady loading noise could be reduced by increasing the number of blades or reducing the blade tip velocity, the noise due to the fluctuating blade loads was unaffected by these parameters.

4. Wright [1971] also found that the impulsive loads were most significant in terms of acoustic radiation. It was suggested that to reduce the noise these impulsive loads had to be completely avoided by changing the design or operating condition of the rotor.

2.5   Summary

There are various potential methods for predicting the noise radiated from a moving aerofoil. Unsteady blade loading is a potentially strong source of noise and an efficient, simplified model of the source can be implemented using the results derived by Lowson [1965]. One of the problems with many aeroacoustic models is the dependence on the aerodynamic inputs, which are often difficult to measure or model with sufficiently high resolution to make accurate acoustic predictions. Even without accurate inputs however, such models can be used to investigate the importance of various design parameters on the levels of noise radiated.

One way to partly avoid the difficulties of trying to determine the aerodynamic loads is to use an empirical model such as that developed by Brooks et al. [1989]. This method is potentially useful, but was developed to model the noise from steady flow over an aerofoil. Since the flow over a VAWT blade is fundamentally unsteady it is not clear whether such a model would be able to accurately predict the sound radiated from a VAWT rotor.

The phased array measurements carried out by Oerlemans et al. [2007] proved very useful in identifying the sources of noise on a large scale HAWT. The dominant source was located at the blade trailing edge and was found to radiate most strongly to the observer when the blade was on its down-stroke. It is hoped that similar phased array measurements of VAWT noise will deliver equally informative results.

A variety of mitigation techniques for reducing aeroacoustic noise, such as serrated trailing edges, specialised blade tip geometries and active blade control have been developed. Depending on the nature of the noise sources identified on the VAWT, a range of options are therefore available for attempting to reduce the radiated noise. Further potential options for mitigating noise radiation from

VAWTs are highlighted in the next chapter, which focusses on the aerodynamic design and performance of VAWT rotors.

Chapter 3

Vertical Axis Wind Turbine Performance

The aeroacoustic sound radiated from a wind turbine rotor is driven by the rotor aerodynamics. It is therefore important to have a thorough understanding of the aerodynamics before approaching the noise problem. In addition, the design of wind turbines is often driven by aerodynamic performance, and it is necessary to appreciate these design constraints when investigating the problems of noise generation. This chapter first describes some of the key aerodynamic features of wind turbine performance and examines some of the available data on VAWT performance. The phenomenon of dynamic stall is discussed in some detail as it has a significant impact on both the large and small scale behaviour of VAWT rotors.

The second section goes on to look in detail at the key parameters that must be considered when designing a VAWT rotor. The performance impact of the rotor solidity, rotor aspect ratio, blade profile, preset pitch, blade sweep and blade curvature are all discussed. This discussion demonstrates that the designer of a VAWT rotor has significant scope to alter the performance of the rotor and is able, to a reasonable extent, to choose the position of the peak operating point.

The third section discusses the computational methods developed to model the performance of VAWTs. The advantages and disadvantages of each of the methods are assessed and some of the key results are presented. Finally, the impacts of the aerodynamic behaviour on noise generation are summarised and the potentially significant noise sources are highlighted.
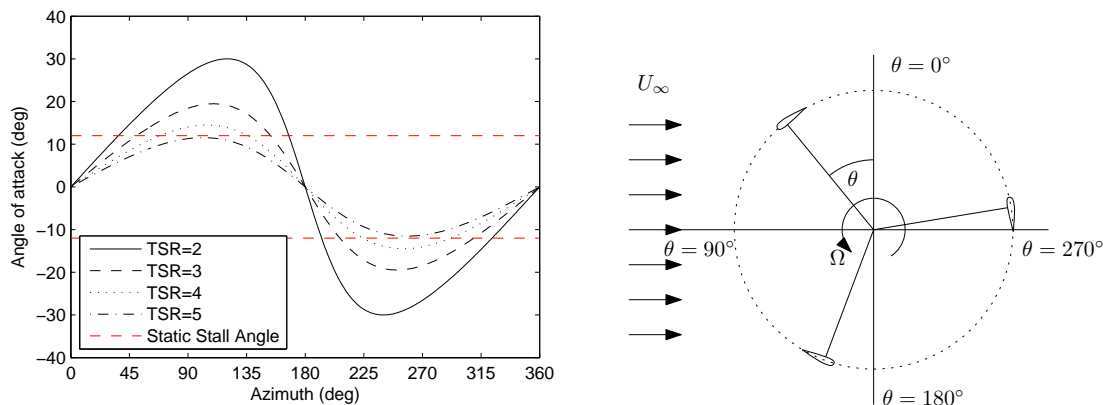
Figure 3.1: Variation of angle of attack with azimuth at different TSR

3.1 Aerodynamic Behaviour

3.1.1 Basic Features

The aerodynamics of a lift-type VAWT are fundamentally unsteady. As the blade rotates around the hub the angle between the blade velocity and the wind velocity varies significantly. This creates a variation in angle of attack and hence a variation in the aerodynamic forces exerted on the blades. The magnitude of this variation is governed by the tip speed ratio (TSR) which is defined as the ratio of the blade speed to the wind speed.

An approximation of the variation in blade angle of attack can be calculated using simple geometry by assuming that the free stream flow is uniform in both magnitude and direction over the whole rotor. This 'geometric' variation in angle of attack is shown in figure 3.1 for a range of TSR. It is important to note that the geometric angle of attack varies from the true angle of attack due to the deflection of the incoming flow by the rotor (see section 3.1.3 on the induction factor).

From figure 3.1 it is clear that at low TSR the blades pass the static stall angle as they approach the most upstream point of the rotation. Since the angle of attack is constantly changing, the blades will experience dynamic stall at low TSR. As the TSR increases, the extent of the stall in the upstream half of the rotor decreases, which increases the amount of torque that the blades generate since the lift to drag ratio remains higher. The higher blade speed however, increases the level of parasitic drag on the rotor which simultaneously reduces the torque generated by the rotor. As such the design of a VAWT rotor is a trade off between minimising both stall and drag in order to achieve maximum

35
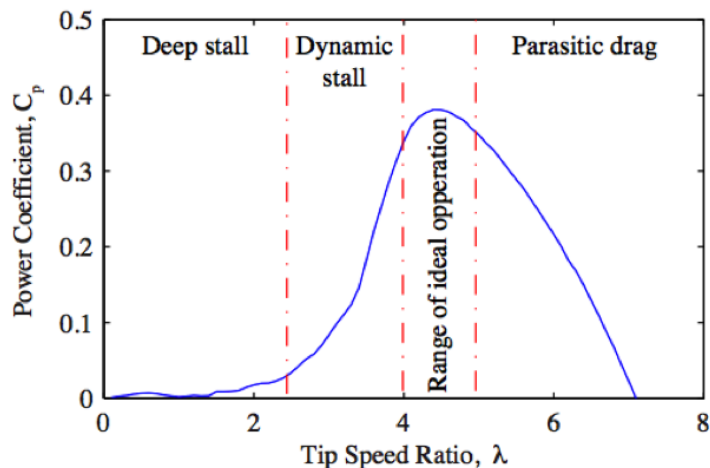
Figure 3.2: Typical variation in power coefficient as a function of TSR for a VAWT highlighting the different performance regimes [McIntosh, 2009]

performance (see figure 3.2).

The second key feature of VAWT operation is the fact that the blades in the upstream half of the rotation shed a wake that passes through the rotor and interacts with the blades in the downstream half of the rotation. This effect is exaggerated by the influence of the tip vortices shed by the upstream blades since their direction of rotation tends to cause the wake at the top and bottom of the rotor to be deflected towards the mid-span of the downstream blades, as shown by the simulations of both Scheurich [2011] and Ferreira [2009]. This potentially introduces further unsteady blade loading that could affect the noise radiated by a VAWT rotor.

3.1.2   Dynamic Stall

During operation at lower TSR the blade angles of attack will exceed the static stall angle. Since the blade angle of attack is constantly changing, the blades experience dynamic stall, which results in a significantly different lift and drag behaviour relative to a static aerofoil: Leishman [2006] found that the dynamic loads can exceed the static values by up to 100%. The process of dynamic stall has been found to be dependent on a large number of factors including Mach number, Reynolds number, pitching rate and aerofoil profile [Carr et al., 1977], but a general description of the stages of dynamic stall has been outlined by Leishman [2006] as shown in figure 3.3. The stages of dynamic stall were first described by Carr et al. [1977] based on data from hot-wire measurements. The sequence below summarises the key points such that they correspond to the five

images presented in figure 3.3.

1. The aerofoil initially passes the static stall angle without any detectable change in the flow over the aerofoil and the boundary layer remains thin with no evidence of flow reversal. As the aerofoil incidence increases further, the flow in the boundary layer starts to reverse at the surface.

2. Larger eddies start to form and full flow reversal moves from the trailing edge to the leading edge. When the flow reversal reaches the leading edge a strong leading edge vortex is formed.

3. As the angle of attack continues to increase the separated leading edge vortex grows and advects along the blade chord resulting in a loss of lift at the leading edge and a shift of the centre of pressure to the aft of the blade. This is the cause of the abrupt change in the pitching moment coefficient which is typically described as 'moment stall'. Carr et al. [1977] observed that the peak in the pitching moment curve occurred just before the core of the leading edge vortex passes over the trailing edge of the blade. It is this large, intense vortex that maintains flow curvature over the aerofoil and prevents lift stall. As the vortex moves towards the trailing edge however, the flow curvature starts to reduce and the lift coefficient starts to drop.

4. Once the leading edge vortex has passed off the trailing edge the aerofoil can no longer produce the flow curvature required for lift generation, and an abrupt drop in the lift coefficient occurs. After this point the flow over the aerofoil is fully separated as seen in full static stall hence the lift and drag coefficients tend towards their static values. Other smaller vortices may continue to form and be shed from the trailing edge resulting in further unsteadiness in the blade loading.

5. As the blade pitches down the flow attaches from the leading edge. The reattachment point moves along the blade chord at a velocity of approximately 25-35% of the free stream velocity. Depending on the pitching rate the process of reattachment may not be complete until the aerofoil is well below the static stall angle, so the static values of lift and drag will not be achieved until a lower angle of attack. Carr et al. [1977] noted that even once the flow is fully reattached the potential flow does not appear to return to unstalled conditions until the blade has passed its minimum angle and is already on the upstroke.

Understanding this dynamic phenomenon is very important for a range of applications, especially helicopter rotor blades, and is still an active area of research.
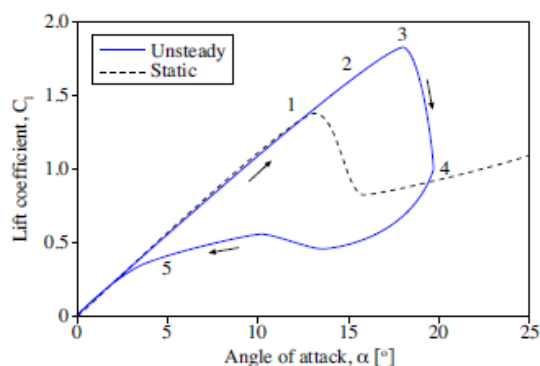
(a) Dynamic lift.
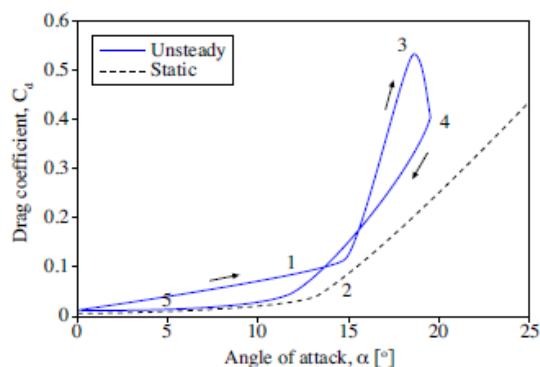
(b) Dynamic drag.
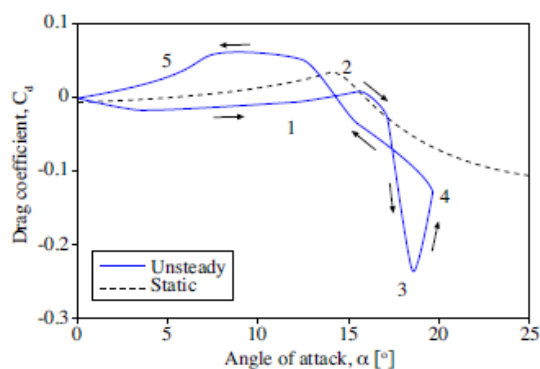
(c) Dynamic pitching moment.
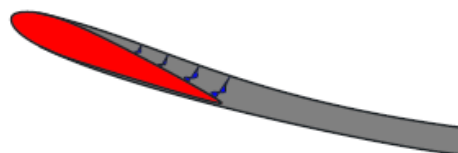
(d) **Stage 1**: Airfoil exceeds static stall angle, flow reversals take place in boundary layer.
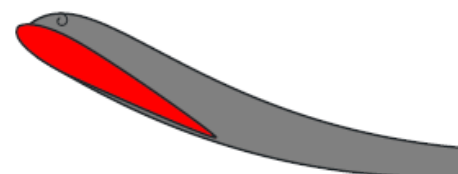
(e) **Stage 2**: Flow separation at the leading-edge, formation of 'dynamic stall vortex'. Moment stall.
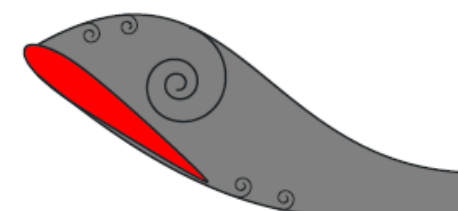
(f) **Stage 2-3**: Vortex convects over chord, inducing extra lift and aft centre of pressure movement.
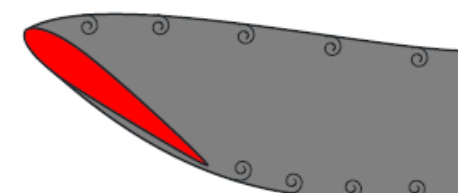
(g) **Stage 3-4**: Lift stall. After vortex reaches trailing edge, flow progresses to a state of full separation.
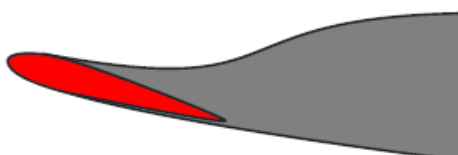
(h) **Stage 5**: When angle of attack becomes low enough, flow reattaches front to back.

Figure 3.3: The stages of dynamic stall as described by Leishman [2006] (figure taken from McIntosh [2009])

Due to limitations in computational capabilities the earlier research focussed on developing a semi-empirical method for predicting the blade loads experienced during dynamic stall. Beddoes and Leishman [1989] developed such a model using the analytical results from thin aerofoil theory combined with empirical inputs from experimental data. This model was originally developed for modelling helicopter rotor blades, but a number of adaptations were made by Berg [1983] for modelling VAWT blade loads and this model has been used in several studies [Masson et al., 1998; McIntosh, 2009; Paraschivoiu and Allet, 1987].

More recent studies have applied modern computational methods to the problem of modelling dynamic stall (Akbari and Price [2003], Ekaterinaris and Platzer [1997], Ferreira et al. [2007]). Of particular interest is the work of Ferreira et al. [2007] who compared various computational models for predicting the aerodynamic loads on a VAWT. The Detached Eddy Simulation (DES) and Large Eddy Simulation (LES) models both predicted that during dynamic stall the blades would experience highly unsteady loading, although there was some uncertainty as to whether this was a physical feature of the flow or a computational convergence problem. These highly unsteady loads do, however, appear to approximately agree with the high frequency load measurements made by Tsang et al. [2008] for a range of dynamic stall conditions, which also showed significant load fluctuations (see figure 3.4). Unsteadiness in blade surface pressures during dynamic stall was also observed by Leishman [1990].
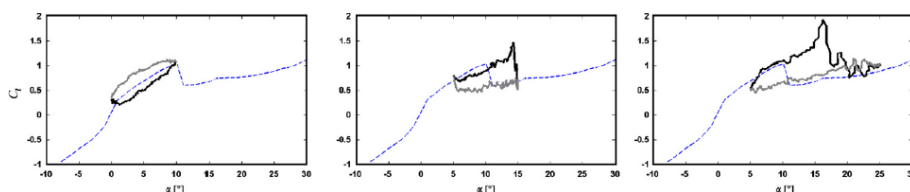
Figure 3.4: Variation in lift coefficient during dynamic stall. From left to right the pitching angles are, $\alpha = 5 + 5sin(\Omega t)$, $\alpha = 10 + 5sin(\Omega t)$ and $\alpha = 15 + 10sin(\Omega t)$. For all cases the reduced frequency of the pitching rate is $k = 0.04$ [Tsang et al., 2008]

These high frequency components of the blade loading were observed by Wang et al. [2010], who used CFD to model dynamic stall cases similar to those measured by Tsang et al. [2008]. Wang noted that the flow reversal on the suction surface produced a highly unstable region of flow near the blade, which resulted in the generation of a number of small vortices on the blade surface. Wang suggested that the unsteadiness observed in the blade loads was the result of these small vortices advecting over the blade. These rapid load fluctuations are potentially significant from the perspective of far-field noise generation since the noise

radiated by a fluctuating point force is proportional to the rate of change of force (see equation 2.5).

There have been several experimental studies of dynamic stall specific to VAWTs (see Fujisawa and Shibuya [2001], Ferreira [2009] and Edwards et al. [2012]). Fujisawa and Shibuya [2001] used a small model VAWT in a water tank to examine streamlines and perform Particle Image Velocimetry (PIV) to analyse the flow during dynamic stall around a VAWT blade at TSR=2. The streamline images in figure 3.5 clearly show the shedding of intense vortices during dynamic stall, and these vortices are seen to advect through the rotor to volume such that they are likely to interact with the blade in the downstream half of the rotor.
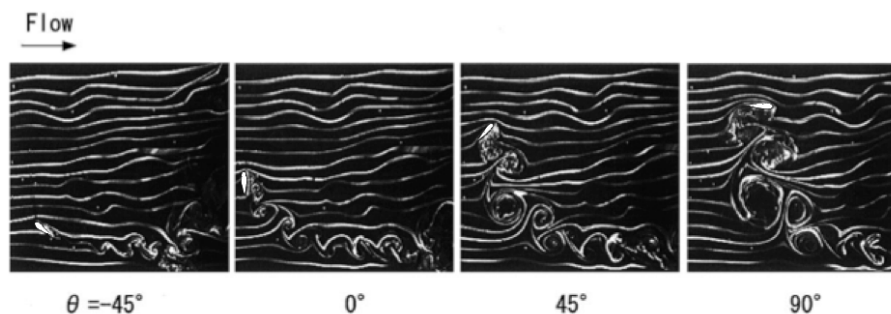
Figure 3.5: Smoke flow visualisation of dynamic stall on a VAWT blade at TSR=2 Fujisawa and Shibuya [2001]. (Note that a different definition of azimuth is used from this study so that 0deg corresponds to the most upstream blade location)

The thesis of Edwards [2012] also used PIV to visualise the flow around VAWT blades at a range of TSR. In order to focus on the large scale features of the flow the PIV plots were generated from phased averages of 100 samples. This showed the same large scale flow features, such as the vortex shedding and reattachment, seen in the PIV experiments of Ferreira [2009]. One interesting result from Edwards' experiments was the identification of the point at which the flow reattached to the blades. For both the TSR=2 and TSR=3 cases the flow was seen to not be fully reattached until after 180° blade azimuth (i.e. not until the blades had passed the fully downwind direction) and it was suggested that for the TSR=2 case the flow was not attached for the majority of the downstream half of the rotation. The detached flow produced a high level of drag, which resulted in negative values of the measured power coefficient at low TSR. These results, indicating a very late reattachment of the flow, agree well with the CFD simulations of Wang et al. [2010] who found that, for a blade oscillating between $0 - 25 \deg$ at a reduced frequency of $k = 0.15$, the flow did not reattach until the angle of attack had dropped to zero.

One feature of dynamic stall that is worth considering for these model scale experiments is the impact of the reduced frequency at which the angle of attack oscillates. The experiments of Tsang et al. [2008] demonstrated that the pitching rate of the blade had a significant impact on the extent of the dynamic stall on a NACA-0012 aerofoil. Their definition of the reduced frequency was $k = \pi f c / U_\infty$ and this dimensionless parameter has been calculated for each of the experimental set-ups described above along with the experimental model used in this study and the full scale QR5 turbine pictured in figure 1.4(a).

Rotor	R (m)	c (m)	U_∞ (m/s)	f(Hz)	$k = \pi f c / U_\infty$
Edwards	0.350	0.040	7.0	9.55	0.057
Ferreira	0.200	0.050	5.0	11.94	0.125
Fujisawa	0.030	0.010	0.05	0.769	0.167
QR5	1.500	0.175	10.0	3.18	0.058
Current Study	0.265	0.055	6.6	11.94	0.104

Table 3.1: Comparison of the reduced frequency of the fluctuation in blade angle of attack for the dynamic stall experiments described along with the values for the QR5 and the wind tunnel model used in this study.

The data in table 3.1 show that the model scale turbines used to investigate the dynamic stall on VAWTs have a reduced frequency of blade oscillations that is roughly similar to the full scale QR5. In particular the model used by Edwards [2012] is very similar to the QR5 by this measure. This means that the dynamic stall behaviour observed should be generally similar to that observed on the full scale rotor.

One other interesting result from the high resolution blade load measurements made by Tsang et al. [2008] was the behaviour of the blade loads when the angle of attack does not exceed the static stall angle. At higher pitching rates (reduced frequency of $k = 0.04$) the blade loads were observed to deviate significantly from the static values even below the static stall angle (see left hand plot in figure 3.4). It was noted that changing the reduced frequency did not result in any increase in the peak load but the loading curves suggest that there could be an increase in unsteady loading relative to a quasi-steady blade operating below the static stall angle.

3.1.3 Induction factor

As the rotor extracts more energy from the incoming flow it creates a greater blockage. This effect is characterised by the induction factor, a, which for a

HAWT is defined by the relation $u = (1 - a)U_\infty$ where U_∞ is the free stream velocity and u is the wind speed at the rotor plane. For a VAWT it is a little more difficult to define the induction factor since there is no fixed rotor plane; the most simple definition uses the wind speed at the rotor hub. The general flow pattern created by the blockage effects of a VAWT can clearly be seen in the plot generated by the 2D vortex transport modelling code of McIntosh [2009] for a 3-bladed rotor at TSR=4 (figure 3.6).
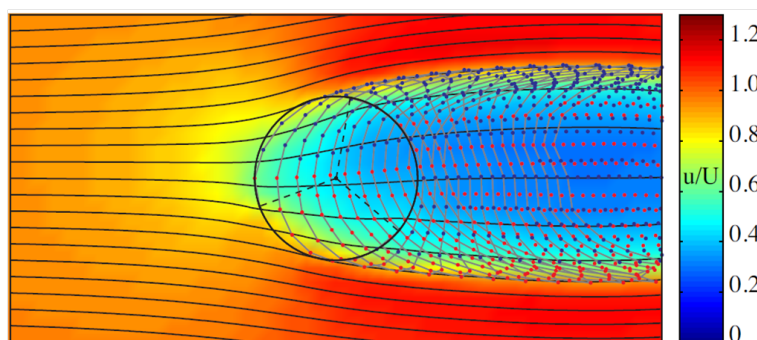
Figure 3.6: Plot showing the mean velocity relative to the free stream. The dots indicate the positions of the vortices that the code used to generate the velocity field [McIntosh, 2009]

An increase in the induction factor has two effects on the performance of a VAWT. The first is to reduce the free stream velocity in the downstream half of the rotor, resulting in an effective increase in TSR, and hence a drop in the blade angle of attack. The second effect is that the increased blockage causes a deflection of the incoming flow in the upstream half of the rotor. This also results in a decrease in the angle of attack experienced by the blades. These two effects were shown very clearly in the experiments carried out by Edwards et al. [2012]. These experiments used PIV to examine the flowfield around a model scale VAWT with three straight blades, which enabled the blade angles of attack to be accurately measured (see figure 3.7). At TSR=2 the measured angle of attack was within 5deg of the geometric angle, which is an error of approximately 20%. At TSR=4 this error had increased to more than 7deg, which is an error of at least 50%. These results show the importance of accurately determining the true angle of attack if the performance, or sound sources on a VAWT are to be correctly identified.

The induction factor is strongly dependent on the design of the rotor and and is influenced by both the TSR and the rotor solidity (see section 3.2.1). It is clear from the plots in figure 3.7 that the blockage effects can have a significant impact on the aerodynamics of a VAWT rotor and hence are likely to affect the noise radiation.

Figure 3.7: Comparison of geometric and measured angle of attack for two different TSR cases showing the effects of increased blockage with TSR, from Edwards [2012]

3.2 VAWT Rotor Design Parameters

There are a large number of design parameters that can be adjusted to change the performance of a VAWT rotor. An outline of these variables, and their impact on the rotor aerodynamics is presented below. It will be seen that there is a significant amount of scope to change the TSR at which peak power is achieved, and this raises the possibility that a rotor could be designed such that the maximum power output and minimum noise output coincide.

3.2.1 Rotor Solidity

The rotor solidity is defined as the ratio of blade area to rotor swept area, $\sigma = Bc/R_0$, where B is the number of blades, c is the blade chord and R_0 is the rotor radius. (It is worth noting that the solidity is sometimes defined as $\sigma = 2Bc/R_0$.) There are two ways in which the solidity can be adjusted: changing the ratio of blade chord to rotor radius or changing the number of blades.

Increasing the solidity will result in greater blockage of the flow, causing a change in the incoming flow velocities and blade angles of attack. In addition the greater blade area will result in higher levels of parasitic drag. The higher blockage results in lower angles of attack in the upstream half of the rotor which means that the TSR at which the blades no longer stall decreases to a lower value. This tends to move the peak power coefficient to lower TSR, but the continued drop in angle of attack as TSR increases means that the aerodynamic torque generated is less than for a lower solidity rotor at high TSR. The increase in drag with increased solidity also causes the power to drop even further at higher TSR relative to a lower solidity rotor. The combination of these effects means that the

43

peak in power coefficient is much sharper for a high solidity rotor(see figure 3.8). In general it is better to have a broad peak in the C_p curve since this means that the rotor speed does not have to be so closely controlled to achieve the optimum power output.
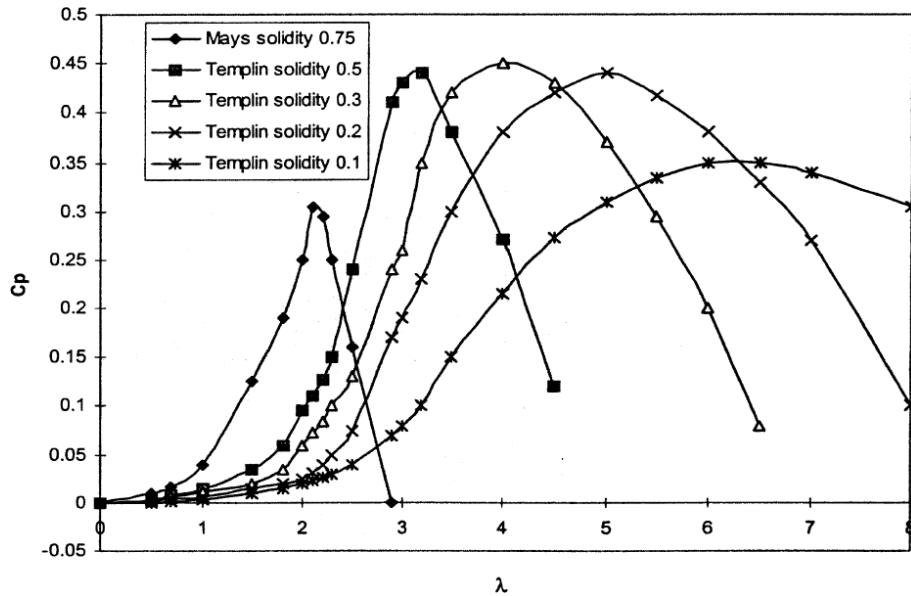
Figure 3.8: Variation of C_p curve for VAWTs with different solidities as measured by Mays and Templin [Kirke, 1998]. In this figure the x axis (λ) shows TSR.

Straightforward, analytical calculations show that increasing the number of blades has the advantage of producing a smoother torque profile and reducing the vibration loads on the turbine tower.

3.2.2 Rotor Aspect Ratio

The rotor aspect ratio is defined as the ratio of the rotor span to the rotor diameter. A low aspect ratio has the advantage of giving a high swept area while maintaining a lower angular velocity, thereby reducing the centrifugal loading on the blades. Since the centrifugal blade loads are often significantly greater than the aerodynamic loads, a lower angular velocity can help reduce the structural demands placed on the blades. The high aspect ratio of the WindSpire turbine, shown in figure 3.9, results in relatively high angular velocities being required. The structural implications are illustrated by the large number of spokes required to support the blades. This high number of spokes potentially increases the parasitic drag, reducing the peak power coefficient.

Figure 3.9: Photo of the high aspect ratio WindSpire turbine (image from the WindSpire website)

The main potential advantage of a high aspect ratio is the reduction of the impact that the blade tip vortices would have on blade loads. From a noise generation perspective this could help to reduce the impact of blade vortex interaction noise (see section 2.4.1).

3.2.3   Blade Profile

Since a VAWT aerofoil experiences both positive and negative angles of attack it is common for a symmetrical aerofoil to be used, such as one of the NACA-00XX series. The NACA-0012 and NACA-0015 are often used simply because there is a large amount of performance data available for them, which makes the aerodynamic design process easier. It has been suggested that a specially designed blade, such as a laminar flow aerofoil or a cambered profile, could improve the performance of a VAWT, but as yet no significant advances have been made (see Edwards et al. [2012]; Klimas [1992]).

Keeping a symmetrical profile but increasing the blade thickness has also been proposed. This has the structural advantage of increasing the blade stiffness, which would make it possible to have longer blade spans and/or higher rotational speeds. McIntosh [2009] used a 2D VTM code to estimate the potential change in the power coefficient for a 3-bladed rotor with different symmetrical NACA-00XX blade profiles. It was suggested that the thinner blades, which had lower zero-lift drag, had higher peak power coefficients that were at higher TSR. The C_p curves

for the thin blades however, had much sharper peaks than the thicker blades, as shown in figure 3.10(a). The broader peak for the thicker blades was seen to be advantageous as it would mean that the turbine could more easily be kept near its peak power output in variable wind conditions. Due to the importance of 3D effects it is uncertain whether this trend in performance would be observed on a real VAWT.
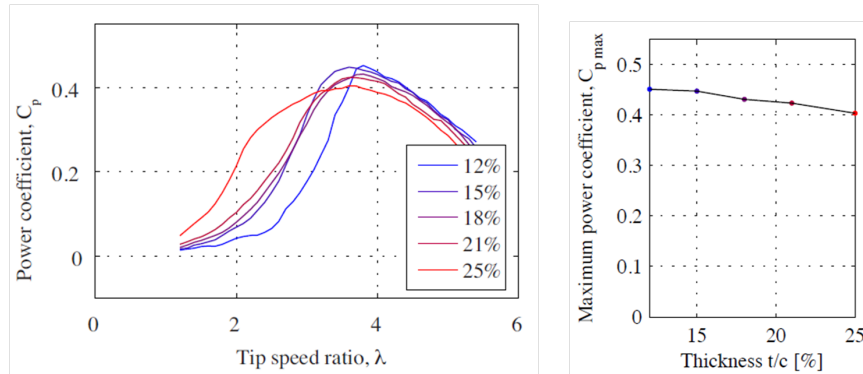
Figure 3.10: Variation in power coefficient for different symmetrical NACA aerofoils computed using a 2D VTM model McIntosh [2009]

McCroskey et al. [1982] conducted a systematic review of the static and dynamic lift performance of eight aerofoils. They found that the aerofoils with higher static stall angles also performed better under dynamic stall conditions. The cambered SC1095 and HH-02 aerofoils (developed for helicopters) were observed to reach higher peak lift coefficients than the datum NACA-0012 before stalling and also had narrower hysteresis loops in the lift coefficient, which implies a higher mean value of lift. In particular these two cambered aerofoils performed significantly better than the symmetrical NACA-0012 for the light dynamic stall case ($\alpha = 5 \deg + 10 \sin(\Omega t) \deg$), where there was barely any hysteresis in their lift curves. For application on a VAWT a cambered aerofoil would only have an advantage in one half of the rotation due to the reversal in the angle of attack. If the majority of the torque was being generated in the upstream half of the rotor however, it could be worth optimising the blade for this half of the rotation and neglecting the downstream half of the rotor. In addition, the unsteady loads due to dynamic stall are seen to be worst in the upstream half of the rotor, and if these could be reduced there might also be a reduction in noise radiation.

3.2.4 Preset Pitch

The problems of dynamic stall on a VAWT could be completely avoided if the blades could have their pitch varied with azimuth to achieve the optimal angle of

attack around the whole revolution. Constantly varying the pitch would however, be extremely mechanically challenging, particularly since the amount by which the pitch had to be adjusted would be a function of TSR. An alternative approach that has been tested is to give the blades a fixed preset pitch angle. The pitch angle, β, is defined as shown in figure 3.11. Fixing a pitch angle in this way can be thought of as a translation of the angle of attack curve up or down by exactly the preset pitch angle. This means that a negative pitch angle will reduce the peak angle of attack in the upstream half of the rotor, but increase the negative peak in angle of attack in the downstream half of the rotor.

A negative preset pitch would have a number effects on the blade loading experienced:

1. By reducing the angle of attack in the upstream half of the rotor, the onset of dynamic stall would be delayed. This would result in the blade producing torque for a greater portion of the revolution. Since the lift force produced as the blade approaches the most upstream location acts increasingly in the direction of rotation, maintaining attached flow in this region could result in a significant increase in torque output. Coton et al. [1996] showed that this effect results in the torque curve being shifted to higher azimuth and also increases the peak torque in the upstream half of the rotor.

2. In the downstream half of the rotor the blades would experience increased negative angles of attack, so the onset of dynamic stall would be earlier than for zero pitch angle. This results in a decrease in the amount of torque produced in the downstream half of the rotor, and could result in more unsteady loading for this portion of the rotation.
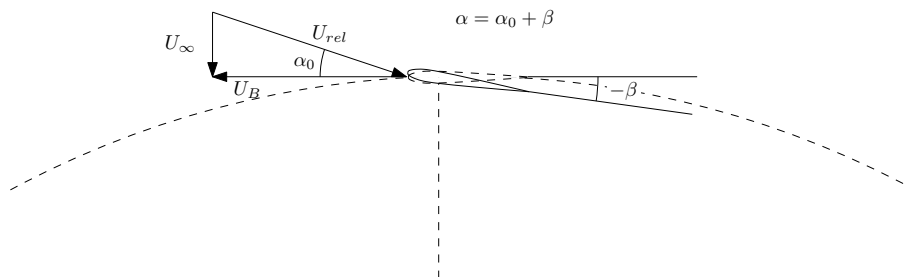
Figure 3.11: Definition of the preset pitch angle illustrating the impact on the blade angle of attack. The pitch angle shown is defined as a negative preset angle.

Both the experiments of Klimas and Worstell [1981] and the simulations performed by Coton et al. [1996] indicate that there is a small increase in peak power

coefficient for a preset pitch angle of -2deg. Coton et al. [1996] also noted that there is a significant reduction in the extent of dynamic stall in the upstream half of the rotor at TSR=2. Since the blade loads are generally higher in the upstream half of the rotation, this effect could be useful for broadening the peak of the C_p curve. In addition, if dynamic stall in the upstream half of the rotation is found to be a major noise source, a negative preset pitch angle could be a potentially effective mitigation technique.

3.2.5 Blade Sweep and Curvature

Blade curvature arises from having a variable radius. Early VAWT designs often adopted curved blades that described a shape known as a troposkein, which is the shape formed when a skipping rope is spun around a vertical axis, and accounts for the effects of both centrifugal and gravitational loading. This shape results in the blades experiencing no bending moment, which is a significant advantage from a structural design perspective. From an aerodynamic perspective, the reduced radius at the two ends of the blades means that they experience a lower TSR and a lower relative blade velocity than the mid-span of the blade. The simulations of Scheurich [2011] actually indicated that a curved bladed rotor would have a higher power coefficient than a straight bladed turbine with the same aspect ratio. The reasons for this increase were not examined but it might be supposed that the lower blade velocity at the tips reduced the amount of drag. Since the blade tips of the straight bladed rotor are less heavily loaded than the mid-span, this reduction in drag could more than offset the loss of torque from the reduction in blade radius.

Curving the blades in at the tips also has the advantage of ensuring that the downstream blades do not intersect the tip vortices shed from the upstream blades. The vortices shed from the tips of the upstream blades are advected towards the blade mid span as they move downstream. When the blade tips are curved in however, these tip vortices might remain outside the rotor swept area as shown by the VTM simulations of Scheurich [2011, p.120]. This is potentially significant from the point of view of noise generation.

Blade sweep is the rotation of the blades so that they are no longer parallel to the rotor axis. If the blades are designed to have a constant radius the result is that the blades are helically twisted about the rotor axis. The key feature of a swept bladed rotor is that each section of the blade is at a different azimuthal angle. As a result the peak load does not occur simultaneously along the whole blade, but is spread across a portion of the rotation. From a structural design point of view this has the major advantage of smoothing the rotor loading and torque profiles which reduces vibration and fatigue problems. The spreading of the loads may also be advantageous from a noise generation point of view. If the

blade is considered as a number of point sources distributed along the span, for a straight blade all of the sources are in phase, whereas on a swept blade they are all slightly out of phase. If unsteady blade loading is a strong source this phase shift might result in lower noise radiation.

A further interesting effect of blade sweep is its potential impact on dynamic stall behaviour. In his discussion of dynamic stall on helicopter rotors Leishman [2006, chap.9] presents experimental data that indicates that a blade sweep of 30deg delayed dynamic stall of a NACA-0012 blade to an angle of attack that was almost 5deg higher than for an unswept blade. The hysteresis loop in the lift curve was also narrower, which yielded a higher mean value of lift for a full blade oscillation. In addition, the noise radiated due to scattering at the trailing edge is related to the chordwise Mach number, which will be lower for a swept blade than a straight blade.

Blade sweep and curvature appear to offer both structural and potential noise radiation advantages over straight bladed rotors. The main disadvantage however is the increased cost of manufacture. Based on investigations carried out for the experimental model used in this study a curved, swept blade would cost much more than an equivalent straight blade.

3.3 Modelling VAWT Performance

Computational models of VAWT performance are a useful tool for informing the design of a VAWT rotor. Computationally light methods, such as actuator disc models, are particularly effective for gaining information about global rotor performance, but they are limited to low rotor loading cases [McIntosh, 2009]. These models also do not provide detailed information about the variation in blade loads with azimuth, and do not capture effects such as blade-wake interaction. From a noise generation point of view these models are of little direct use since it is the small scale, unsteady components of the flow field that are likely to be most important. Their application is briefly described below however, since they are historically of general importance in the area of VAWT performance modelling.

Computational fluid dynamics (CFD) methods can provide the high fidelity information required for making estimates of both rotor performance and sound radiation. These direct solution methods are very computationally expensive however, due to the high spatial and temporal resolution required to model both the small scale interactions around the blade chord and the large scale wake development. Some CFD models investigating both the performance and the sound radiation are discussed in section 3.3.2.

Vorticity transport models are capable of modelling the global 3D flow field around a VAWT rotor while not being excessively computationally expensive.

The blade loads can be modelled to a relatively high resolution, which raises the possibility of using these data as the input for a noise model. An outline description of how the vortex transport model works and the results of some significant studies are given in section 3.3.3.

3.3.1 Actuator Disc Models
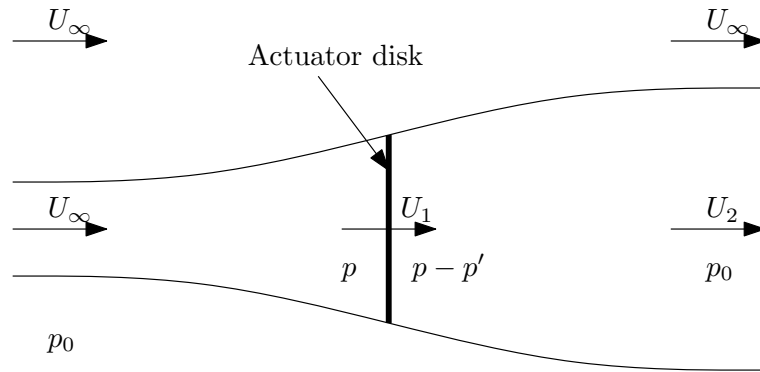
Figure 3.12: Schematic of the actuator disk model for a HAWT.

The concept of the actuator disc was first developed by Glauert [1948]. A simple illustration of the actuator disc concept for a HAWT is shown in figure 3.12. It is a very useful tool for computing the mean flow parameters through a device which is transferring energy either into or out of a fluid. The flow through the disc can be solved by applying Bernoulli's equation and the conservation of momentum and energy. The key parameter is found to be the induction factor a, which is defined below as

$$a = 1 - \frac{U_2}{U_\infty}. \tag{3.1}$$

The basic 1D actuator momentum model is limited to cases with low disc loading since, as the induction factor increases above $a > 0.5$, the model predicts unphysical flow reversal in the wake. Moriarty and Hansen [2005] showed that in this condition, known as the 'turbulent wake state', there is increased entrainment of fluid from the free stream into the wake due to the high levels of turbulence. A simple empirical correlation was developed by Glauert [1926] to correct for this error, based on data from measurements of thrust on an experimental airscrew.

The application of a simple 1D momentum model to VAWTs is much less straightforward since the rotor does not consist of a simple disc and there is a significant variation in the flow parameters over the rotor's swept area. Various models have been developed to try and overcome these difficulties (e.g.

50

Paraschivoiu [1981]; Strickland [1975]; Templin [1985]). These models involve splitting the VAWT rotor into multiple actuator discs that account for the differences between the upstream and downstream halves of the rotor, and also for the azimuthal variations. Even the more advanced versions of these actuator disc models are largely limited to low rotor loading cases as they often fail to converge at high blade loading. McIntosh et al. [2009] developed a similar approach that was capable of solving high rotor loading cases, although they admitted that the model still had a number of shortcomings, particularly for modelling high resolution blade loading and blade-wake interactions.

3.3.2 Computational Fluid Dynamics

As previously mentioned, the simulation of VAWT aerodynamics using CFD is computationally very demanding. The continual variation in the blade angle of attack with azimuth means that the temporal and spatial resolutions must be high enough to capture the short period, small scale features of the flow such as dynamic stall and blade-wake interaction. In order to accurately model the flow in the downstream half of the rotor it is then necessary to represent the propagation and growth of the wake through the rotor volume.

Ferreira [2009] compared the results from CFD simulations of a VAWT using Unsteady Reynolds Averaged Navier-Stokes (U-RANS), Large Eddy Simulation (LES) and Detached Eddy Simulation (DES). It was found that the high frequency components of the blade loads were very sensitive to the model used. U-RANS was limited by its ability to accurately model the development of the large scale eddies passing through the rotor and so made poor predictions of the downstream blade loads. In addition, both Ferreira [2009] and Wang et al. [2010] found that the results from U-RANS simulations were sensitive to the turbulence model used. Both the LES and DES models made better predictions of the wake development, but were very sensitive to the details of the vortex shedding from the upstream blades. The LES model was found to perform worse than the DES model, which was thought to be a result of the more detailed near-wall model in the DES simulation.

Danao [2012] used a U-RANS method in the CFD solver ANSYS 13.0 to investigate the flow through a VAWT rotor. The sensitivity of the model to a range of parameters including the temporal and spatial resolution was investigated. It was found that at TSR=2, where there was significant unsteadiness caused by dynamic stall, the model output was very sensitive to these parameters and high resolutions were required to capture all the features of the flow. As in the other U-RANS studies, Danao [2012] also found that the output of the simulations was sensitive to the exact turbulence model implemented. In order to exactly predict the sound field from blade loading results very high resolution data would be

required, and the degree of uncertainty in the CFD models means that this is probably not feasible.

One result from CFD that is potentially interesting from the point of view of noise generation is that of Castelli et al. [2011], who simulated the flow through a VAWT rotor using a RANS method and looked in particular at the impact of the wake shed by the rotor hub. These simulations suggested that the wake shed by the rotor hub is significantly more intense than that shed by the blades for TSR = 2.33 (see figure 3.13). There is some corroborating evidence that this effect might be significant in the blade torque data of Danao [2012], where there appears to be an impulsive load as the blade passes directly downstream of the hub. This is one feature of VAWT rotor design that might be worth examining in the experimental program with regards to its impact on noise generation.
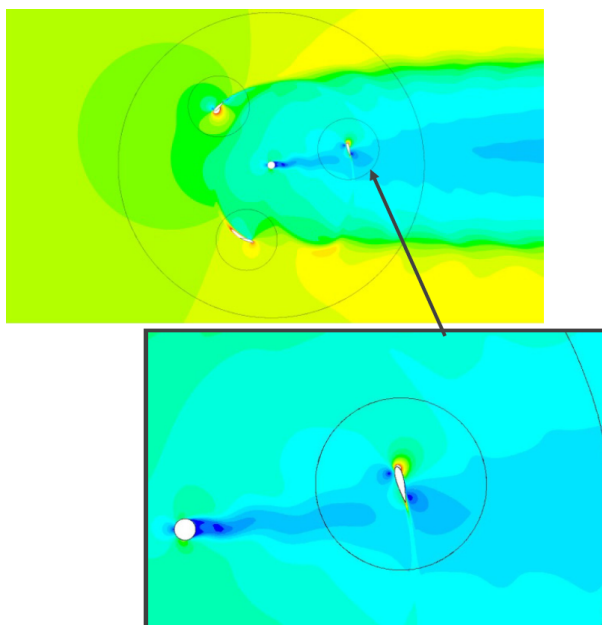
Figure 3.13: Plot of absolute velocity magnitude in m/s showing the relative significance of the wake shed by the rotor hub [Castelli et al., 2011].

3.3.3 Vorticity Transport Models

A VAWT typically operates at low Mach numbers, and the Reynolds number is high enough to neglect viscosity away from solid boundaries. The wake of a VAWT rotor can therefore be well modelled by taking the curl of the Navier-Stokes equations, such that they explicitly represent the evolution of vorticity. The wake of each individual blade can then be modelled as a train of point vortices, and by summing the contributions of each of these vortices and the free

stream velocity one can determine the whole velocity field. This is the fundamental concept used in a vorticity transport model (VTM) and allows complex wake structures to be modelled in a computationally efficient way.

The key step in this model is the method for accurately determining the vorticity shed from the blades. The flow around the blades can be modelled in detail using a CFD solver and then far from the solid boundaries the conservation of vorticity is applied (see Whitehouse et al. [2010]). A second, faster approach is to use lifting line theory, as described by Prandtl [1918]. While this method requires less CPU time than using CFD, it does require careful implementation to accurately capture effects such as dynamic stall [McIntosh, 2009; Scheurich, 2011]. Both McIntosh [2009] and Scheurich [2011] present thorough descriptions of the detailed operation of the VTM and the reader is referred there for further information.

The VTM developed by McIntosh [2009] models the 2D flow through a VAWT rotor, but cleverly accounts for phenomena such as blade sweep and finite blade aspect ratio. The 2D model was used to reduce the computational time since the objective was to perform a parametric study of the factors influencing VAWT rotor performance. This method does not however, deliver such detailed information on the complex blade-wake interactions.

The 3D vorticity transport model implemented by Scheurich [2011] for modelling VAWT aerodynamics was originally developed to model the wakes produced by helicopters [Brown, 2000; Brown and Line, 2005]. It has been used to perform a detailed investigation of the 3D flow around 3 different VAWT rotors, with the output being validated against the experimental blade load data of Strickland et al. [1981]. As mentioned previously, the key strength of the VTM is its ability to accurately model the wake, and the 3D simulations yielded some interesting results regarding the blade-wake interactions in the downstream half of the rotor.

Scheurich [2011] modelled a 3-bladed rotor with straight blades and plotted the horizontal and vertical components of the wake vorticity (see figure 3.14). One of the key features highlighted by the 3D simulations is the impact of the tip vortices, which can be seen to interact strongly with the blades in the downstream half of the rotor. This is consistent with the computational and experimental work of Ferreira [2009] who also found that the vorticity shed by the blades in the upstream half of the rotor interacts with the downstream blades. This is particularly significant for noise generation, since the unsteady loading caused by blade-wake interactions has been shown to be a potentially strong source of noise [Schmitz and Yu, 1986].

Scheurich [2011] simulated a range of TSR and found that as the TSR increased the tip vortices advected further towards the mid-span of the downstream blades. In addition, the vortices were much more closely spaced making it more likely that the downstream blades would interact with this shed vorticity. The
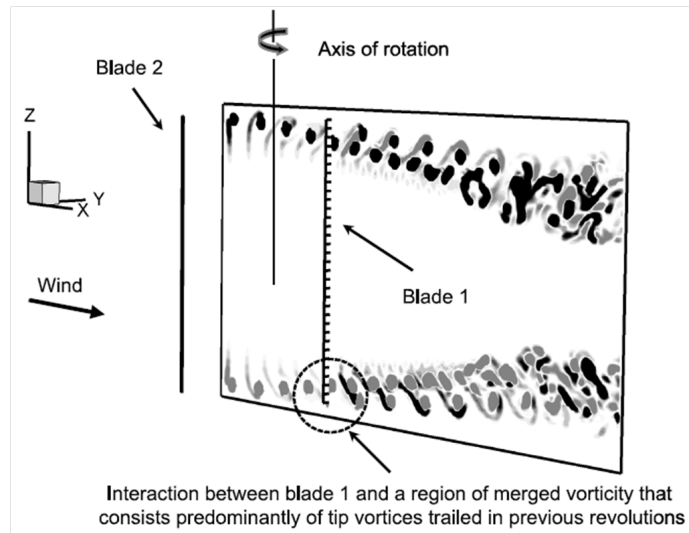
(a)   Vorticity on vertical plane through rotor hub aligned
with the free stream direction
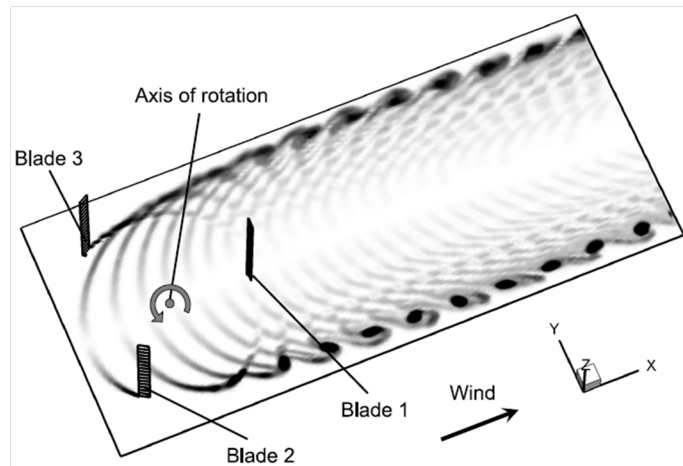
(b) Vorticity on horizontal plane at blade mid-span

Figure 3.14: Plots showing the wake vorticity for a straight bladed rotor at
TSR=3.5 Scheurich [2011]

54

Figure 3.15: Plot showing the variation in angle of attack on a 3-blade, straight bladed rotor at TSR=7.5 at multiple locations along the blade span. [Scheurich, 2011, p.79]. The characteristic BVI signal has been highlighted and is seen to extend across the full span of the blade.

implication was that blade-wake interactions are likely to become more significant at higher TSR than at low TSR. The plot of the blade angle of attack in figure 3.15 shows that at TSR=7.5 a straight bladed rotor experiences blade-wake interactions over the whole span as indicated by the characteristic BVI signature in the angle of attack.

3.4 Summary of Implications for Noise Generation

This chapter has presented some of the key concepts relating to the aerodynamics and design of a VAWT rotor. A number of concepts were highlighted as being potentially significant from a noise generation or mitigation perspective and these are summarised below:

1. **Dynamic stall:** Both experimental and computational studies have indicated that during dynamic stall an aerofoil can experience significantly unsteady loading. Unsteady forces radiate sound, and the rapid loading

55

fluctuations observed during dynamic stall are likely to be a particularly intense sound source.

2. **Blade wake interactions:** The vorticity transport model simulations indicated that there are potentially significant interactions between the the wake from the upstream half of the rotor and the downstream blades. In particular, the intense vortices shed from the upstream blade tips are seen to cause strong blade vortex interactions. These interactions with the tip vortices were shown to be more intense at higher TSR [Scheurich, 2011].

   Another possible region of blade wake interaction was highlighted by Castelli et al. [2011] who suggested that the wake shed by the rotor hub could result in a strong blade wake interaction noise.

3. **Noise mitigation options:** There are a number of ways in which the design of the rotor can be altered to potentially mitigate the two noise sources described above. Dynamic stall can be avoided either by simply operating at high TSR or, if low TSR is desirable, a blade preset pitch angle can delay the onset of dynamic stall in the upstream half of the rotor.

   By spreading the loading around the rotor azimuth, blade sweep also may also help to reduce the intensity of the sound radiated by blade load fluctuations. Swept blades may also delay the onset of dynamic stall to some extent.

   Blade wake interactions are more difficult to avoid, but the VTM simulations of Scheurich [2011] suggested that curving the blades to reduce the tip radius can reduce the interaction between the downstream blades and the tip vortices shed in the upstream half of the rotation.

Chapter 4

Experimental Techniques

The overall objective of the experimental program was to use the phased acoustic array in the Markham wind tunnel to locate and identify the dominant sources of noise on a VAWT. An acoustic array consists of a large number of microphones that simultaneously sample the sound being radiated from a source object. By comparing the phase of the signals received at the different microphone locations it is possible to estimate the location and magnitude of the noise source. The experiments conducted in this study measured the sound field of a simple straight-bladed, model-scale VAWT.

This chapter first introduces the Markham wind tunnel and the acoustic array specification. The design of the model-scale VAWT presented a number of challenges and these are discussed along with the solutions adopted. The process of frequency domain beamforming is then described along with certain adaptations made to cope with the challenges of locating the sources on the VAWT model. Finally the details of the experimental cases that were tested are presented along with the exact data processing methods adopted for analysing the results. The results themselves are presented separately in the next chapter.

4.1   Wind Tunnel Model

This section first describes the wind tunnel facility used including the layout and specification of the acoustic arrays. The design of the model scale VAWT is then discussed and the choices of rotor configuration and operating conditions are explained.

4.1.1 The Markham Tunnel and Acoustic Arrays

The Markham wind tunnel is a closed section, recirculating tunnel with a top speed of 59m/s and a working section measuring 1.675m x 1.220m. In 2006 a pair of nested acoustic arrays were installed in the floor of the tunnel as described by Shin et al. [2007]. The low-frequency array is designed to operate between 1kHz-5kHz, while the high-frequency array is designed to operate between 5kHz-30kHz. The arrays each consist of 48 Linear-X M51 microphones, with six microphones being shared between the two arrays meaning that the arrays cannot be used simultaneously. The microphones have an outer diameter of 1/2inch, while the diaphragm is approximately 2mm in diameter and is exposed directly to the flow, having no protective cover. The microphones' temperature coefficient is -0.01dB/°C, which is sufficiently small that the signals are unaffected by the temperature rise experienced during operation of a recirculating wind tunnel. The layout of the two nested arrays is shown in figure 4.1.

The signals from all the microphones were simultaneously sampled at up to 250kHz by the GBM VIPER data acquisition system, which also provides the 10V DC power supply to the microphones. The system has built in low-pass anti-aliasing filters linked to the sampling frequency and programmable gain amplifiers with an 'autorange' function that automatically assigns an offset and gain to each channel in order to maximise the dynamic range on the 16 bit analogue-to-digital converter. There is also a choice of three high-pass filters at 1Hz, 650Hz and 5000Hz. The 650Hz filter is designed to filter out the wind tunnel fan noise from the low-frequency array signals and the 5000Hz filter is designed to eliminate a significant amount of the boundary layer noise from the high-frequency array signals.

The most common technique used for locating the noise sources is known as beamforming. This process calculates the source strength at a given location that is most compatible with the measured sound field. The method is particularly computationally efficient since it does not require any iteration [Quayle, 2008]. An outline of the procedures involved in conventional, frequency-domain beamforming is presented in section 4.2, based on the description given by Sijtsma [2004a] whose software was used in this study. In his investigation of landing gear noise, Quayle [2008] determined certain elements of the beamforming process that are specific to the Markham wind tunnel. Elements of the process relating to the Markham tunnel are therefore based on the methods outlined in his thesis.

4.1.2 Rotor Design

When designing the wind tunnel model it was necessary to try and match as many of the operating parameters as possible to the full scale model. This presented
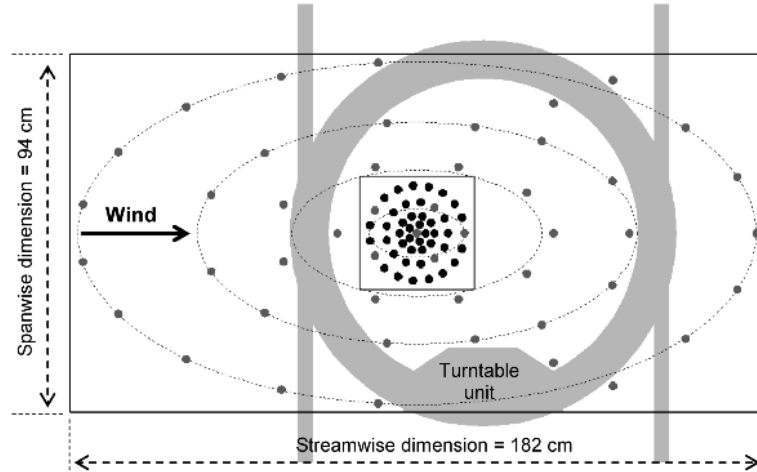
Figure 4.1: Schematic of the nested high frequency and low frequency arrays in the Markham wind tunnel. The LF microphones are grey and the HF microphones are those inside the grey square in the middle. The grey microphones within that square are the ones that are shared between the two arrays

certain problems since there are a number of non-dimensional parameters that govern the flow field around a VAWT (see table 4.1).

When designing the model VAWT it was not clear what the dominant source was going to be. The aerofoil self-noise and turbulent inflow noise are related to the blade Mach number, which is fixed by the wind speed and the TSR. These parameters can be made similar between the full scale and model VAWTs. If the blade loads as a function of blade azimuth are assumed to be similar between the full scale and model VAWTs then the periodic, fluctuating force component of sound will be proportional to the angular velocity, since this will determine the rate of change of the force. Achieving the desired TSR with the small radius of the model VAWT rotor requires a much high angular velocity than the full scale rotor (the ratio of angular velocities is simply equal to the ratio of rotor diameters). It might be expected therefore that the component of noise radiated by the periodic blade loading fluctuations would be relatively louder for the model scale VAWT.

High rotational velocities have some advantages with regards to making measurements with the acoustic array. The spatial resolution of the array measurements is inversely related to the frequency of the radiated noise (Sijtsma [2004a], see figure 4.6). The fundamental frequency of the sound generated by the model was expected to be the blade passage frequency, which is equal to the number of blades times the angular frequency of the rotor. Therefore the faster the rotor

Dimensionless Parameter	Definition	QR5	Model VAWT
TSR	U_∞/U_B	1-5	1-5
Re	$\rho U_B c/\mu$	$1.8 \times 10^5 \to$ 7.2×10^5	$0.6 \times 10^5 \to$ 2.0×10^5
Rotor Solidity	Blade area / total swept area	0.1	0.12
Rotor Aspect Ratio	Rotor height / rotor diameter	1.67	1.07

Table 4.1: Dimensionless parameters defining the operation of a VAWT including a comparison between their values for the full scale QR5 rotor and the wind tunnel model

was spun the better the resolution of the measurements that could be made. This presented some interesting problems for model design due to the large centrifugal forces generated by rapidly spinning bodies.

4.1.3 Tunnel Blockage

The limiting dimensions of the VAWT model were determined by the constraint of wind tunnel blockage. Tunnel blockage is defined as the ratio between the model cross section and the tunnel cross section. Ideally, for a solid model, the blockage ratio should be of the order of 5% [Chen and Liou, 2011]. The Markham wind tunnel has dimensions of $1.675m \times 1.220m$ giving a cross sectional area of $2.044m^2$, meaning that the cross section of a solid model should be of the order of $0.1m^2$.

For rotating machines, such as turbines or propellers, the blockage is normally defined as the ratio of swept area to tunnel area, but since the swept area is not solid the 5% ratio no longer applies. Howell et al. [2010] found that, for a VAWT, a blockage ratio of up to 14% had a negligible impact on the flow field over a range of TSR. A blockage ratio of 14% in the Markham tunnel gives a maximum swept area of $0.286m^2$. Assuming that the rotor is roughly square this gives a dimension of 0.535m for the blade span and rotor diameter.

4.1.4 Blade Design

The main constraint on the design of the blades was the centrifugal loads. Given that the rotation speed needed to be as high as possible this meant that the blades
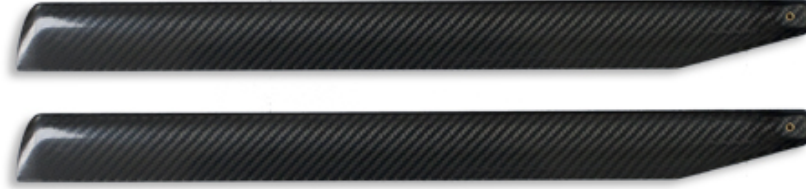
Figure 4.2: NHP Razor Pro carbon model helicopter main rotor blades
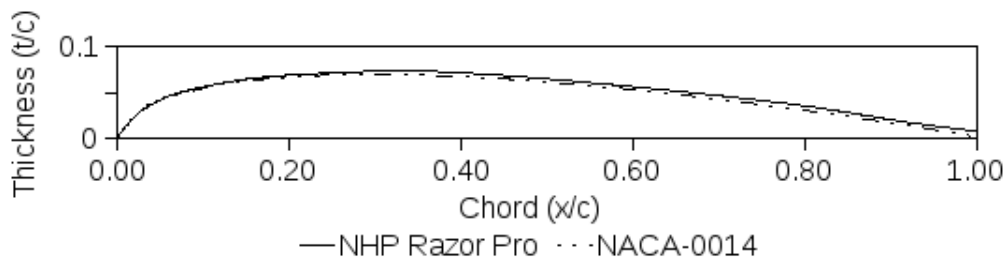
Figure 4.3: Comparison of the NHP Razor Pro blade profile with the NACA0014 profile.

had to be light and stiff. In terms of material selection, the parameter of interest was therefore the specific stiffness E/ρ, where E is the Young's modulus and ρ is the density. Consequently materials like carbon fibre were the best choice for the blades.

Due to the aerodynamic behaviour of a VAWT rotor, the blades typically have a symmetrical profile (The QR5 turbine shown in 1.4(a) uses a NACA-0018). As discussed in section 3.2.3 the shape of the blade has been shown not to significantly alter the overall performance of the rotor, so obtaining a specific aerofoil profile was not seen as a design priority.

Research into prefabricated carbon fibre aerofoils found that model helicopter rotor blades satisfied almost all of the design criteria for the blades of the model scale VAWT. The blade chosen was the NHP Razor Pro Carbon main rotor blade, which has a span of $L = 630mm$ and a chord of $c = 55mm$ (see figure 4.2). These components were made from a skin of carbon fibre approximately 1mm thick with a core of closed cell foam. The exact blade profile was not known, but was symmetrical, with a very similar profile to the NACA0014, as shown in figure 4.3. The attachment for fixing the blade to the helicopter hub was cut off leaving a square blade tip and reducing the span to $L = 536mm$. The opposite blade tip was left in its original, curved configuration as this would possibly highlight whether the blade tip shape had any significant effect on the sound field radiated.

Structural beam calculations were carried out to assess the peak bending

moment in the blades and thereby determine the optimum location for the spoke attachments. Assuming a stress concentration factor of 3 at the holes for the spoke attachments, the optimal location for the spokes was found to be 91mm from the blade tips. Since the centrifugal loads were much greater than the aerodynamic loads, the spokes were attached in line with the centre of mass rather than the centre of lift. The beam calculations also determined a limiting rotational velocity due to the strength of the blades, which was approximately 2200rpm. Finite element modelling carried out by Neil Houghton in the Cambridge Engineering Department design office supported the simple beam loading calculations, but highlighted the issue of model vibration and resonance.

4.1.5 Boundary Layer Trips

The investigation of potential noise sources presented in chapter 2 suggested that laminar boundary layer noise might be significant on the wind tunnel model. In their investigation of helicopter rotor noise Paterson and Amiet [1982] found that this source could easily be avoided by installing a simple boundary layer trip. They used an 8mm wide and 0.15mm thick strip of aluminium tape with its leading edge at 25% chord.

For the experiments conducted in this study a similar approach was adopted with a strip of aluminium tape placed at the point of maximum blade thickness. The strip was approximately 5mm wide and 0.15mm thick and was cut in a zig-zag, as this shape has been shown to give more rapid transition to turbulence than a straight strip of the same thickness [Hama, 1957].

4.1.6 Rotor Spokes and Shaft

The main objective when designing the spokes and the shaft was to make them as small as possible to minimise the amount of noise that they would radiate. For the spokes, this was achieved by using 6mm diameter steel rods with screw attachments at either end.

There was initially some concern that the cylindrical profile of the spokes would result in tonal vortex shedding noise. This was found not to be a problem since the radial nature of the spokes meant that every point on a spoke was experiencing a different relative flow velocity meaning a tonal noise would not be radiated.

The diameter of the shaft was also made small (25.4mm), which resulted in a very slender shaft ($L/D \approx 70$) meaning that shaft resonance had to be considered. Vibration tests were carried out to determine the natural frequency of the shaft, which was found to be approximately 15Hz without the motor assembly attached. Careful testing of the rotor was carried out prior to its installation in the wind
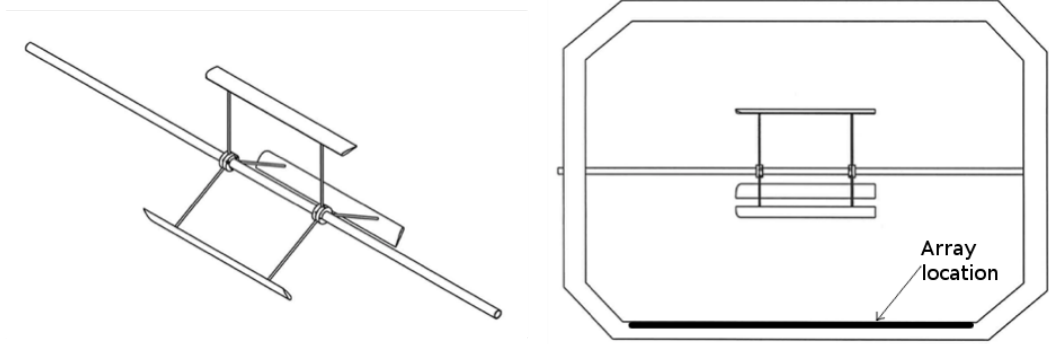
Figure 4.4: Schematics of the VAWT model designed for the wind tunnel experiments. The left hand image is an isometric representation while the right hand image is a scale drawing of the VAWT in the working section of the Markham tunnel.

tunnel and it was found that, with the motor assembly driving the rotor, it began to resonate at approximately 1000rpm (16.6Hz), which was in broad agreement with the vibration tests. As a result the rotor speed during the wind tunnel tests was limited to 900rpm (15Hz) to avoid excessive vibrations.

4.1.7   Motor Control System

For these experiments the aerodynamic performance of the model was only of secondary importance. It was expected that the model would not produce any positive torque, thus requiring it to be motor driven at all speeds and TSRs.

In order to investigate a full range of TSRs it was necessary to be able to accurately control the speed of the rotor. This was achieved by using a brushless servo motor with a rotary encoder connected to a four quadrant controller, meaning the rotor could be both driven and braked in both directions of rotation. This control system was provided by QuietRevolution Ltd and is very similar to the system used on their full-scale wind turbines.

4.2   Beamforming

The basic principle of any beamforming algorithm is to estimate the source distribution that produces a sound field that best matches the measured data. The key components of the process are therefore the artificial source/propagation models and the method used for comparing the real and simulated sound fields. This process can be conducted in either the time or frequency domain. In the time domain it is commonly known as Delay-and-Sum beamforming since the algorithms

aim to estimate the time delay between the sound arriving at a pair of microphones in order to determine the angle of arrival of the sound. In the frequency domain, the beamforming algorithms perform exactly the same task, but do so by comparing the phase of the signal arriving at each of the microphones.

4.2.1 Cross Spectral Matrix

The phase difference between the signals arriving at two microphone is captured by the cross spectra of the two signals. For a microphone array where there are multiple microphone pairs this information is represented by the Cross Spectral Matrix (CSM). The CSM is calculated by forming a vector of the complex spectral values for each microphone at a given frequency line and then computing the matrix formed by multiplying this vector by its Hermitian transpose[1]. This captures the phase relationship between the signal received at each microphone, m, and each other microphone in the array, n.

$$CSM = C_{mn}(f) = \frac{1}{2}P_m(f)P_n^*(f) \tag{4.1}$$

where $P(f)$ is the complex pressure amplitude at discrete frequency f and the star indicates the Hermitian transpose of a vector.

4.2.2 Fourier Transforms

Before the CSM can be calculated the first task is to convert the time series data into the frequency domain using a Fourier transform. There are a number of parameters that can be changed in the process of computing the spectra and it is important to choose these variables carefully in order to achieve the best results from the beamforming process. When performing the Fourier transform the time domain signal is broken down into a number of blocks whose size is set to a power of two in order to make best use of the Fast Fourier Transform (FFT) algorithm. For each block, an FFT is carried out and the CSM is computed at every frequency within the range specified. The mean CSM is then calculated for every frequency.

A smaller blocksize means that more blocks can be taken from a given sample, giving more averages. This is very important in the presence of random noise, since the average value of the cross-spectrum of uncorrelated, random noise is zero; hence the more samples that are taken the closer the noise component of the spectrum will approach this minimum. If the signal is not perfectly periodic then it is necessary to use a windowing function in order to avoid introducing

---

[1]The Hermitian transpose is defined as the complex conjugate of the regular transpose

noise due to the otherwise square window. Also, if the signal is not periodic, an overlap between the FFT blocks is used, which has the advantage of increasing the number of averages that can be taken from a given sample. The signal processing algorithms within the beamforming code allow the user to apply a Hanning window and by default use a block overlap of 50%. This approach was adopted in all of the signal processing in this study unless otherwise stated.

The array microphones in the Markham tunnel are flush mounted in the floor so are strongly influenced by the turbulent pressure fluctuations in the boundary layer. In many cases this pressure signal can be much louder than the acoustic pressure signal that one is trying to measure. For the case of the VAWT model the source signal was often much louder than the background noise (see section 4.2.6), but the source signal did contained a stochastic, broadband component. The averaging process was therefore still necessary to determine the mean level of this part of the signal.

A small blocksize gives more averages from a given signal but limits the frequency resolution, δf, of the spectra since it is related to the sampling frequency, F_s, by $\delta f = F_s/$Blocksize. In order to maintain a sufficiently high frequency resolution there is consequently a trade off when choosing the blocksize between higher resolution and more averages. Another way to obtain a large number of averages is to increase the length of the sample in the time domain. The limitation in terms of sample length is effectively enforced by the computational time required to process the resulting time series.

An investigation was conducted to determine the number of averages required to find the mean broadband level. The 3-bladed rotor was run at TSR=2 and the sound was recorded for 2mins at a sampling frequency of 23.1kHz. The cross-spectra of microphones one and two was then computed using a blocksize of 8192 for a range of averages and the results are presented in figure 4.5. There is a clear, if small, convergence of the broadband component of the signal above 3kHz. The spectra between 1kHz-3kHz don't appear to converge at all however, which implies that this component of the spectrum is deterministic in nature. The implication is that, while the signal from the model is greater than the background noise, the spectrum can be computed with fewer than 100 averages. This allowed a very large blocksize of 65536 to be used for examining the harmonic component of the spectra, which gave 74 averages from a 2min sample.

The cyclical loading fluctuations on a rotating source, such as a wind turbine, are a fundamentally periodic noise source. The Fourier transform of this periodic portion of the spectrum can potentially be more exactly calculated if the exact period of the signal is used as the FFT blocksize. The VIPER data acquisition system is capable of carrying out synchronised sampling using a once-per-revolution signal from the rotating shaft. This synchronised sampling works by recording the microphone signals at the highest possible sampling rate and
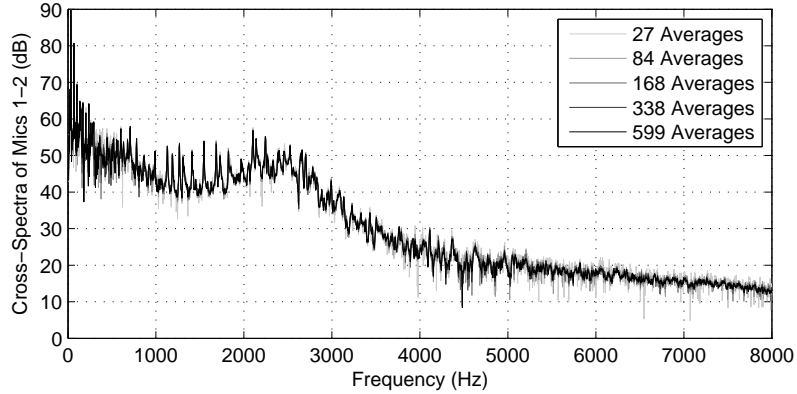
Figure 4.5: Plot of the spectra for the 3-bladed rotor operating at TSR=2 showing the convergence of the broadband component of the signal above 3kHz with increasing number of averages.

then interpolating the data between two clocking pulses from the shaft to give a fixed number of equally spaced samples per revolution. By setting the number of samples per revolution to be a power of two and using no windowing or overlap in the FFT an 'exact' Fourier transform of the periodic signal can be calculated. This results in the frequency resolution of the Fourier transform being equal to the angular frequency of the rotating shaft.

4.2.3   Beamforming Process

The first stage of the process of beamforming is the definition of a scanning grid. The scanning grid is an array of points at which the beamforming algorithm evaluates the source strength, and should contain the locations of the sources of interest. The algorithm assumes that a source exists at each point in the scanning grid and estimates the source strength that provides the closest match between the measured sound data and predicted sound field from a source at that point.

The sources in the scanning grid are often assumed to be monopoles as this allows the frequency domain definition of a monopole source, given in equation 4.2, to be used. In this expression a is the source amplitude and the term $\Delta(t_e)$ is defined in equation 4.4.

$$P_m(f) = \frac{ae^{-2\pi i f \Delta(t_e)}}{4\pi a_0} \tag{4.2}$$

$$P_m(f) = ag_m(f) \tag{4.3}$$

Dipole sources can also be used in the beamforming algorithm, but when

the microphones are located sufficiently far from the source there is virtually no difference in the appearance of a monopole and a dipole source since the incident waves are approximately planar is either case [Sijtsma et al., 2001]. In the Markham tunnel it is not possible to make this far-field assumption, but for the case of the VAWT rotor the monopole is still a more useful source model for reasons discussed at the end of section 4.2.7.

The function $g_m(f)$ in equation 4.3 is known as the steering function. It describes the signal at each microphone due to a unit source and is also sometimes called the transfer function. a is then the complex amplitude of the source. If the source is at $\underline{\xi}$ in the scanning plane and the microphone is at $\underline{x_m}$ then the definitions of the time delay, $\Delta(t_e)$, and α are as follows:

$$\Delta(t_e) = \frac{-\underline{M} \cdot \underline{r} + \alpha}{c(1 - \|\underline{M}\|^2)} \tag{4.4}$$

$$\alpha = \sqrt{\underline{M} \cdot (\underline{r})^2 + (1 - \|\underline{M}\|^2)^2 |\underline{r}|^2} \tag{4.5}$$

where $\underline{r} = \underline{x_m} - \underline{\xi}$ is the distance from microphone m to a point in the scanning grid. If the source is not moving then $\underline{M} = 0$ and $\alpha = \underline{r}$.

For each point in the scanning grid the beamforming process estimates the source power, $A = \frac{1}{2}aa^*$, by minimising the expression,

$$J = \|C_f - A_f \underline{g}\underline{g}^*\|$$
$$= \sum_{m,n} |C_{mn} - Ag_m g_n^*|_f^2 \tag{4.6}$$

This calculation is carried out for each frequency computed in the FFT (as indicated by the subscript f), and for every scanning grid point. The solution for source strength at scanning grid point, ξ, is given by equation 4.7. By graphically representing these amplitudes a source plot can be generated, indicating the scanning grid locations where the array estimates the sound to be coming from.

$$A(\underline{\xi}) = \frac{\sum_{m,n} g_m^* C_{mn} g_n}{\sum_{m,n} |g_m|^2 |g_n|^2} \tag{4.7}$$

If there were no interference, then this method would return the true value of the source strength at the true source location. One consequence of the best-fit method however, is that the process will also return non-zero values for the source strength at locations adjacent to the true source location. This gives rise to the concept of the point spread function (PSF), which characterises the extent to which the beamforming algorithm spreads the true source strength around the nearby scanning grid points. It is the extent of this PSF that determines the array's ability to resolve a given source location.
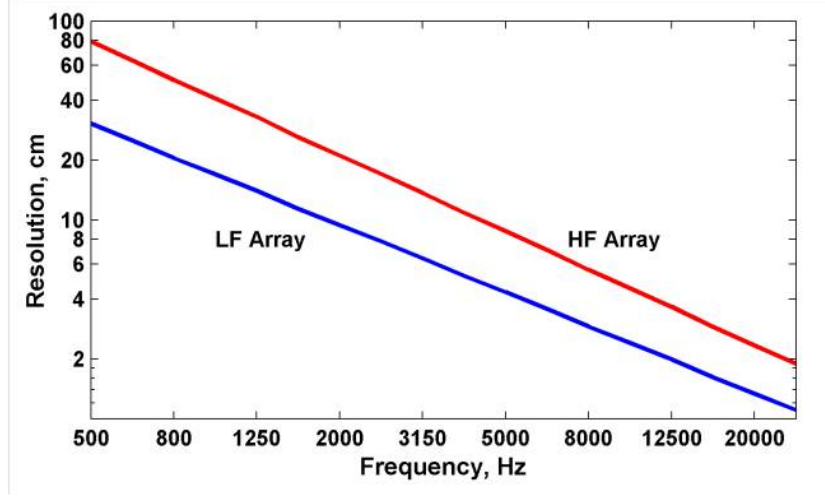
Figure 4.6: Plot showing the resolution of the Markham arrays as a function of source frequency (Quayle [2008])

4.2.4 Sidelobes and Resolution

A unit source at the scanning grid point $\underline{\xi}_j$ produces the CSM given by equation 4.8:

$$C_{jj} = \frac{1}{2}\underline{g}_j\underline{g}_j^*$$ (4.8)

Since the beamforming process described above is imperfect, it gives a source strength at point k due to the source at another grid point j:

$$A_{jk} = \underline{\omega}_k^* C_{jj} \underline{\omega}_k$$ (4.9)

$$\underline{\omega} = \frac{\underline{g}}{\sum_{m,n}|g_m|^2|g_n|^2}$$ (4.10)

If the true source is located at $\underline{\xi}_k = \underline{\xi}_j$ then at that location $A_{jj} = 1$. For all points $\underline{\xi}_k \neq \underline{\xi}_j$, the true source strength is 0 but the beamforming algorithm returns positive values at some of these locations, including those immediately adjacent to the estimated source. The resolution of the array is thus normally defined as the region where A_{jk} is within 3dB of the peak source strength.

The resolution of the arrays in the Markham wind tunnel was investigated during their initial installation and calibration by Shin et al. [2007]. The resulting array resolutions are shown in figure 4.6.

The beamforming algorithm returns other non-zero values at locations around the scanning grid. These other false solutions are known as sidelobes and their
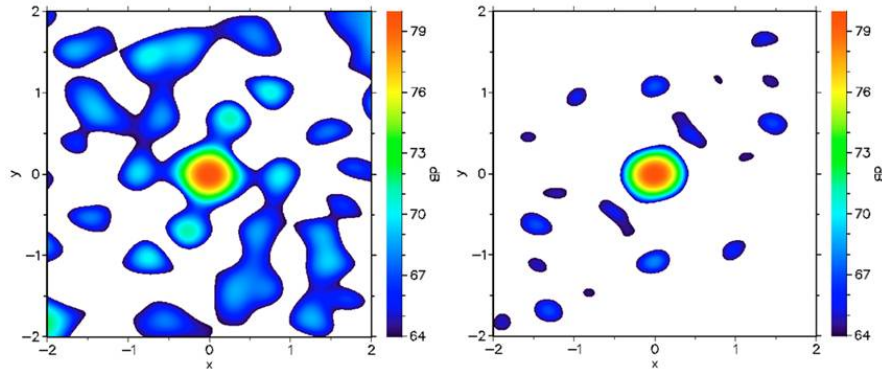
Figure 4.7: Source plots from an array with randomly located microphones (left) and with optimised microphone locations (right) [van der Wal and Sijtsma, 2001]

strength and location will depend on the location and frequency of the source. The location of the microphones is a key determinant of the strength and location of the sidelobes. This effect is demonstrated in the plot from van der Wal and Sijtsma [2001] that shows the difference in source plots for an array with randomly located microphones and an optimised microphone configuration (figure 4.7).

4.2.5 Removal of Microphone Autopowers

The diagonal components of the CSM are know as the 'autopowers'. There are two circumstances in which the autopowers can dominate the CSM and have a negative impact on the performance of the beamforming algorithm. These are when the microphone signals are influenced by boundary layer pressure fluctuation and when the sound propagation is distorted by turbulence, causing a loss of coherence.

In a closed section wind tunnel like the Markham tunnel, where the microphones are flush mounted in the tunnel walls, the pressure fluctuations in the boundary layer are often greater than the acoustic pressure signal from the source. The boundary layer fluctuations are random in nature and therefore the signal is only weakly coherent between microphones. The boundary layer pressure signal therefore only appears in the autopowers and has little impact on the cross-powers, provided enough averages are taken to eliminate random noise.

When sound propagates through a turbulent flow the paths from the source to the microphones will be distorted. This can result in a loss of coherence between the microphone signals. Since the autopowers do not contain any phase information they are not affected by coherence loss and so come to dominate the CSM. Coherence loss is particularly significant in open jet wind tunnels where there is

an intensely turbulent shear layer between the source and the microphones. If sufficiently many averages are taken the noisy distortion introduced by turbulence can be reduced in the cross-powers.

The microphone autopowers lie on the diagonal of the CSM and by simply setting their value to zero the performance of the beamforming algorithm can be significantly improved for the two cases described above. An alternative method for removing the noise on the diagonal component of the CSM was investigated, which avoided completely removing the diagonal components. A property of the CSM is that it has to be positive semi-definite. This allowed the convex optimisation methods developed by Boyd and Vandenberghe [2004] to be implemented to attempt to determine the noise components.

Assuming that the noise lies exclusively on the diagonal of the CSM allows it to written as the sum of a noise free CSM, R_0, and a diagonal matrix containing the noise signal, D:

$$C_0 = R_0 + D; \qquad (4.11)$$

The convex optimisation routine then minimises the sum of the diagonal components of D, subject to the condition that R_0 is positive semi-definite. With the help of Prof. Keith Glover this method was implemented in Matlab using the CVX package developed by Boyd and Vandenberghe [2004]. A 'noise free' CSM was generated by this method and the beamforming algorithm was run on the output. A comparison of the beamforming plots for the cases with no noise removal, the diagonal removal method and the CVX method is presented in figure 4.8. The beamforming tests were conducted on a 2mm diameter cylinder in a flow of 20m/s, since this gave a known source location indicated by the vertical line. The plots shown are for the 1/3rd octave band with a centre frequency of 5000Hz and the microphone data were sampled for 2mins at 120kHz using the high frequency array. The cross-spectral matrices were calculated using a blocksize of 1024 with a 50% overlap and a Hanning window giving over 42,000 averages.

The CVX method clearly works well and produces beamforming output that is as good, if not slightly better, than that produced by just setting the autopowers to zero. The issue with this method is the time taken to carry out the convex optimisation calculation to remove the noise on the diagonal of the CSM. To process all of the CSMs required to produce the single plot shown above took 20secs. For a general investigation of the beamforming output, where it is necessary to look at multiple cases and multiple frequencies, this method adds a significant amount of time to the processing without yielding any significant improvement in the output.

(a) No noise removal   (b) Removal of diagonal   (c) CVX noise removal
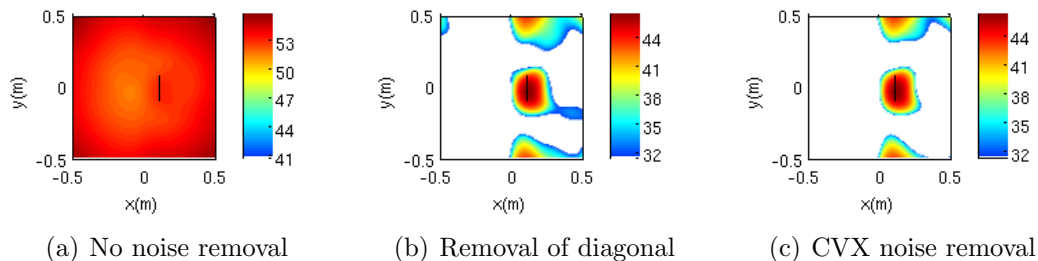
Figure 4.8: Comparison of the basic beamforming output with the results of the two different noise removal methods for the noise radiated by a 2mm diameter cylinder in a free stream of 20m/s.

4.2.6 Tunnel Background Noise

For his study of landing gear noise, conducted in the Markham wind tunnel, Quayle [2008] developed a method for subtracting the background noise from the microphone cross-spectra. The method involved recording the microphone signals with an empty tunnel and computing the CSM before subtracting it from the signals measured with the model installed. For the VAWT model, background noise measurements were made at each tunnel speed corresponding to the different rotor TSR. In addition, these measurements were made with the motor running (without the rotor attched) at the speed required to achieve each TSR, as there was a concern that the microphones could be directly recording the sound from the motor rather than the aerodynamic noise from the model.

Comparison of the cross-spectra with the tunnel empty and with the rotor installed found that the background noise was much less than the noise from the model (see figure 4.9). Even for the TSR=1 case, where the tunnel speed was highest, the background noise was well below the signal from the rotor, particularly in the frequency range that was of interest for beamforming (1kHz-3kHz). The routine for subtracting the background noise was tested and was found to make no discernible difference to the output.

4.2.7 Dipole Beamforming

A dipole can be represented as two monopole sources separated by a small distance δl, and 180° out of phase with each other. The amplitude of a dipole can therefore be written as the sum of two monopoles (See Eqn.4.2).

71

(a) TSR=1: $U_\infty = 14.8$m/s, $\Omega_{rotor} = 535$rpm

(b) TSR=3: $U_\infty = 6.6$m/s, $\Omega_{rotor} = 718$rpm
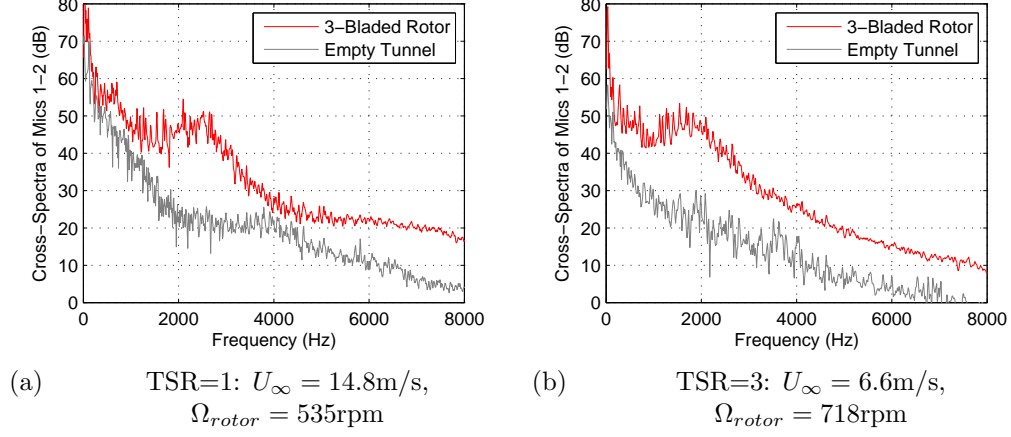
Figure 4.9: Comparison of spectra from the model VAWT rotor and for the empty tunnel with both the tunnel fan and the motor that drives the model running.

$$\hat{p}(\underline{x}, t) = \left(\frac{ae^{-i\omega\Delta t_e}}{4\pi\alpha} \right)_{\underline{\xi}+\underline{\delta l}} - \left(\frac{ae^{-i\omega\Delta t_e}}{4\pi\alpha} \right)_{\underline{\xi}}$$

$$= -\underline{\delta l} \cdot \nabla \left(\frac{ae^{-i\omega\Delta t_e}}{4\pi\alpha} \right)_{\underline{\xi}} \qquad (4.12)$$

where α and Δt_e are as defined in equation 4.4 and equation 4.5.

The minus sign on the right of equation 4.12 arises due to the fact that the gradient function ∇ operates on $\underline{x}$ rather than $\underline{\xi}$. Expanding the bracket in the expression above gives,

$$\hat{p}(\underline{x}, t) = \frac{a\delta l}{4\pi} \cdot \left[\frac{i\omega\nabla(\Delta t_e)}{\alpha} e^{-i\omega(\Delta t_e)} + \frac{e^{-i\omega\Delta(t_e)}}{\alpha^2} \nabla\alpha \right] \qquad (4.13)$$

In the above expression α is the distance term, hence the term on the left is the far-field term and the term on the right is the near-field term due to the $1/\alpha^2$ dependence. The acoustic far field is defined as the region where $f\alpha/c_0 \gg 1$. For a model that is at a minimum distance of 0.35m from the array plane then the source can only be considered as being in the far-field if the source frequency $f \gg 950$Hz.

The gradient terms in equation 4.13 can be written as:

$$\underline{\nabla}(\Delta(t_e)) = \frac{-\underline{M} + \underline{\nabla}\alpha}{c\beta^2}$$

$$\underline{\nabla}\alpha = \frac{(\underline{M} \cdot \underline{r})\underline{M} + \beta^2\underline{r}}{\alpha}$$

where $\beta^2 = 1 - |M|^2$.

It is theoretically possible to determine both the dipole amplitude a and the direction $\underline{\delta l}$ at every point in the scanning grid. This would however, require a great deal of iteration, and would hence take a very long time to reach a solution. The array would also struggle to identify dipoles whose axes were parallel to the array plane, particularly if the signal to noise ratio was low [Quayle, 2008].

In most cases the orientation of a dipole source being investigated is known in advance. This piece of information can therefore be used in the beamforming process, making it a simple adaptation of the monopole case. This is the approach that was implemented by Sijtsma in the beamforming software used for this research.

For the case of the model VAWT the dipole direction is known to be perpendicular to the blade chord, but this direction is constantly varying. It was therefore not sensible to select a single dipole direction as this could result in misleading results. While the monopole model is not a true representation of the source it was, therefore, still the better option for investigating the time-averaged sound from the VAWT.

4.3 Beamforming Limitations

Beamforming has a number of limitations for location of the noise sources on the model VAWT and it is worth attempting to quantify these uncertainties before examining the output plots. One major limitation is the low resolution below 1kHz, which prevents the harmonic sources identified in the spectral analysis from being located. As such the beamforming analysis focusses on the higher frequency components of the spectra.

4.3.1 Doppler Effects

When the source is moving relative to the array the impact of Doppler amplification needs to be accounted for. The amplification of a sound due to relative motion of the source and observer is given by the term $(1 - M_r)^{-1}$ (see Dowling and Ffowcs Williams [1983], eqn.9.7). One half of the VAWT rotor will be travelling towards the array and one half will be travelling away, which means that

73

the change in amplitude of the cross-spectral power due to Doppler effects can be expressed as,

$$\text{Doppler Amplification (dB)} = 10 \log \left(\frac{(1 + M_B)^2}{(1 - M_B)^2} \right) \qquad (4.14)$$

where M_B is the absolute blade Mach number. The highest blade Mach number in these experiments was 0.07 which gives a maximum relative Doppler amplification of 1.2dB between the upstream and downstream halves of the rotor.

4.3.2 Model Depth Issues

The array is designed to estimate the angle of arrival of a sound and has very limited ability to determine the distance of a source from the array plane. If the source lies within a fixed plane then the placement of the scanning grid can eliminate this problem since the distance from the source to the array is known. In the case of the model VAWT however, the source has significant depth in the direction perpendicular to the array. The maximum depth of the model is 0.53m (i.e. the rotor diameter), and its axis was located 0.60m from the array, meaning that the assumed source location in a horizontal scanning plane could be significantly in error.

In order to understand the effect of this on the beamforming output an estimate of the potential error due to depth effects was calculated. A series of cases was simulated, with a point monopole source placed at different distances from the centre of the array to represent the possible range of depths that a source from the model VAWT could come from. The beamforming algorithm was then run with the scanning grid assumed to be fixed at the rotor hub height. The results from these simulations are presented in figure 4.10.

It is evident from these plots that if the source is located away from the scanning grid that the beamforming algorithm can potentially produce misleading results, particularly if the source is close to the array. To assess the impact of this problem on the experimental data the beamforming algorithm was run on a test case with the scanning grid placed at a range of heights from the lowest to the highest point of the VAWT's rotation. This test showed that the location of the scanning grid did affect the source location estimated by the beamforming algorithm. Critically however, the trends in the *relative* source location between the various cases tested was not significantly affected. As such, the beamforming plots obtained by placing the scanning grid at the hub were sufficient for most of the analysis undertaken.
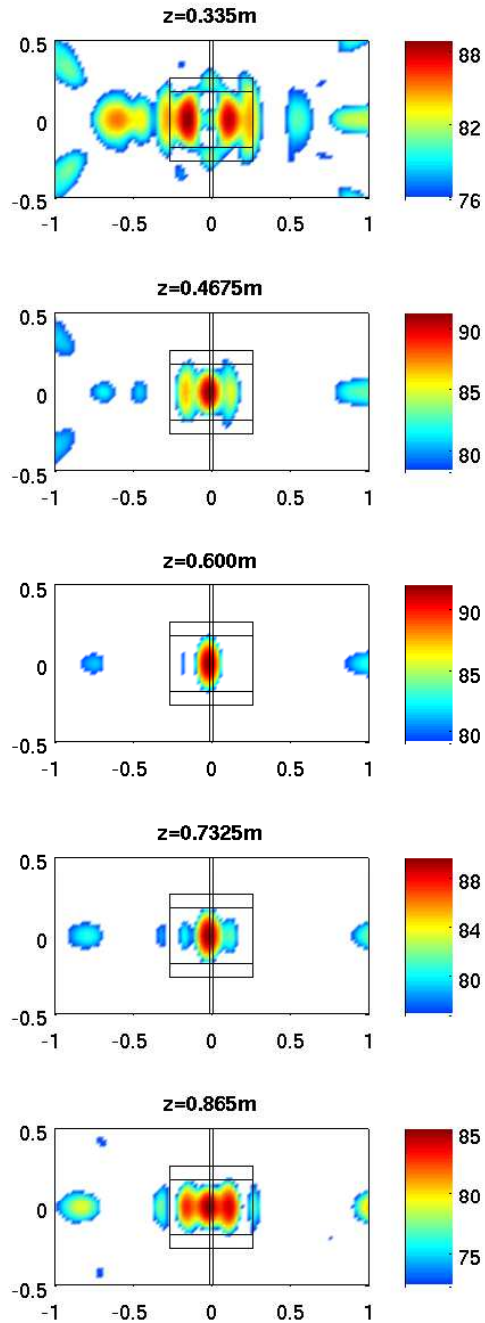
Figure 4.10: Plots showing the different beamforming outputs at $f_{1/3}$=1600Hz with a simulated point monopole source in the centre of the scanning grid at the height indicated above each plot. The scanning grid height is 0.6m in all cases.

4.3.3   Moving Sources

Aside from Doppler effects the fact that the source is moving has other impacts on the output generated by the beamforming algorithm. The averaging carried out when converting to the frequency domain necessarily means that only the loudest sources on each rotation will be visible in the beamforming plots. While the loudest sources are of the most interest in terms of noise reduction, this does prevent detailed examination of the sources at different blade azimuthal angles.

4.3.4   Tunnel Reverberation

The Markham wind tunnel, used in these experiments, is a closed section tunnel and therefore the issue of tunnel reverberation might be expected affect the results. Previous measurements using the acoustic array in this tunnel found however, that this issue did not have any significant impact on the results [Quayle, 2008; Shin et al., 2007]. It was therefore not deemed to be necessary to consider any effects of reverberation in this study.

4.4   Beamforming Extensions

In order to attempt to account for some of the beamforming limitations described above, two extensions to the existing beamforming approach were developed. To limit the problem of model depth a curved scanning grid was generated, and to cope with the unsteadiness of the moving sources individual sectors of the rotation were separated out and individually processed. The details of these two methods are outlined below.

4.4.1   Curved Scanning Grid

When the sources were located at the closest point of the blades' trajectory it was found that the beamforming algorithm struggled to accurately locate them if a flat scanning grid was used. An alternate scanning grid was generated that was flat upstream and downstream of the rotor, but followed the curve of the lower half of the rotor, as shown in figure 4.11(e). For the simulated monopoles in section 4.3.2 this approach was found to greatly improve the ability of the array to locate sources at the position closest to the array (see figure 4.11).

The results from some of the experiments were processed using this grid in order to evaluate the performance of the conventional flat grid to help ensure that sources were correctly identified (see figures 4.11(c) and 4.11(d)). The curved scanning grid clearly gave slightly different estimates of the source strength and location relative to the flat grid. As with the choice of scanning grid height

however, the trends in the location of the sources between the various cases tested was the same for both scanning grids. To avoid preferentially locating sources on the lower half of the rotor the flat scanning grid was therefore used, unless otherwise stated.

4.4.2 Sector Beamforming

As discussed above, the fact that the VAWT blades are moving and the depth of the model perpendicular to the array make beamforming difficult. Algorithms have been developed, such as the rotating source algorithm ROSI [Sijtsma et al., 2001], that operate in the time domain and allow moving sources to be resolved. This has been shown to work well for cases such as a helicopter in hover or HAWT blades, where the flow over the blades is steady. For the case of the VAWT however, where the blade aerodynamics are a function of both time and space, this algorithm would still only yield a time averaged source image.

The solution implemented in this study was to divide the rotation into a number of small sectors and then separately beamform the sound radiated from each. This division into sectors was possible due to the synchronised sampling method which allowed a fixed number of evenly spaced data points to be recorded for every revolution of the rotor. The process for beamforming individual sectors is outlined below:

1. The original sampling rate was 2048 samples per revolution so blocks of 128 were split out from each microphone channel and then reassembled into 16 separate data sets. One important consideration in choosing the number of sectors to resolve was the propagation time from each sector to the most distant microphones. In order to avoid having to account for this propagation time in the data processing it had to be less than the time taken for the rotor to pass through each sector. With the number of sectors set to 16 the maximum propagation time was approximately half of the duration of each sector, which was found to be sufficient to resolve the sources.

2. The number of sectors of interest N_{sec}, was equal to $16/B$ where B was the number of blades. For the three bladed rotor this was not an integer, but was rounded up to 6 to include one complete period. The first N_{sec} sectors were then carried into the next processing stage.

3. The cross-spectra for each microphone pair were then computed and the cross-spectral matrix (CSM) was generated for each frequency line up to 5000Hz, which was the upper limit for beamforming with the low frequency array. The FFTs were computed with no overlap since the signals were not continuous and a Hanning window was used to avoid any discontinuities

(a) Simulated monopole 335mm from array, flat grid at 600mm

(b) Simulated monopole 335mm from array, curved grid

(c) 3-bladed rotor at TSR=2, flat grid through hub

(d) 3-bladed rotor at TSR=2, curved grid
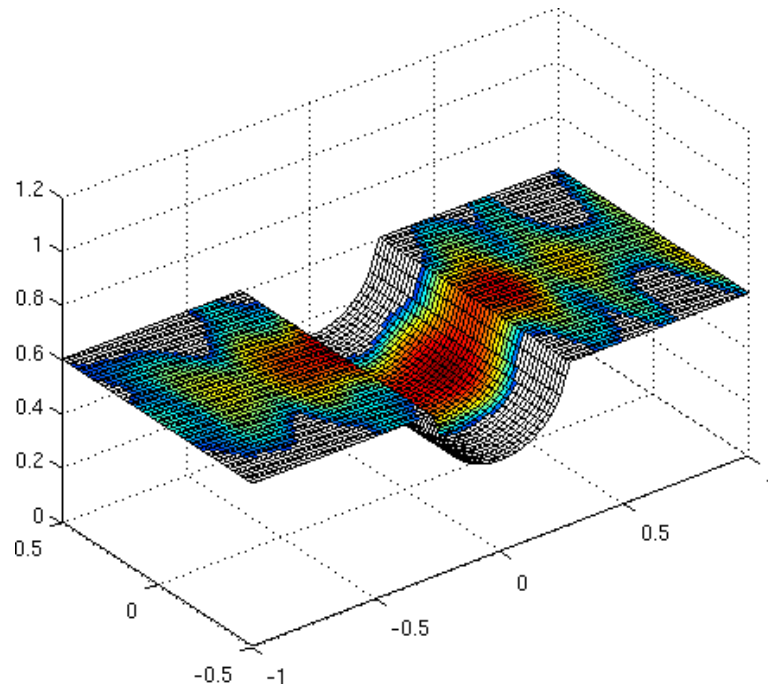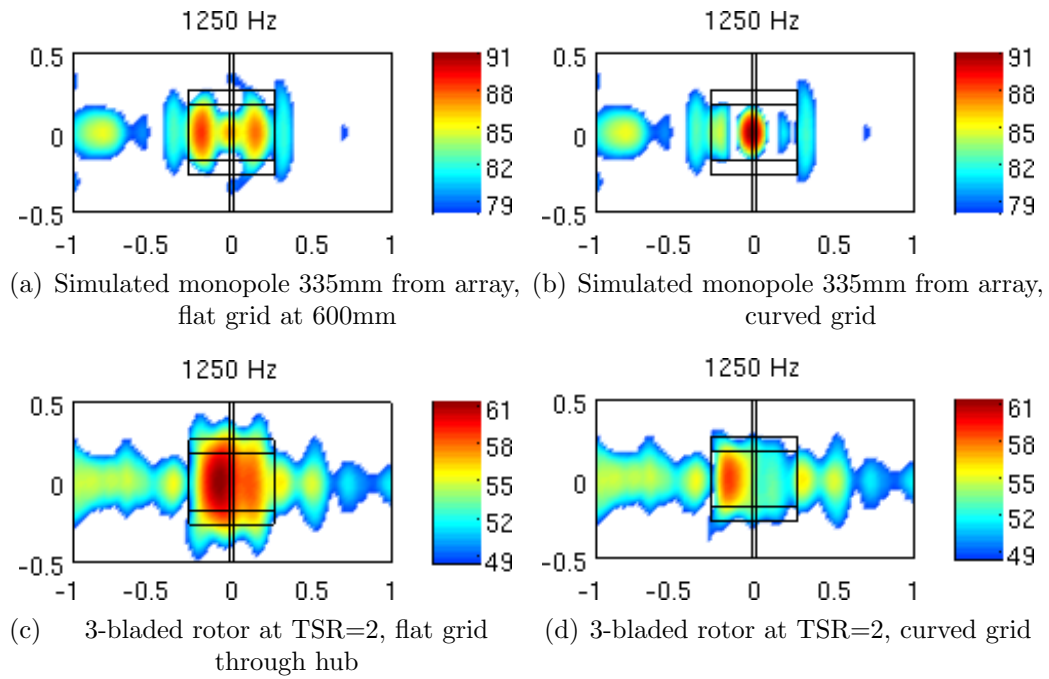
(e) Example of curved scanning grid

Figure 4.11: (a) and (b) show beamforming plots of simulated monopole source 335mm from the array for a flat and a curved scanning grid. (c) and (d) show the effect of using a curved scanning grid on an experimental test case (3-bladed rotor at TSR=2) and (e) shows the configuration of the curved scanning grid.

between consecutive blocks. In this calculation the microphone density correction was included, but not the effective aperture correction (see Sijtsma [2004b, p.23]). This correction term only scales the amplitude of the cross-spectra and does not change the relative phase of the microphone signals so was not expected to dramatically effect the ability of the array to locate the sources. This was confirmed by a direct comparison between the full method and the sector method with the number of sectors set to 1, which produced a nearly identical source map but with slightly increased amplitudes.

For the sectors where the blades were at either the upstream or downstream location the beamforming algorithm struggled to locate the sources. The sources on the blades were expected to be dipole in nature, hence, when the blades were at these locations, a proportion of the microphones was expected to be 180° out of phase of the rest. To test this, dipole beamforming was used with the dipole orientation set perpendicular to the mean location of the blade chord. This was found to slightly improve the algorithm's ability to locate the sources in some cases, although it was only really applicable to the 2-bladed rotor where the dipole on both blades had the same orientation.

The curved scanning grid described above was used in the sector beamforming process and was found to slightly improve the location of the sources, particularly for the sectors where the blades were closest to the array. The impact of using the curved grid in the sector beamforming process is illustrated in figure 4.12. With the flat scanning grid the main source is relatively well located, but the curved scanning grid also allows the quieter, upstream blade to be identified.

4.5 Spectral Processing Methods

The cross-power spectra of a pair of microphones represents the component of the sound spectrum that is coherent between the two microphones. If two closely spaced microphones are chosen in the computation of the cross spectra then the result is a reasonable approximation of the autopower spectrum radiated to that region. The spectra are a useful tool for investigating the sound field in conjunction with the beamforming algorithms. A number of the aeroacoustic prediction models, such as the empirical approach of Brooks et al. [1989] and the trailing edge noise model of Amiet [1976], generate estimates of the power spectral density. Comparisons of the predictions from this type of model with the measured spectra can potentially yield useful information about the noise sources.

A further benefit of examining the spectra is that it gives a clear indication of which frequencies radiate the loudest noise. This can help to direct the inves-

(a)

(b) Flat scanning grid   (c) Curved scanning grid
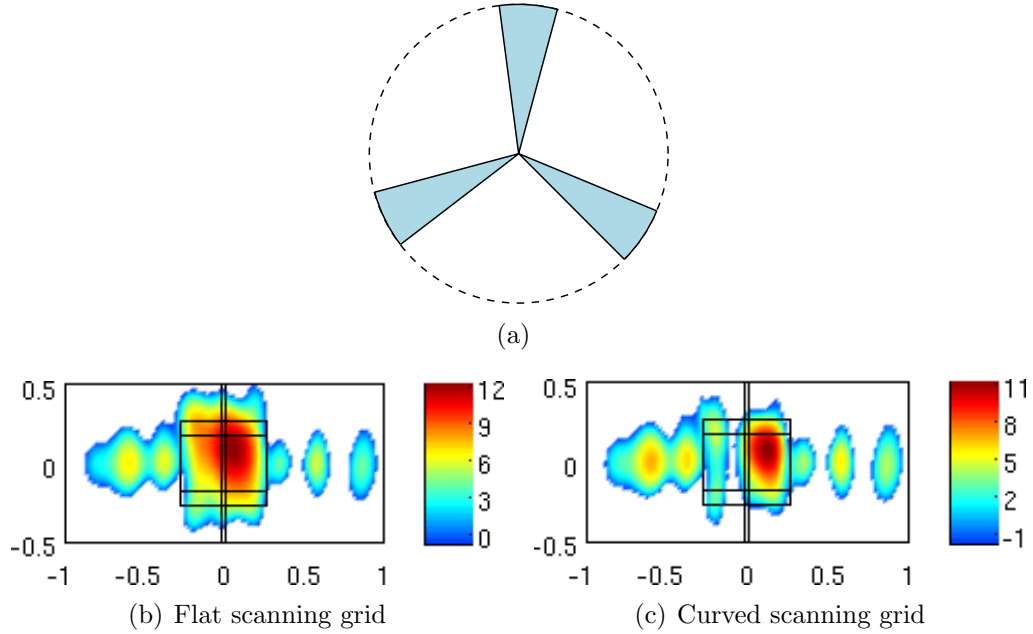
Figure 4.12: Impact of using curved scanning grid for sector beamforming

tigation carried out with the beamforming algorithms as it can focus the process on the dominant frequency bands. Comparison of the spectra between different cases could also highlight the regions of the spectra where there are changes in the radiated sound. Again this can help to direct the beamforming investigations to the most interesting components of the sound sources.

4.5.1   Trailing Edge Noise Scaling

As previously mentioned, the sound radiated by scattering of pressure fluctuations passing over a sharp edge scales with the fifth power of the Mach number [Ffowcs Williams and Hall, 1970]. By examining the amplitude of the spectra radiated by the VAWT rotor at different operating conditions it may be possible to identify whether the relative amplitude is consistent with this M^5 scaling.

For the experimental cases carried out at a constant relative blade velocity any component of the spectra that was not influenced by a change in TSR could have been radiated from the trailing edge of the blades. For the constant TSR cases, where the relative blade velocity was changing, the amplitude of the spectra would be expected to scale in proportion to the fifth power of the ratio of the velocities. On a decibel scale the change in amplitude of the cross-spectra would then be given by an addition of $20 \log_{10}(U_2/U_1)^5$ where U_1 and U_2 are the two velocities in question. For example, an increase in wind speed of 6m/s to 7m/s

gives an increase of 6.7dB.

This relationship is embodied in the scaling laws of Brooks et al Brooks et al. [1989], where trailing edge noise spectra were normalised with respect to the Mach number variation using the formula of equation 4.15, in which δ_p is the pressure surface boundary layer thickness, L is the blade span and r_e is the distance from the source emission location to the observer.

$$SPL_{1/3,Scaled} = SPL_{1/3} + 10\log_{10}\Big(M^5\frac{\delta_p L}{r_e^2}\Big) \qquad (4.15)$$

4.5.2 Laminar Boundary Layer Noise Scaling

In light of the chord-based Reynolds numbers of both the full-scale and model-scale VAWT rotors, there was a possibility that laminar boundary layer tonal noise could be radiated. Preliminary investigations of the spectra from the model-scale VAWT indicated that there was a broadband peak that could have been generated by this mechanism, so spectral scaling methods were investigated to determine whether this source was from laminar boundary layer effects. In their paper on airfoil self-noise Brooks et al. [1989] developed a method for scaling the spectra radiated by laminar boundary layer vortex shedding (LBL-VS). Parts of this methodology were implemented in the present study to ascertain whether any of the stochastic features of the spectra could be due to LBL-VS. Due to the fact that the blade angle of attack and relative blade velocity were constantly changing a number of assumptions had to be made in the scaling process and these are outlined below.

The frequencies were first converted to Strouhal numbers using twice the laminar boundary layer thickness, $2\delta_p$, as the relevant length scale. Following the method originally described by Paterson et al. [1973], δ_p was estimated from the Blasius solution for flat-plate, laminar boundary layers given in equation 4.16, where c is the blade chord.

$$\delta_p = \frac{5c}{(Re_c)^{1/2}} \qquad (4.16)$$

Inserting this expression into the equation for the Strouhal number results in a factor of $U_{rel}^{3/2}$ as shown in equation 4.17 where f is the frequency, ν is the kinematic viscosity and U_{rel} is the relative velocity of the blade.

$$Str = \frac{10f(c\nu)^{1/2}}{U_{rel}^{3/2}} \qquad (4.17)$$

The expression determined by Brooks et al. [1989] for predicting LBL-VS noise is given below in equation 4.18, where $\bar{D}_h$ is a directivity function and α is the

angle of attack. In this equation the function $G1$ gives the shape of the LBL-VS spectra and the other terms scale the amplitude of this curve to account for the influence of blade Mach number, Reynolds number and angle of attack.

$$SPL_{1/3,LBL-VS} = 10\log_{10}\Big(\frac{M^5\delta_p L\bar{D}_h}{r_e^2}\Big) + G1\Big(\frac{St'}{St'_{peak}}\Big) + G2\Big(\frac{Re_c}{(Re_c)_0}\Big) + G3(\alpha)$$

$$(4.18)$$

For the experiments where the TSR was held constant while the tunnel speed was varied, the blade angles of attack should have been the same for all cases so the function $G3$ could be ignored. The scaling process therefore involved subtracting the first term of equation 4.18 and the function $G2$ from the measured spectra as follows:

$$SPL_{1/3,Scaled} = SPL_{1/3,Measured} - 10\log_{10}\Big(\frac{M^5\delta_p L\bar{D}_h}{r_e^2}\Big) - G2\Big(\frac{Re_c}{(Re_c)_0}\Big) \quad (4.19)$$

If the measured spectra were due to LBL-VS then this scaling process would cause the spectra to collapse on to a single curve with the shape given by function $G1$. For calculating the blade Mach numbers and Reynolds numbers a representative blade velocity needed to be chosen. Preliminary beamforming results suggested that, for the frequency range where LBL-VS was expected, the sound was being radiated as the blades travelled upstream. As such the blade velocities used in the scaling process were (TSR+1) times the free stream velocity. In the function $G2$ the reference Reynolds number $(Re_c)_0$ is a function of angle of attack so, since $\alpha \simeq 0$ as the blades travel upstream, this value was used for calculating $(Re_c)_0$.

4.5.3 Sensitivity to Scaling Parameters

An investigation of the sensitivity of the scaling process to the input parameters showed that the scaling is strongly dependent on the inputs used, especially the angle of attack. This sensitivity is entirely due to the shape of the function $G2$, which determines the relative amplitudes of the LBL-VS peaks as a function of Reynolds number and angle of attack.

The value of the scaling function $G2$ was calculated for the constant TSR=3 cases at a range of different values of angle of attack and Reynolds number. The results are plotted in figure 4.13, superimposed on the complete $G2$ function. It is clear from these two plots that the function is much more sensitive to angle of attack than it is to Reynolds number. A one degree change in the angle of attack used in calculating $(Re_c)_0$ caused the four cases to be shifted from the relatively

(a) Constant $U_{rel} = 4 \times U_\infty$ (b) Constant $\alpha = 0 \deg$
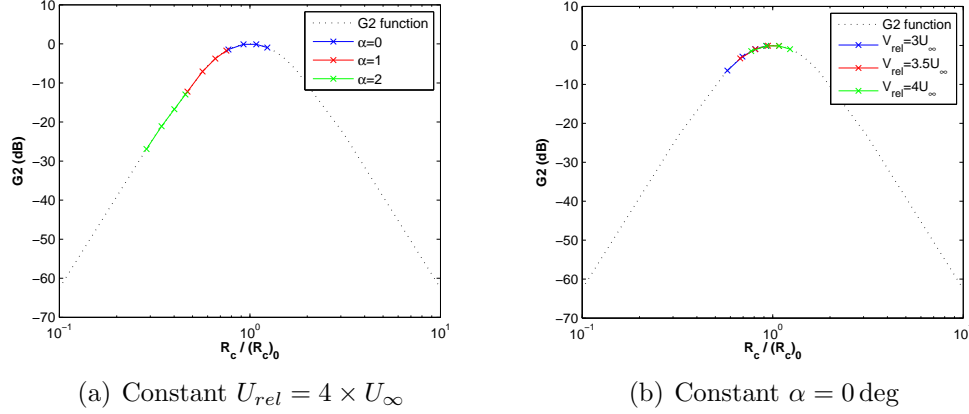
Figure 4.13: Values of $G2$ for the four constant TSR=3 cases with a range of Reynolds numbers and angles of attack.

flat peak of the curve on to the steeper section of the curve resulting in completely different relative scaling of the four cases. Changing the relative blade velocity from $3U_\infty$ to $4U_\infty$ however, had only a small impact on the location of the four cases on the $G2$ curve.

Assuming that the scaling function is accurate, the fact that the output is sensitive to the angle of attack means that it should be possible to determine the angle of attack at which the laminar tonal noise is generated. Since the angle of attack is a function of blade azimuth, this theoretically means that the blade location where the tonal noise is radiated can be estimated.

4.5.4 A-Weighting

Preliminary investigations of the cross-spectra indicated that there was a strong low frequency component. The human ear is less sensitive at these low frequencies so a weighting function is often used to account for this. The most commonly used weighting function is A-weighting which is defined by equation 4.21.

$$R_A(f) = \frac{12200^2 f^4}{(f^2 + 20.6^2)(f^2 + 12200^2)\sqrt{(f^2 + 107.7^2)(f^2 + 737.9^2)}} \tag{4.20}$$

$$A(f) = 2.0 + 20 \log_{10}(R_A(f)) \tag{4.21}$$

Care needs to be taken when using A-weighting on the experimental data however, since the frequencies radiated will have been altered by the scaling of the model. For the laminar boundary layer noise the Strouhal number scales
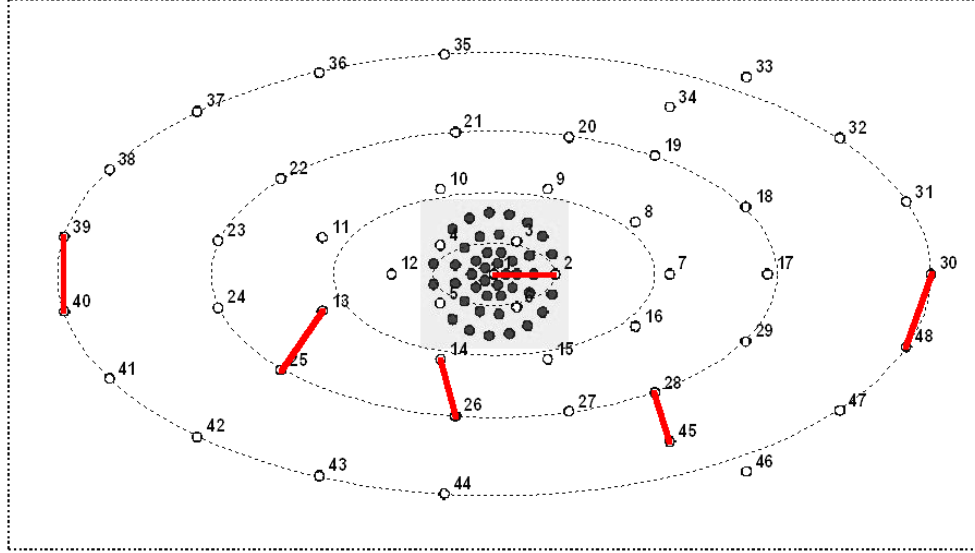
Figure 4.14: Layout of low-frequency array microphones with the pairs used for calculation of the total sound power linked by red lines.

with the pressure surface boundary layer thickness, which is assumed to be proportional to the square root of the blade chord. The frequencies on the model rotor will therefore have been shifted to higher frequencies by a factor of $(c_{Full-scale}/c_{Model})^{1/2} = 1.8$. The trailing edge noise frequencies are also assumed to scale with boundary layer thickness so will be shifted by approximately the same factor. These scaling issues make it inappropriate to apply A-weighting to the model-scale noise measurements.

4.5.5 Average Sound Pressure Level

The spectra give some indications about the origins of the sound, but do not necessarily demonstrate any trend in total noise radiation. The frequency-summed, total cross powers were therefore calculated in the following steps:

1. Convert the spectra from dB to a linear scale
   $P_{lin}(f) = 10^{P_{dB}(f)/10} P_{ref}^2$

2. Sum the pressures, scaling the output by the frequency resolution, Δf
   $P_{tot} = \sum_j P_{lin}(j)\Delta f$

3. Convert the total pressure back to decibels
   $P_{tot,dB} = 10\log(\frac{P_{tot}}{4e^{-10}})$

In order to account for potential directivity effects, an average of several microphone cross-spectra was used to estimate the average sound pressure level. Since the sound field was expected to be symmetrical about the blade mid-span, six pairs of microphones were chosen in one half of the array (see figure 4.14). Closely spaced pairs of microphones were chosen to achieve the best approximation of the autopower. The clockwise rotation case is equivalent to the anticlockwise case but with the microphones mounted on the roof, rather than the floor of the tunnel. As such the data for these two cases could also be averaged to obtain the best possible estimate of the total radiated sound power.

4.6 Experimental Program

Based on the previous studies of VAWT aerodynamics and noise generation a number of parameters were identified for investigation in the experimental program. They were TSR, rotor solidity, shaft diameter and inflow turbulence. The ways in which these parameters were tested are outlined below.

4.6.1 Tip Speed Ratio

The TSR is a key parameter in determining the performance of a VAWT. It was shown in section 3.1.1 that the TSR has a significant effect on the blade angles of attack and hence on the blade loads. Since the blade loading fluctuations were thought to be a potentially strong noise source, the variation in sound radiation with TSR was of great interest.

In the wind tunnel experiments there were a number of ways in which a range of TSRs could be acheived. These options are listed below along with their potential advantages and disadvantages.

1. **Constant tunnel speed** - With the tunnel speed constant the rotor speed could be varied to achieve the desired TSR. The advantage of this method is that it allows a direct comparison of the different noise levels at each TSR for a given wind speed. This is potentially useful in determining the optimum TSR for noise minimisation. The disadvantage is that, in order to reach TSR=5 without exceeding the maximum rotor angular velocity, the tunnel speed would have to be very low. One problem with this approach is that at the lower TSRs the rotor angular velocity and hence blade speed will be low meaning that the noise radiated may be hard to detect above the background noise. The tunnel speed is also difficult to accurately control at such low velocities meaning that it is hard to accurately fix the TSR.

2. **Constant rotor speed** - With a fixed rotor angular velocity the tunnel speed could be varied to achieve the desired TSR. The advantage of this method is that it maximises the rotor speed and hence the frequency of the radiated sound, thereby giving the highest possible spatial resolution in the beamforming plots. This method will give much higher relative blade velocities for the low TSR cases, which results in the blades radiating much more sound. This may however, make it difficult to isolate the changes in the sound field that are due to the aerodynamic changes with TSR from the change in the sound field due to the increased blade velocity.

3. **Constant maximum relative velocity** - The relative blade velocity at a reference point in the rotation could be fixed, which requires both the rotational velocity of the rotor and the tunnel speed to be varied to achieve the desired TSR. The advantage of this method is that it allows a more direct comparison between the noise generation mechanisms at each TSR since the impact of changing blade velocity is removed. In this case the only differences between the sound fields at each TSR are due to the changes in angle of attack and induction factor. The method therefore largely eliminates differences in sound generation due to changes in the Reynolds number of the flow over the blades.

The third method was chosen for most of the experiments since it permitted the best comparison between the different noise source mechanisms at each TSR. The tunnel speed and rotor speed for each TSR were calculated assuming a fixed relative blade velocity at the most upstream point in the rotation, where the blade velocity and free stream velocity are perpendicular. The relative velocity chosen was governed by the maximum rotational speed at which the rotor could safely be operated. For the initial experiments with the 3-bladed rotor this maximum speed was 900rpm, while for the later experiments with different rotors it was limited to 770rpm due to vibration problems. In order to make comparisons across all cases a limit on the rotational speed of 770rpm was imposed. This gave a maximum relative blade velocity of 21m/s for which the tunnel and rotational speeds are given in table 4.2.

4.6.2 Rotor Solidity

The rotor solidity is a key parameter in the design of a VAWT since it has an impact on the rotor induction factor, and hence the global rotor aerodynamics. The rotor solidity could be varied in a number of ways. One could either change the blade chord, change the spoke length or change the number of blades (or any combination of these).

TSR	$U_\infty(m/s)$	$\Omega(rpm)$
1	14.8	535
2	9.4	677
3	6.6	718
4	5.1	734
5	4.1	742
No Wind	0.0	757

Table 4.2: Tunnel and rotor speeds used

Since the blades used for the wind tunnel model were an 'off-the-shelf' component their chord could not be easily changed without further major alterations to the rotor. The spoke length was also constrained by the wind tunnel dimensions. The spokes could not be made any longer without increasing the tunnel blockage to an unacceptably high level. At the same time their length could not easily be reduced due to the maximum rotational speed that could safely be achieved. It was therefore decided that the best option was to change the number of blades on the rotor.

A further rotor model was therefore manufactured with four spoke attachment points on the hub, all at 90deg to each other. This allowed both a 2-bladed and a 4-bladed rotor configuration to be tested. The construction of the additional blade was identical to the 3-bladed rotor so that the same blades could be used in all three models. One consideration that had to be made was the increase in the mass of the rotor due to the addition of a fourth blade. This increased mass reduced the natural frequency of the shaft, which was why the upper limit on the rotational velocity of the rotor had to be reduced from 900rpm to 770rpm.

The 2-bladed rotor also posed certain problems since, with the blades at 180° to each other, the aerodynamic loads create significant structural vibration. This problem was very evident in the experimental tests and, while it was possible to make virtually all the measurements desired, great care had to be taken to ensure the rotor was not damaged. It was particularly important to reduce the tunnel speed before increasing the rotor speed, otherwise the rotor could easily be driven into a state of extreme vibration.

4.6.3 Shaft Diameter

The work of Castelli et al. [2012] indicated that the interaction between the downstream rotor blades with the wake from the shaft could produce a significant amount of noise. In order to investigate whether this effect was significant or not the wind tunnel model was fitted with a large diameter tube over the main shaft.

Grid	Mesh Size, M (mm)	Bar Width (mm)	Solidity (%)	Downstream Distance x (mm)	(x/M)
Grid 1	203	38	34	800	3.9
Grid 2	102	19	34	520	5.1
Grid 3	305	75	43	1060	3.5

Table 4.3: Parameters describing the turbulence grid configurations used

The tube more than doubled the shaft diameter from 25.4mm to 55mm and it was hoped that this would highlight any effects of the wake from the hub on the sound radiation.

4.6.4 Inflow Turbulence

As discussed in chapter 3, one of the main advantages of VAWTs is that they perform well in gusty, turbulent wind environments. Typically the length scale of a gust is much greater than the diameter of a VAWT, even in an urban wind environment McIntosh [2009]. The gust response of a VAWT can therefore be treated as quasi-steady. There will however be smaller scales of turbulence in the wind that may affect the performance of a VAWT, particularly in terms of noise generation. There is very little data on the small scale turbulence found in the wind and this is partly due to the fact that the turbulence intensity is likely to be very site specific.

In order to determine the impact of inflow turbulence on the noise radiation from the model VAWT, a series of three turbulence grids of varying size were placed in the wind tunnel upstream of the rotor. The intensity of the turbulence generated by the grids was determined by using a hotwire measurement to find the ratio of the unsteady and mean components of the incoming flow. While the expected turbulence length scale in the wind was not known, it was hoped that, by looking at a range of different length scales, the general effect of inflow turbulence on noise generation could be determined.

The grid geometries are shown below in figure 4.15. Due to the way the turbulence grids were mounted in the tunnel they were not all placed the same distance upstream of the rotor. The distance x in figure 4.15(d) for each of the three turbulence grids is given in table 4.3. These distances were not sufficient to allow the full development of isotropic turbulence, but this was not essential for these experiments. The general characteristics of the inflow turbulence could still be determined from the measurements, which allowed a comparison of the three cases to be made.

(a) Grid 1

(b) Grid 2

(c) Grid 3

(d) Side view
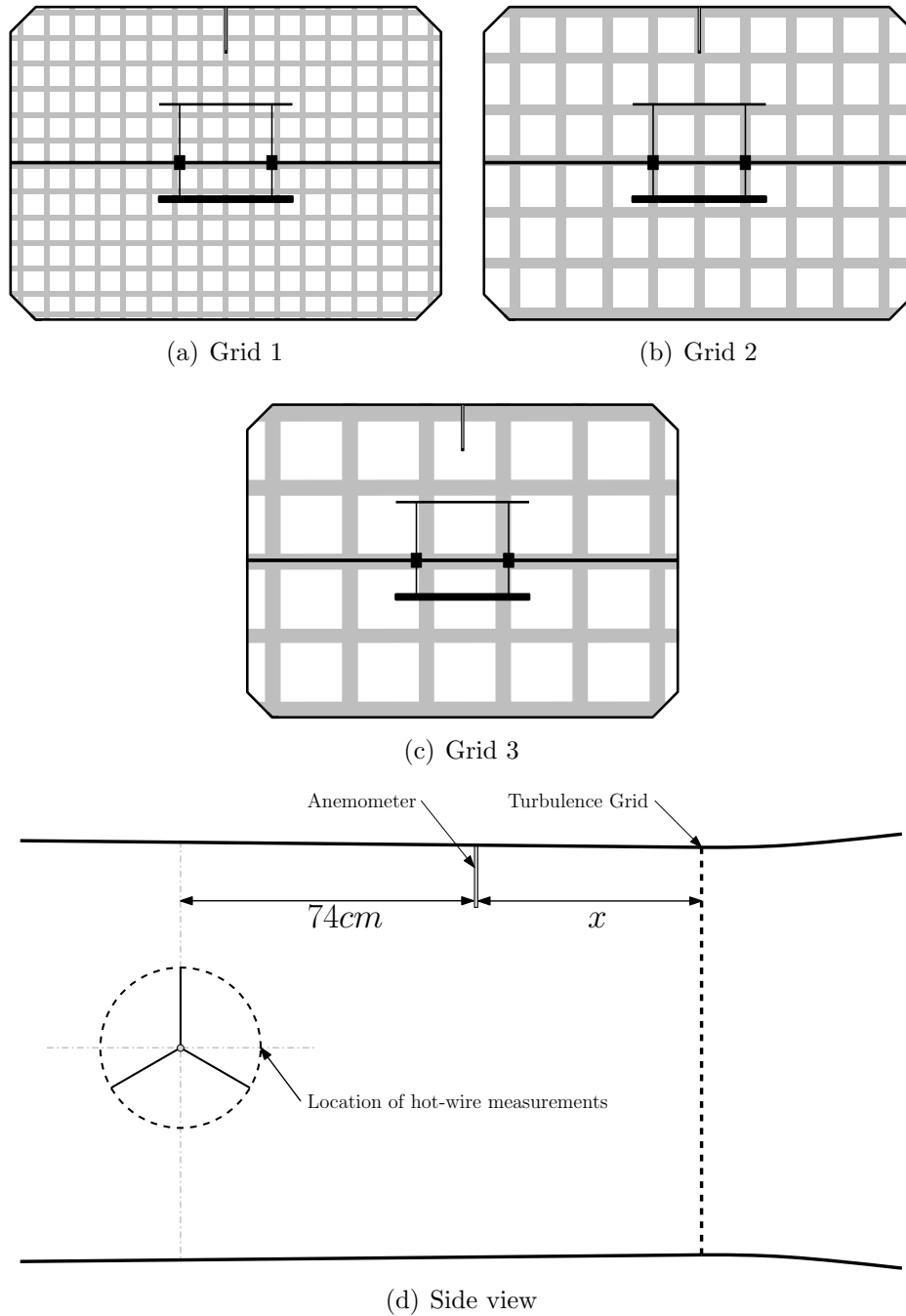
Figure 4.15: Schematics of the three turbulence grids used plus diagram to indicate their location relative to the model VAWT and the flow measurement devices.

Before the rotor was installed the turbulent flow was measured using a hot-wire anemometer at the location indicated in figure 4.15(d) for a range of tunnel speeds between 1m/s and 15m/s to cover the entire working range used in the experiments. For good convergence of the turbulence statistics, the velocity was sampled at 10kHz for 100sec giving 10^6 data points. From these data, estimates of the turbulence intensity and autocorrelation length were calculated (for calculation methods see, for example, Tennekes and Lumley [1972]).

In the standard experiments, without the turbulence grids, the tunnel speed was computed by measuring the dynamic pressure in the working section of the tunnel. The unsteadiness of the flow with the grids in place made it impossible to estimate the mean flow velocity using a standard pitot-static probe, so a calibrated, digital hot-wire probe was used instead (Chauvin Arnoux CA-826 Thermo-Anemometer). The probe was located as shown in figure 4.15(d). This probe still measured an unsteady velocity, but had a built in averaging function which allowed the mean velocity to be quickly and easily estimated to within ±0.25m/s.

The placement of the anemometer required some care since it was necessary to be sufficiently far from the turbulence grid to avoid the local acceleration/retardation of the flow, while also being far enough from the rotor to avoid acceleration of the flow due to tunnel blockage effects. For simplicity it was decided to locate the probe approximately half way between the grid and the rotor hub. The probe was also inserted sufficiently far into the flow to avoid any boundary layer effects at the tunnel walls. When taking the average flow speed measurements it was found that a 10sec average provided a relatively stable result for all cases. The variation observed in the 10sec average was greater than the resolution of the anemometer but was never more than ±0.5m/s.

Array measurements were made for the 3-bladed rotor, spinning both clockwise and anticlockwise, for the five TSR cases specified in table 4.2.

4.6.5   Boundary Layer Trips

In order to investigate the possible impact of laminar boundary layer tonal noise, trips were added to the blades. Three combinations were tested: just the outer surface tripped, just the inner surface tripped and both surfaces tripped. These tests were only conducted on the 3-bladed rotor as it was assumed that the effect of tripping the boundary layers would be the same on any of the rotors.

4.7 Summary

This chapter has described the physical and numerical tools used to investigate the noise radiated from the model VAWT rotor. A range of rotor geometries and operating conditions was selected for the experiments, and the means of testing these parameters was described. The results from all of these test cases, and the various processing methods described, are presented in the next chapter.

Chapter 5

Analysis of Experimental Results

This chapter presents the results from the wind tunnel experiments. The analysis of this data attempts to locate and identify the dominant sound sources on the model scale VAWT. Two principal methods of analysis were used: comparison of the sound spectra for the different cases and examination of the beamforming plots.

The limitations of the beamforming algorithm in this experiment were highlighted in section 4.3 and these issues meant that interpreting the beamforming plots required some care. The general approach was to first identify the differences between the spectra radiated by the various cases and then focus the beamforming investigations on these regions. It is important to note that two very similar spectra could have been radiated from different source locations so it was still necessary to examine the beamforming plots independently.

The difficulty of interpreting the results meant that, in general, no single piece of data provides conclusive evidence about the nature of a sound source. Instead the combination of multiple results from both the spectral and beamforming analyses is used to make the case for the different sound sources on the various rotor configurations and operating conditions.

5.1   Comparison with full-scale rotor

Noise measurements were carried out on the full-scale QR5 rotor by ISVR Consulting in accordance with BS EN 61400, which is the British standard governing the measurement of noise from wind turbines (see Brown [2007]). A power generating VAWT aims to always operate at the TSR that coincides with its peak power output, which for the QR5 rotor is approximately 3.5. Noise data were acquired for wind speeds from 6m/s-10m/s, although the data for the low wind speed cases are relatively sparse since the noise from the rotor was not measurable

<div align="center">(a) QR5 Rotor   (b) Wind tunnel model</div>

Figure 5.1: Comparison of the spectra radiated by the full-scale QR5 operating at TSR=3.5 rotor and the model-scale rotor operating at TSR=3

above the background noise at a number of frequencies.

Noise measurements were made in the wind tunnel to mirror the measurements conducted on the full-scale rotor. The 3-bladed rotor was run at TSR=3 at tunnel speeds from 4m/s to 8m/s in both directions of rotation. Similar to the full-scale noise measurements, the low speed 4m/s case was of poor quality so was not included in the analysis. A comparison of the 1/3rd octave spectra from both the full-scale and model-scale rotors is presented in figure 5.1.

There are clear qualitative similarities between the two sets of spectra. Firstly the rate of increase of the spectral amplitude with wind speed below 1kHz is very similar between the two rotors. Secondly there is a clear broadband peak around 2kHz in both sets of spectra, whose peak frequency and amplitude increase with increasing wind speed. This comparison suggests that the noise generating behaviour of the model-scale rotor is broadly similar to the full-scale rotor, meaning that the conclusions drawn from the experimental measurements should be transferable to a real VAWT.

It is perhaps surprising that these features of the spectra are observed at similar frequencies despite the substantial difference in the size of the two rotors. This behaviour is mostly due to the fact that, despite the size difference, the blades on the two rotors experience similar velocities. This does not explain all of the features observed in the spectra however, and a more detailed examination of the spectral scaling is undertaken in section 5.2.3.

5.2 Spectral Analysis

To investigate the spectra radiated by the model VAWT a range of techniques was adopted. Narrowband spectra were computed to investigate the harmonic content of the sound field, while 1/3rd octave spectra were calculated to examine the stochastic components of the sound. Spectral scaling methods were then used on the 1/3rd octave spectra to aid identification of the sound sources. The spectra were also integrated to estimate the total sound power radiated.

5.2.1 Harmonic Sound

The deterministic component of VAWT blade loads will radiate a purely harmonics sound field, so narrowband spectra with a frequency resolution less than 1Hz were computed to see if the spectra contained harmonic peaks. The high block-size required to produce these spectra reduced the number of blocks available for averaging, which meant that when the tunnel speed was high the boundary layer noise was not completely averaged out. As such it was difficult to identify harmonic peaks in the TSR=1 spectra at higher frequencies.

5.2.1.1 Effect of Tip Speed Ratio

The harmonic spectra for the 3-bladed rotor spinning anticlockwise[1] are presented in figure 5.2. The high noise levels are clear in the TSR=1 spectrum so the discussion that follows does not refer to this specific result. The first obvious conclusion to draw from the spectra in figure 5.2 is that there is clearly a strong harmonic component to the sound field. The next important conclusion is that the number of harmonics of the angular frequency that are radiated reduces as the TSR increases. At TSR=2 harmonic peaks are visible up to the 96th harmonic of the angular velocity, which approximately equals 1kHz. At TSR=3 harmonic peaks are only visible up to around the 40th harmonic and for TSR=5 this has reduced further to only around 20 harmonics being visible.

At low TSR, where the blades experience dynamic stall, there are likely to be rapid loading fluctuations, which will result in high harmonics of the angular velocity in the blade loading. As the TSR increases the angle of attack variation becomes approximately sinusoidal in nature and avoids any stall phenomena, so the blade loading should contain fewer harmonics of the angular velocity. The reduction in the harmonic content of the sound field with increasing TSR is therefore consistent with the unsteady loading induced by dynamic stall being a strong sound source at blade loading harmonics up to around the 90th harmonic

---

[1]Anticlockwise rotation is defined as being when the VAWT blades were travelling towards the array in the downstream half of the rotor.

(a) TSR=1, Ω=8.9Hz, U_∞ =14.8m/s

(b) TSR=2, Ω=11.3Hz, U_∞ =9.4m/s

(c) TSR=3, Ω=12.0Hz, U_∞ =6.4m/s

(d) TSR=4, Ω=12.2Hz, U_∞ =5.1m/s

(e) TSR=5, Ω=12.4Hz, U_∞ =4.1m/s
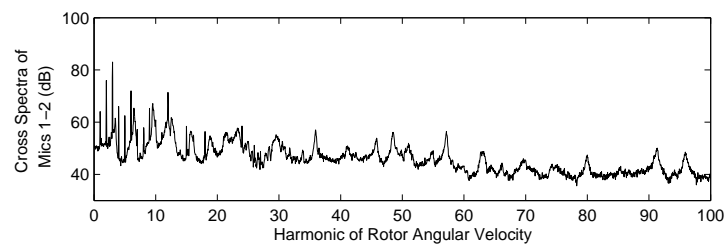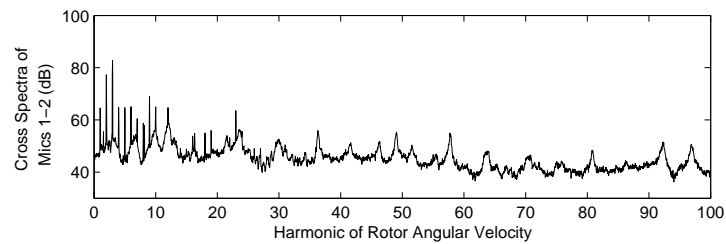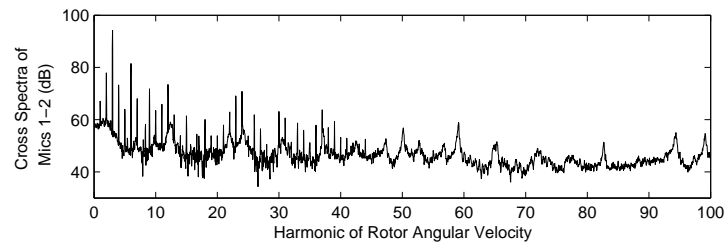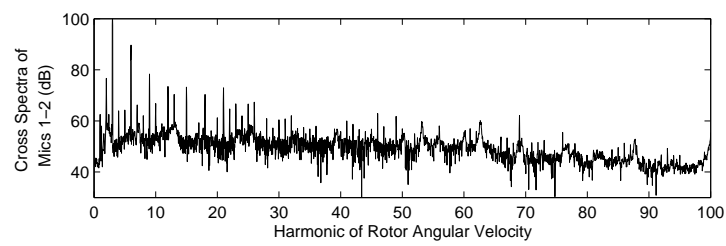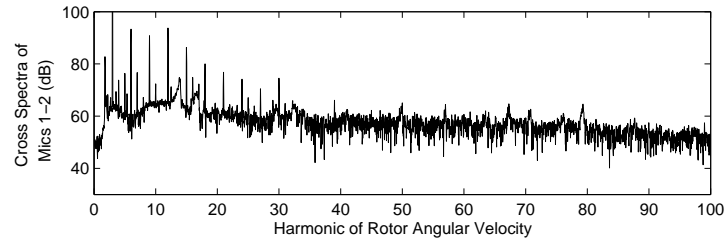
Figure 5.2: High resolution cross-spectra of microphones 1 and 2 for the
3-bladed rotor spinning anticlockwise.

95

of the rotor angular velocity. For the model scale rotor the 90th harmonics was at around 1kHz, while for the QR5 rotor at full speed it would be at around 360Hz.

Blade-vortex interaction (BVI) was suggested as another potential source of unsteady loading, but if intense, periodic blade loading fluctuations were being generated by this mechanism then one would expect to see it at all TSR, not just at low TSR. In fact, the VTM simulations of Scheurich [2011, p.82] suggested that BVI would be more of an issue at higher TSR. This was because, at low TSR, the spacing between the wakes shed by consecutive blades was greater due to the relatively higher free stream velocity, resulting in a less intense wake. It is also important to note that BVI noise might not generate harmonic sound because the stochastic nature of the wake turbulence could mean that the interactions are not entirely periodic, in which case a more broadband sound would be radiated.

5.2.1.2 Effect of Rotor Solidity

Increasing the rotor solidity has the effect of increasing the rotor induction factor at a given TSR. This will mean that there is more deflection of the incoming flow, which reduces the angles of attack experienced by the blades in the upstream half of the rotor. If the assumption that the sound harmonics are being radiated by unsteady loads induced by dynamic stall is correct, then it would be expected that a higher solidity rotor would have a fewer harmonics in the sound field.

The effect of rotor solidity on the harmonic content of the spectra at TSR=3 is shown in figure 5.3. There is not a great reduction in the harmonic content of the spectra between the 2-bladed and 3-bladed rotors, but there is a significant reduction in the harmonic sound from the 4-bladed rotor. This supports the assumption that the harmonic noise is being radiated by the unsteady loading that occurs during dynamic stall.

It is also interesting to note that the blade passage frequency harmonics are more prominent for the lower solidity rotors. This implies that the unsteady loading is more periodic in nature than for the higher solidity, 4-bladed case. This may indicate that the loading due to dynamic stall is relatively periodic, compared to any blade wake interaction loads.

5.2.1.3 Inflow Turbulence

Three turbulence grids were placed in the tunnel as described in section 4.6.4, and the flow turbulence was measured using a hot-wire probe without the rotor in the tunnel. The turbulence generated by a grid does not become isotropic until at least 30 mesh lengths downstream, whereas the rotor in these experiments was, at most, 5 mesh lengths from the grid. This means that the flow measured by the hot-wire probe was probably unique to the specific measurement location. Since

(a) 2-Bladed
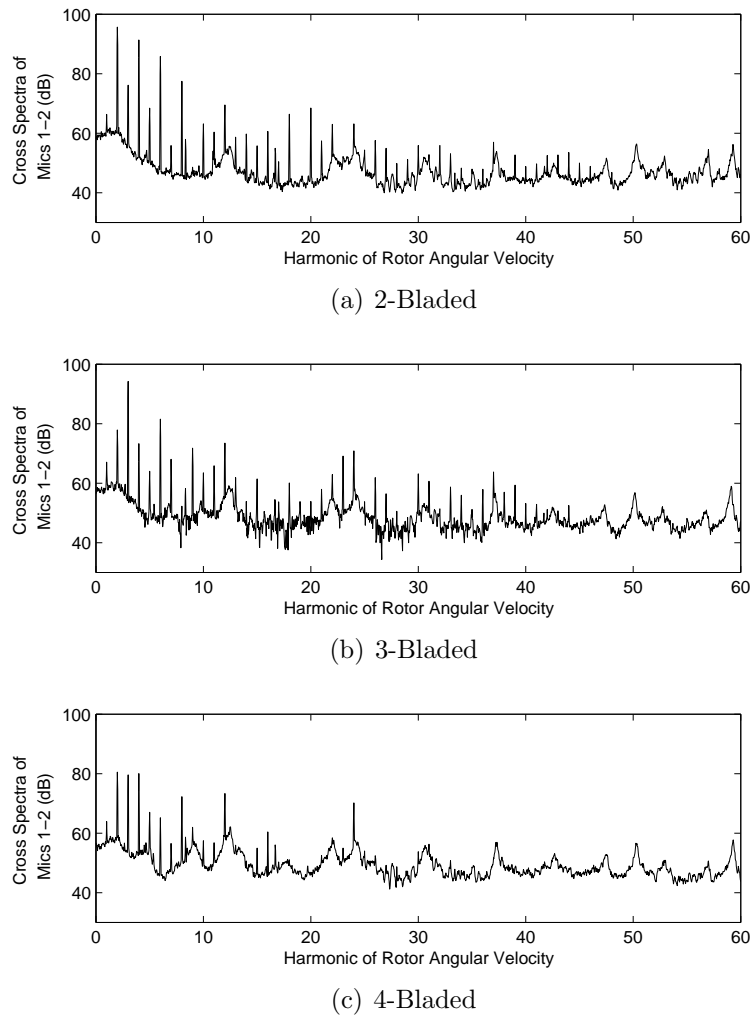
(b) 3-Bladed

(c) 4-Bladed

Figure 5.3: High resolution cross-spectra of microphones 1 and 2 for the 2-, 3- and 4-bladed rotors spinning anticlockwise at TSR=3 (Ω=12.0Hz, U_∞=6.6m/s).
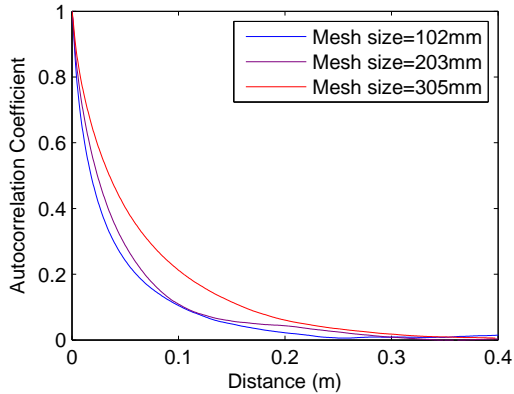
Figure 5.4: Mean autocorrelation curves for each grid

Mesh Size	Turb. Intensity	Autocor. Length
102mm	7.6%	43mm
203mm	16%	47mm
305mm	19%	63mm

Table 5.1: Turbulence statistics for each grid

the exact turbulence statistics were not essential to this experiment however, the general characterisation of the turbulence obtained through these measurements was sufficient. The spatial autocorrelation coefficients were computed for each grid and are plotted in figure 5.4. An estimate of the autocorrelation length was then found by integrating the autocorrelation curves for each grid, as described in section 4.6.4 (see table 5.1).

The array measurements with the turbulence grids in place were significantly affected by the noise radiated by the flow through the grids. The noise with just the turbulence grids in the tunnel was measured and the cross spectra of mics 1-2 was computed for comparison with the signal from the model without the grid in place. The results of this analysis for grid 3 (mesh size 305mm) are plotted in figure 5.5, and the spectrum radiated by the 3-bladed rotor operating at TSR=1 are shown for comparison. From figure 5.5, it is evident that the spectra for the TSR=1 case (U_∞=14.8m/s), where the tunnel speed was highest, were likely to be completely dominated by the noise from the grid, so have been ignored in the discussion that follows. This is not too limiting since the TSR=1 condition is well away from the target operating condition of all lift-type VAWTs.

The harmonic spectra were computed for all three grids at all TSR and compared with the smooth inflow cases. The spectra for the 3-bladed rotor spinning clockwise at TSR=3 are presented in figure 5.6 and are representative of the general trends observed. The obvious conclusion is that the turbulent inflow significantly alters the harmonic content of the spectra. This would be the case if the stochastic unsteady loading due to the turbulent eddies was greater in amplitude than the unsteady loading due to the general aerodynamics of the VAWT rotor. Alternatively, the turbulent inflow could have disrupted the aerodynamics of the VAWT, thereby reducing the unsteady periodic loading component.
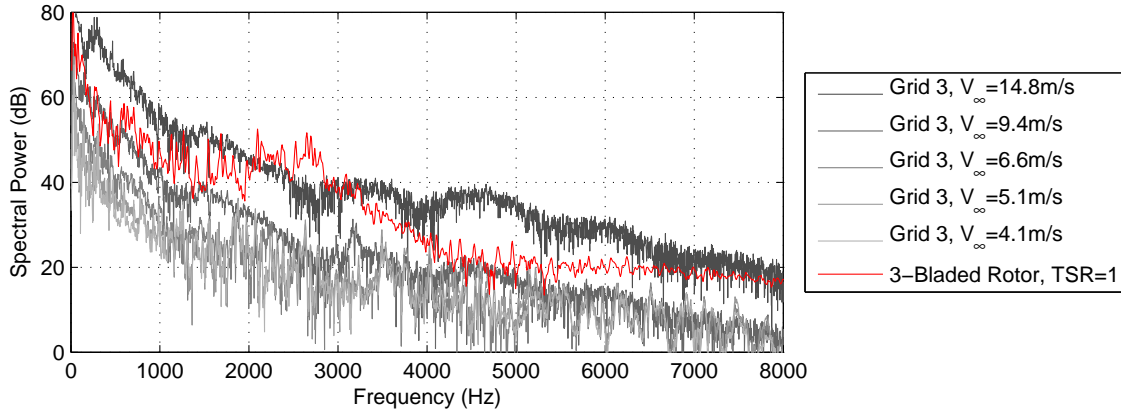
Figure 5.5: Plot of the noise radiated from turbulence grid 3 at the free stream velocities used for TSR 1-5. The spectrum of the 3-bladed rotor at TSR=1 with no grid in place is shown for comparison.

Looking at the amplitude of the broadband component of the spectra for the turbulent inflow cases, this level is close to the amplitude of the harmonic peaks for the smooth inflow case. One would still expect to be able to see the harmonic peaks above this level, if they were not reduced in amplitude by the turbulent inflow. As such it is not possible to definitively say whether the reduction in harmonic content is due to the harmonic source being disrupted or being swamped by the stochastic noise from the turbulent inflow. In all probability it is a combination of the two.

5.2.1.4   Harmonic Versus Broadband Component

It is possible to make a definitive assessment of the extent to which the harmonic component of the sound contributes to the overall energy content of the spectra. In the harmonic spectra, the frequency resolution is equal to 32 points for each harmonic of the rotor angular velocity. Given that the spectra are plotting dB/Hz, for the harmonic peak within a block to be radiating the same amount of energy as the broadband component within that block, it's amplitude must therefore be 31 times greater. This is approximately equal to a 15dB difference between the harmonic and broadband levels.

The implication is that any harmonic peak which is less than 15dB greater than the broadband level will not be the dominant feature of the spectra. Assessed against this criteria, the extent of the harmonic component is seen to be much less. In the 1/3rd octave spectra, the majority of the energy is therefore from the broadband sources rather than the harmonic sources. This explains why it is satisfactory to use 1/3rd octave spectra to assess the broadband component of

99
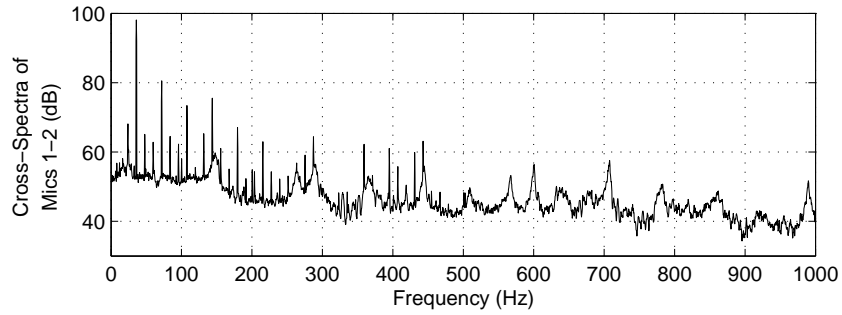
(a) No Grid
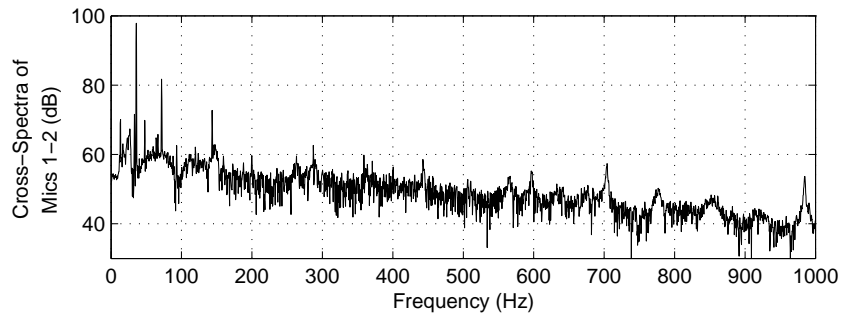
(b) Grid 1, Mesh Size = 102mm
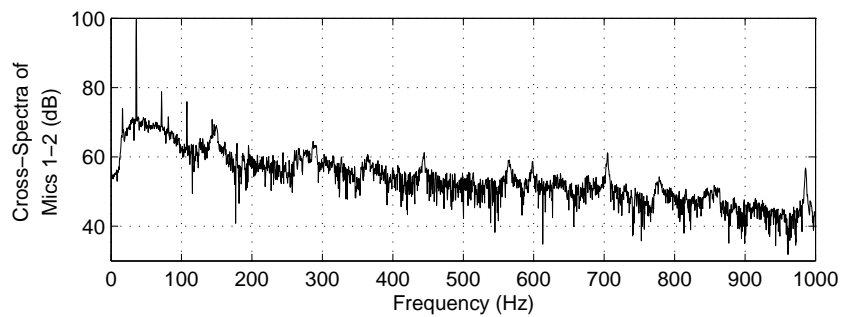
(c) Grid 2, Mesh Size = 203mm
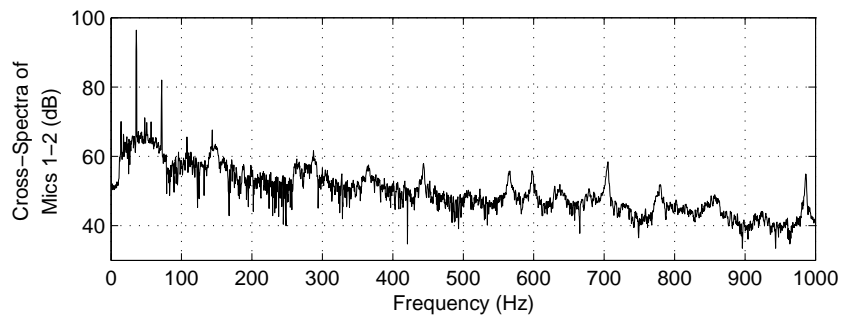
(d) Grid 3, Mesh Size = 305mm

Figure 5.6: Plots showing the change in the harmonics content of the spectra when the inflow is turbulent rather than smooth (TSR=3, Ω=12.0Hz, U_∞=6.6m/s)

100
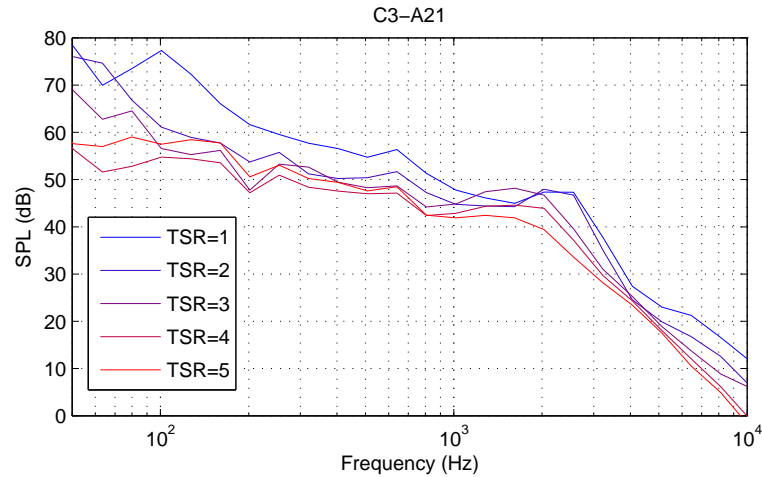
Figure 5.7: Plot showing the 1/3rd octave spectra for the 3-bladed rotor spinning anticlockwise at a constant blade relative velocity of 21m/s

the spectra, even in the range where some harmonic peaks are still observed.

5.2.2 Broadband Spectra

Analysis of the harmonic content of the spectra indicated that the spectra were almost completely stochastic in origin above 1kHz, and still had a strong stochastic component at lower frequencies. This meant that broadband or 1/3rd octave spectra were sufficient to investigate the sound field radiated by the model VAWT rotor. One advantage of using broadband spectra was that the lower blocksize required gave many more blocks for averaging, and hence excellent smoothing of the broadband components of the spectra.

5.2.2.1 Effect of Tip Speed Ratio

The 1/3rd octave spectra are best for showing the overall trends in broadband sound output, and these spectra from the 3-bladed rotor at a range of TSR are shown in figure 5.7. (Note that these are the same cases as were shown in the harmonic spectra plots in figure 5.2). From figure 5.7 it is clear that the broadband peak in the region 1-3kHz is influenced by changes in TSR. The peaks for the TSR=1 and TSR=2 cases are different in shape and location which implies a different source mechanism. The beamforming plots in this frequency range were therefore examined to see if the location of the sources also changed (see next section). The changes in this peak as the TSR increased from 3-5 were more subtle and this source is investigated in more detail in the section on spectral scaling (section 5.2.3).

(a) TSR=1   (b) TSR=5
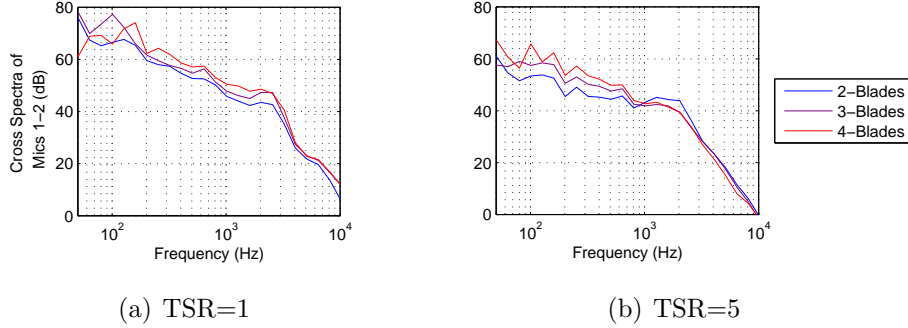
Figure 5.8: Plots showing the 1/3rd octave spectra at TSR=1 (Ω=8.9Hz, U_∞=14.8m/s) and TSR=5 (Ω=12.4Hz, U_∞=4.1m/s) for the three different rotor solidities, at a constant relative blade velocity of 21m/s.

It is equally notable that large parts of the spectra remain unaffected by the changes in TSR. In particular the region from 100-1000Hz is very similar for the TSR=2-5 cases. The implication is that the broadband component of the sound field in this region is not affected by the changes in the aerodynamics with TSR, but is more strongly influenced by the variable that is being held constant, namely the blade relative velocity. This suggests that the sound in this region is radiated by a self-induced source, such as trailing-edge noise.

5.2.2.2 Effect of Rotor Solidity

Comparing the broadband spectra for different solidity rotors was not straightforward since there were no consistent differences between the cases. One general conclusion that can be drawn from the spectra for the different solidity rotors, shown in figure 5.8, is that the noise amplitude does not simply scale with the number of blades at low TSR. If it did then one would expect a constant difference of 3.2dB between the 2- and 3-bladed rotors and 2.49dB between the 3- and 4-bladed rotors. The fact that this is not the case confirms that the change in solidity also changes the noise source mechanisms.

At higher TSR however, the region of the spectra from 100-500Hz does approximately scale with the number of blades. The implication is that at the higher TSR the flow conditions are more similar between the three different rotors, resulting in similar source mechanisms. This conclusion does not extend to the whole spectrum however, since above 500Hz this trend is no longer observed.

One further feature of the spectra that is worth noting is the amplitude of the broadband peak around 2kHz. At TSR=1 the 4-bladed rotor has the highest amplitude in this region and the 2-bladed rotor has the lowest but at TSR=5
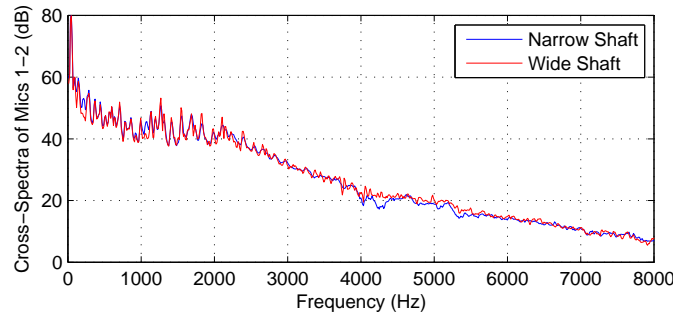
Figure 5.9: Comparison of the spectra radiated from the 3-bladed rotor at TSR=3 with and without the wide shaft.

this is reversed. It is not obvious what causes this change, but one possibility is that the change in the induction factor with TSR is different for different solidity rotors. If the amount of blockage increased faster for the higher solidity rotors this might result in the blades experiencing relatively lower velocities at certain points in the rotation thereby resulting in less noise radiation. Detailed flow measurements would be required to confirm whether or not this is the case.

5.2.2.3 Effect of Wide Shaft

Broadband spectra for the 4-bladed rotor at TSR=3 with and without the wide shaft are presented in figure 5.9. It is clear from this plot that the shaft width had no discernible effect on the noise radiated in this case. Comparisons of the spectra with and without the wide shaft were undertaken for all TSR and rotor solidities and the results were all similar to that shown in figure 5.9. The obvious conclusion is that the wake from the shaft has no significant impact on the noise radiated from a VAWT rotor. Due to the similarity between the spectra it was not deemed necessary to look at the wide shaft cases in the beamforming analysis.

5.2.2.4 Effect of Inflow Turbulence

The 1/3rd octave spectra were computed for the three different turbulence grids at all TSR. Plots comparing the spectra radiated by the 3-bladed rotor for different levels of inflow turbulence are shown in figure 5.10 at three different TSR. It is evident that as the TSR increases the impact of the inflow turbulence becomes less.

The relative velocity of the blades is made up of the wind velocity and the blade velocity, but as the TSR increases this relative velocity will be increasingly dominated by the blade velocity. Fluctuations in the incoming flow will therefore produce a much smaller change in the blade aerodynamics at high TSR than they
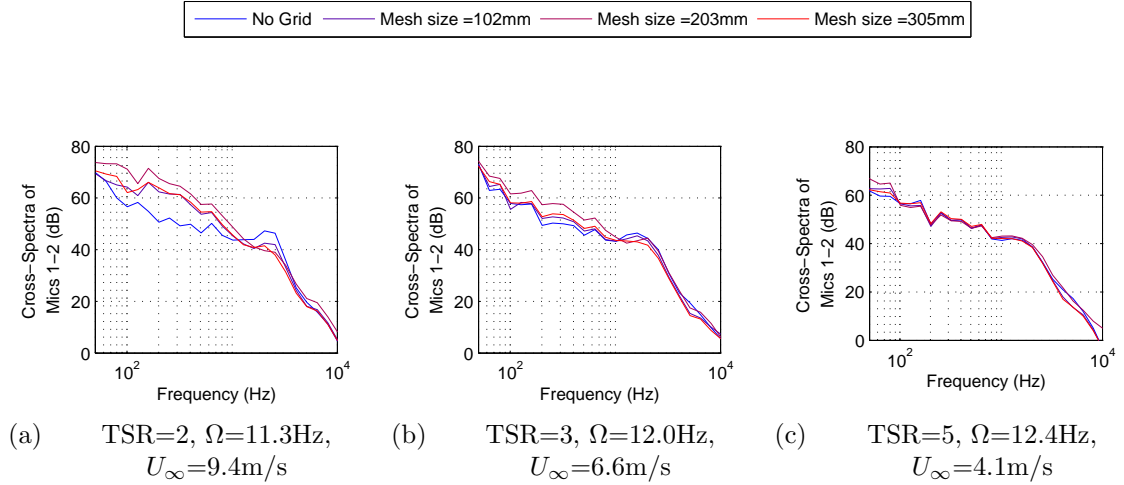
Figure 5.10: Plots showing the impact of the inflow turbulence grids on the radiated spectra at three different TSR.

would at low TSR. This explains why there is almost no change in the spectra for the TSR=5 case at the different levels of inflow turbulence. The implication is that in a turbulent wind environment there may be certain advantages to running the rotor at higher TSR as it would give more predictable aerodynamic and noise performance.

5.2.3 Spectral Scaling

The spectral scaling methods outlined in the previous chapter were applied to the constant TSR=3 cases. These cases were chosen since, at fixed TSR, the rotor aerodynamics were expected to be the same at all tunnel speeds. This meant that the effects of changing angle of attack could be ignored, which significantly simplified the scaling process. A plot of the 1/3rd octave spectra for the 3-bladed rotor operating at a constant TSR of 3 for a range of tunnel speeds is shown in figure 5.1(b).

The spectral scaling stages were applied sequentially to deduce information about the sound sources. Firstly the Strouhal scaling was applied using the boundary layer thickness as the relevant length scale. Secondly the amplitude was adjusted using the velocity scaling defined in equation 4.15, and finally the Reynolds number scaling of the LBL-VS peak was applied. The spectra resulting from each of these three steps are shown in the three plots of figure 5.11.

From figure 5.11(a) it can be seen that the Strouhal scaling resulted in the broadband peaks of all the spectra converging on a Strouhal number of approx-

imately 0.2. The convergence of all the spectra implicitly validates the scaling method used, which in turn suggests that the broadband peak is the result of laminar boundary layer tonal noise. In addition the convergence on a Strouhal number of 0.2 is consistent with the measurements of Paterson et al. [1973].

The spectra resulting from the velocity scaling are shown in figure 5.11(b). There is very good convergence of the spectra in the range of Strouhal number from 0.02-0.1, which suggests that this component scales with the fifth power of the velocity. As discussed previously, this implies that the source in this region is the trailing edge, although it is not possible to determine whether noise is due to inflow turbulence or self-induced boundary layer turbulence. This result is consistent with the data for the constant blade relative velocity cases shown in figure 5.7, where the amplitude in this region was unaffected by the changes in TSR. It is also worth noting that this velocity scaling does not cause the amplitude of the broadband peaks to converge.

Figure 5.11(c) shows the spectra after the scaling function $G2$ of Brooks et al. [1989] has been applied. A good convergence of the broadband peak is observed, which suggests that an appropriate scaling procedure has been used. The best convergence of the broadband peak was found to occur when $G2$ was calculated using a velocity of (TSR+1) times the wind speed and an angle of attack of zero: these are the values experienced by the blades as they are travelling upstream. Given the sensitivity of this scaling step to the values of velocity and angle of attack, the implication is that the laminar boundary layer noise is probably being radiated at this point in the blades' rotation.

As the name implies, laminar boundary layer noise is only radiated while the boundary layer remains laminar. The noise from this source can therefore potentially be reduced by tripping the boundary layer to turbulence. The effect of tripping is described in the next section.

5.2.4 Boundary Layer Tripping

The spectral scaling analysis strongly suggested that the broadband peak observed at around 2kHz was due to laminar boundary layer tonal noise. Paterson et al. [1973] showed that this source could be eliminated by applying a simple boundary layer trip to the pressure surface of the aerofoil. This approach was adopted here (as described in section 4.1.5) with a zig-zag strip of aluminium tape being applied first to the outer blade surfaces, then the inner surfaces and finally to both surfaces simultaneously. The results of applying these trips to the 3-bladed rotor spinning anticlockwise at TSR=3 are shown in figure 5.12.

While applying the boundary layer trip to the outer surface of the blades had little effect on the spectrum, the trip on the inner surface clearly made a significant difference. The broadband peak between 1kHz-3kHz was almost
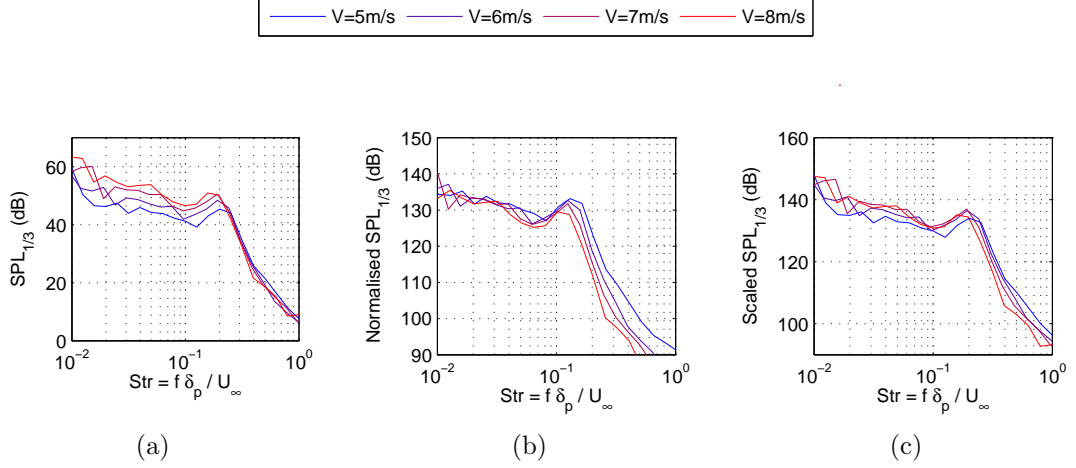
Figure 5.11: Plots showing the sequence of scaling operations on the 1/3rd octave spectra from figure 5.1(b) (a) Strouhal scaling applied, (b) Velocity normalisation of equation 4.15 applied, (c) LBL-VS scaling function $G2$ from Brooks et al. [1989] applied.

completely removed, with the spectral amplitude in this region being reduced by as much as 10dB. This is conclusive evidence that the peak was due to laminar boundary layer noise. This result was found to be true for all TSR and it is safe to assume that it would also be true for all rotor solidities tested.

The spectral scaling had suggested that the sound was being radiated when the blade was travelling upstream. The fact that the inner surface trip removed the noise source suggests that this was the pressure surface when laminar boundary layer noise was being generated. The inner surface of the blade is the pressure surface in the downstream half of the rotation, but the outwards deflection of the incoming flow means that it remains the pressure surface until the blade is slightly into the upstream half of the rotation. The inner surface trip removing the laminar boundary layer noise is therefore consistent with the source location inferred from the spectral scaling process. The location of this source is investigated further in the analysis of the beamforming plots (see section 5.3.3).

The fact that laminar boundary layer noise is not radiated at other locations is not surprising at low TSR where the blade aerodynamics are dominated by separation and stall. At higher TSR it might be expected that this source would extend to other locations around the rotation. The PIV measurements of Edwards [2012] suggested, however, that even at TSR=4, the flow over the blades is at least partially separated for a significant portion of the rotation. In particular, the flow was found to be attached as the blades travelled upstream, but not as the
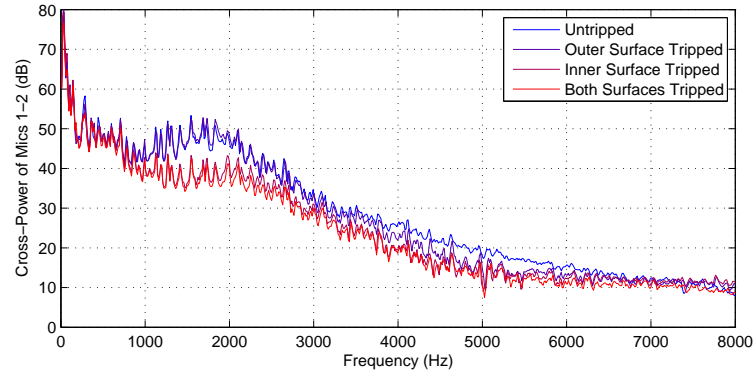
Figure 5.12: Plot showing the effect of tripping the boundary layers on the 3-bladed rotor at TSR=3.

blades travelled in the downstream direction. This was due to the greater rate of change of angle of attack as the blades travel downstream, and was shown to occur even when the blades did not exceed the static stall angle. Given that the mechanism by which laminar boundary layer tonal noise is generated is dependent on the feedback with the unstable Tollmien-Schlichting wave it is probable the unsteadiness experienced when the blade is stalled prevents noise being radiated in this way.

In the experiments conducted by Paterson et al. [1973] the boundary layers were tripped since they were expected to be tripped on the full-scale rotor. Here, however, that is not the case. The model rotor does operate at lower Reynolds numbers than a full-scale rotor, but since the relative Reynolds number of the two rotors is only a function of the blade chord, it is only three times higher on the full-scale rotor. This means that the boundary layers could remain laminar on the blades of the QR5 rotor. The spectra measured from the full-scale rotor exhibit a broadband peak in the region where laminar boundary layer noise is expected, so it is likely that tripping the boundary layers on the QR5 rotor would result in similar noise reductions.

There might be a slight negative impact on rotor efficiency due to the higher zero-lift drag, but the turbulent boundary layers might also delay blade stall, thus reducing the drag. Experiments would be required to determine the exact impact of tripping on rotor performance.

5.2.5 Total Sound Power

The averaged, unweighted total sound powers were computed as described in section 4.5.5 for all the cases measured. The noise radiation as a function of TSR

and rotor solidity at a constant relative blade velocity of 21m/s are presented in figure 5.13(a). The first point to note is that there is a general trend of decreasing noise with increasing TSR with the minimum total sound output achieved with the 3-bladed rotor at TSR=5. This trend is believed to be due to the fact that induction factor effects were not included in the calculation of the operating conditions for each TSR. A greater induction factor at high TSR means that the true relative blade velocities at high TSR are lower than the supposedly constant value.

It can be seen that the rate of noise reduction with TSR is increasingly rapid for higher rotor solidities. This is believed to be a result of the greater changes in rotor aerodynamics with TSR for the higher solidity rotors due to the increased induction factors. In real world applications the rotor is likely to spend a reasonable proportion of time operating away from the target TSR and the noise penalty for operating off design appears to be greater for higher solidity rotors. It is almost certainly not a coincidence that high solidity rotors also tend to have a higher efficiency penalty for operating off design (see section 3.2.1).

It is important to understand that these data do not mean that a rotor operating at a higher TSR will be quieter than one at low TSR for the same wind speed. Figure 5.13(b) shows how the sound power increases with TSR at constant wind speed. The measured data are shown in blue, and a correction term equal to the reduction in sound power at constant V_{rel} is added (in red). This data set is compared with the Mach number scaling laws for a moving dipole source (M^6) and trailing edge scattering (M^5). The relative velocity as the blades were travelling upstream was used to calculate the amplitudes at each TSR (i.e. $U_\infty(TSR + 1)$) with the TSR=1 case used as the reference condition.

From figure 5.13(b) the M^6 scaling appears to fit very well for the TSR=2 case (with the correction term added) and is generally a closer match than the M^5 scaling in all cases. The scaling is, however, highly dependent on the factor by which the free stream velocity is multiplied at each TSR. If, instead of $U_\infty(TSR + 1)$, one uses $U_\infty(TSR + 0.2)$ to account for a component of the induction factor effects, the M^5 was found to fit much better with the measured data. Without better aerodynamic data about the peak relative velocity experienced by the blades it is therefore difficult to say anything conclusive about the comparison with the scaling laws.

5.2.6   Summary of Spectral Analysis

The spectral analysis revealed a number of features of the noise sources on the model-scale VAWT rotor:

1. **Harmonic Sound:** There is a strong harmonic component to the sound
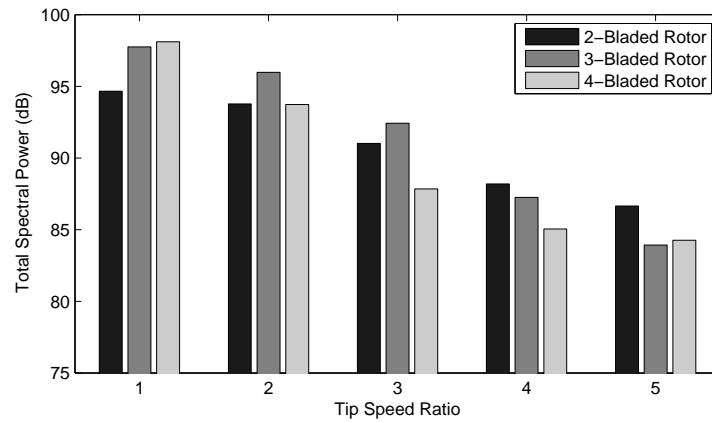
(a) Variation with TSR and solidity at constant V_{rel}
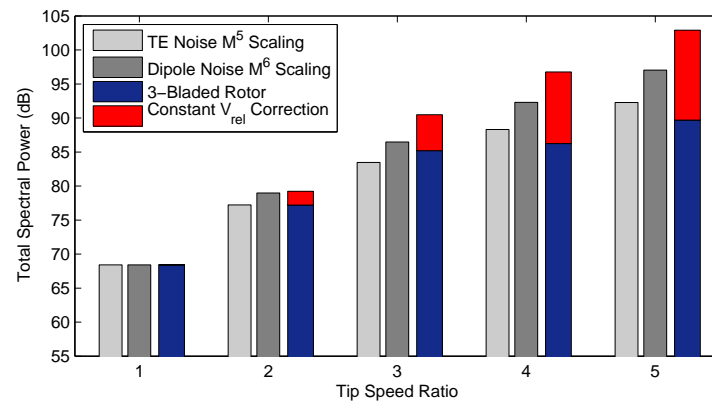
(b) Variation of 3-bladed rotor noise with TSR at constant U_∞=5m/s

Figure 5.13: Averaged unweighted total sound powers showing the trend with TSR and solidity. Total sound powers were computed as an average of multiple cross-spectra (mics 1-2), as described in section 4.5.5

radiated by the model-scale VAWT, which extends up to at least the 30th harmonic of the rotor angular velocity. The harmonic content of the source was seen to decrease with both increasing TSR and increasing rotor solidity. This was deemed to be due to reduced blade loading fluctuations and, in particular, the avoidance of dynamic stall. Inflow turbulence was also seen to disrupt the harmonic component of the sound with the stochastic blade loading radiating more noise than the periodic, deterministic blade loads at most frequencies.

The harmonic source scales with the rotor angular velocity, meaning that for a full-scale rotor the amplitude of the harmonics will be lower relative to the broadband components of the sound as a result of the lower angular velocities. It was estimated that for the QR5 rotor this source would only dominate up to the 20th harmonic of the angular velocity which is a maximum of 80Hz.

Due to the low frequency of the harmonic component of the sound field it was not possible to perform further investigations using beamforming as the resolution would have been too low.

2. **Broadband Sound:** The broadband component of the sound below 1kHz was shown to scale with the fifth power of the blade velocity. This implies that it is being radiated from the trailing edge of the blades. Above 1kHz a broadband peak was observed that was shown to be due to laminar boundary layer tonal noise. This source was successfully eliminated by placing a boundary layer trip on the inner surfaces of the blades. Beamforming analysis will be used to investigate this source further to confirm its location and to assess the impact of tripping the boundary layers on the dominant source location.

   Inflow turbulence was found to only have a significant effect on the noise sources at TSR<2. This was due to the fact that the blade velocity dominated the relative flow over the blades at higher TSR so the turbulent fluctuations only caused small changes in the blade aerodynamics. The spectra for the rotors with wide and narrow shafts were found to be virtually identical, which suggested that the interaction of the downstream blades with the shaft wake was not a significant source of noise.

3. **Total Sound Power:** The total sound power output showed that, at constant relative blade velocity there is a general trend of decreasing noise with increasing TSR. The rate at which the noise decreased was seen to be highest for the higher solidity rotors. It was suggested that this was due to the differences in the induction factor for the three rotors.

5.3 Beamforming Analysis

As previously discussed, the information available from beamforming is relatively limited for the case of the VAWT rotor. The objective was therefore not to precisely locate specific sources, but to observe trends in source location that could help to infer what the noise source mechanisms might be. The data presented below focus on a specific 1/3rd frequency band (unless otherwise stated) in order to demonstrate a given trend. The frequency bands investigated were identified from the spectral analysis, which indicated where differences in the beamforming output might be expected.

5.3.1 Effect of Tip Speed Ratio

The spectral analysis had indicated that there were changes in both the harmonic and broadband components of the spectra as the TSR was increased. The resolution of the array at low frequencies meant that it was not possible to investigate the harmonic source so the beamforming analysis focusses on the broadband source between 1kHz and 3kHz. Figure 5.14 shows the beamforming plots for the 3-bladed rotor spinning in both directions at the 1/3rd octave band with centre frequency of 1250Hz. In all of the beamforming plots in this report the flow is from left to right and a clockwise case is one in which the blades were travelling towards the array in the upstream half of the rotor. The location of the shaft is shown on the plots along with a box indicating the swept area of the rotor. The lines within the box give the location of the spokes.

The first significant feature to note in the beamforming plots is the clear shift in the dominant source location between TSR=2 and TSR=3. For both the clockwise and anticlockwise cases the dominant source at TSR=2 is in the upstream half of the rotor but at TSR=3 it has moved to the downstream half. At low TSR dynamic stall is expected in the upstream half of the rotor, but as the TSR increases this effect is expected to reduce. The beamforming plots appear to indicate that the noise radiated during dynamic stall is the dominant source on the 3-bladed rotor for TSR=1-2, but after that other sources dominate.

The plots for the clockwise and anticlockwise cases both show the same broad trends in dominant source location except at TSR=5. At this condition the strongest source in the clockwise case is in the upstream half of the rotor but is in the downstream half for the anticlockwise case. The amplitudes of the sources in the upstream and downstream halves of the rotor for both cases differ by only around 1-2dB, which is approximately what was expected to be observed as a result of Doppler amplification. Since this small Doppler effect is observed, the implication is that blades are radiating roughly the same noise levels at all locations and with no particularly strong directivity. At low blade Mach numbers
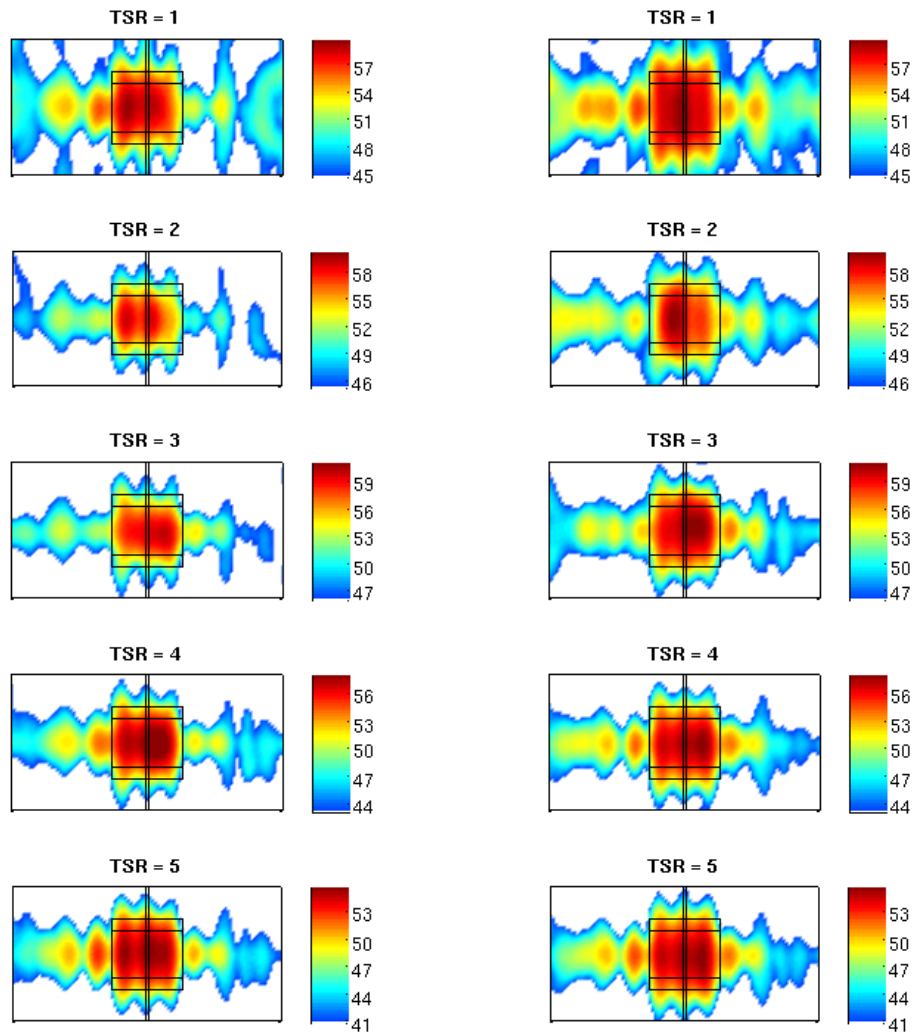
(a) Clockwise rotation   (b) Anticlockwise rotation

Figure 5.14: Beamforming plots for the 3-bladed rotor at the 1/3rd octave band with centre frequency of 1250Hz.

this is consistent with the dominant source being a self-induced mechanism such as turbulent boundary layer trailing edge noise.

5.3.2   Effect of Solidity

Analysis of the spectra indicated that increasing the rotor solidity at a fixed TSR had a similar effect to increasing the TSR of a fixed solidity rotor. Beamforming plots for the 2-, 3- and 4-bladed rotors at a range of TSR are presented in figure 5.15, which appear to confirm this trend. The beamforming plot for the 2-bladed rotor at TSR=3 is clearly very similar to the 3-bladed rotor at TSR=2, which implies that the blades are experiencing comparable aerodynamics in both cases. The same goes for the 2-bladed rotor at TSR=4 and the 4-bladed rotor at TSR=3.

A further point to note from these plots is that the noise source in the upstream half of the rotor, which was presumed to be due to dynamic stall, persists up to TSR=3 for the 2-bladed rotor. This highlights the fact that it is possible to control the nature of the noise source at a given TSR by changing the solidity of the rotor. In terms of rotor design this could mean that the the peak power output and the minimum noise output could potentially be engineered to occur at the same TSR.

5.3.3   Boundary Layer Tripping

Tripping the boundary layers on the inner surface of the blades was shown to remove the broadband peak in the spectra between 1kHz - 3kHz. Beamforming in this frequency range was carried out to identify where this source was being radiated from, and to see what effect removing the source had on the overall sound field. Figure 5.17 shows a comparison of the untripped 3-bladed rotor spinning anticlockwise and the same case with boundary layer trips on the inner surfaces of the blades. Given that the trip on the inner surface caused the reduction in noise it was expected that the source that was being affected was in the downstream half of the rotor and the beamforming plots confirm this. In all cases the source that was removed by the boundary layer trip was either in line with the hub or slightly downstream of it.

At all TSR there is a substantial reduction in the peak source amplitude of up to 11dB. Removing this intense laminar boundary layer noise also has the advantage of revealing some of the weaker sources in the beamforming plots. The dynamic stall noise at TSR=1-2 is very clearly highlighted but interestingly at TSR=2 the downstream noise source is already slightly louder than the upstream source. This may be due to the trips affecting the dynamic stall behaviour on the blades. Above TSR=2 the downstream noise source is then seen to dominate. It is important to note that this trend is also observed in the clockwise rotation
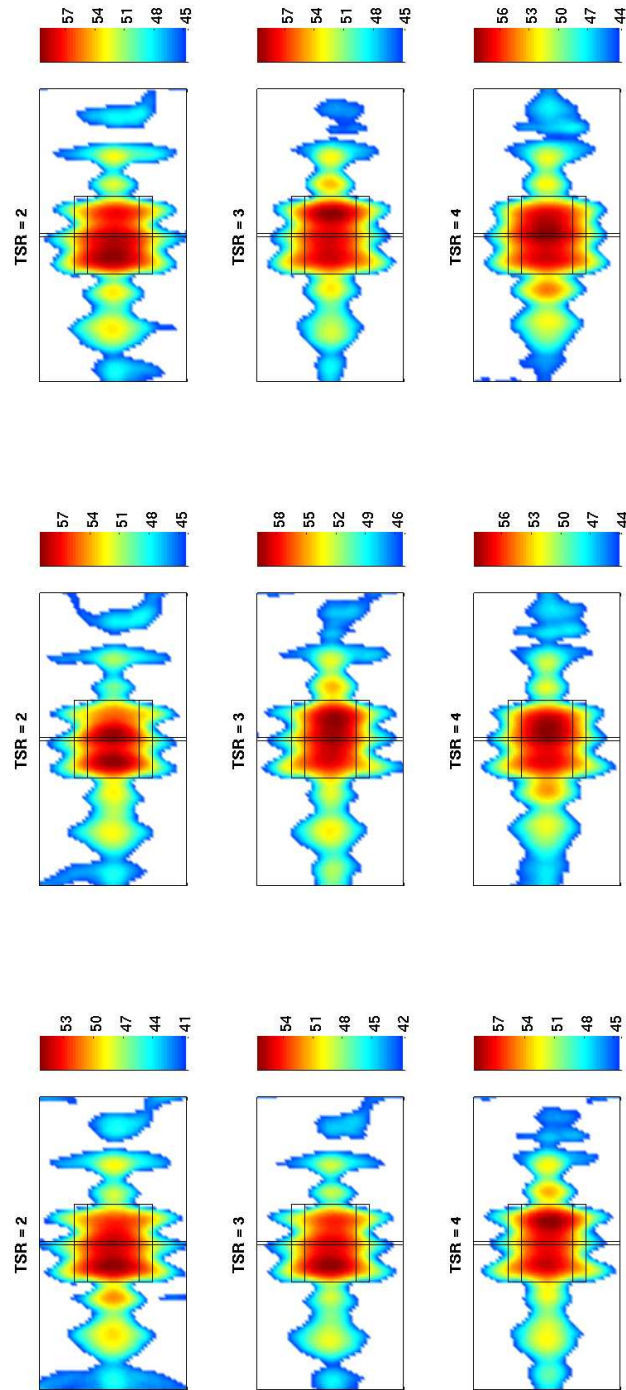
(a) 2-Bladed Rotor

(b) 3-Bladed Rotor

(c) 4-Bladed Rotor

Figure 5.15: Beamforming plots of the 1/3rd octave band with centre frequency 2000Hz showing the shift in source location for different solidity rotors (clockwise rotation).

(a) Untripped   (b) Inner surface tripped
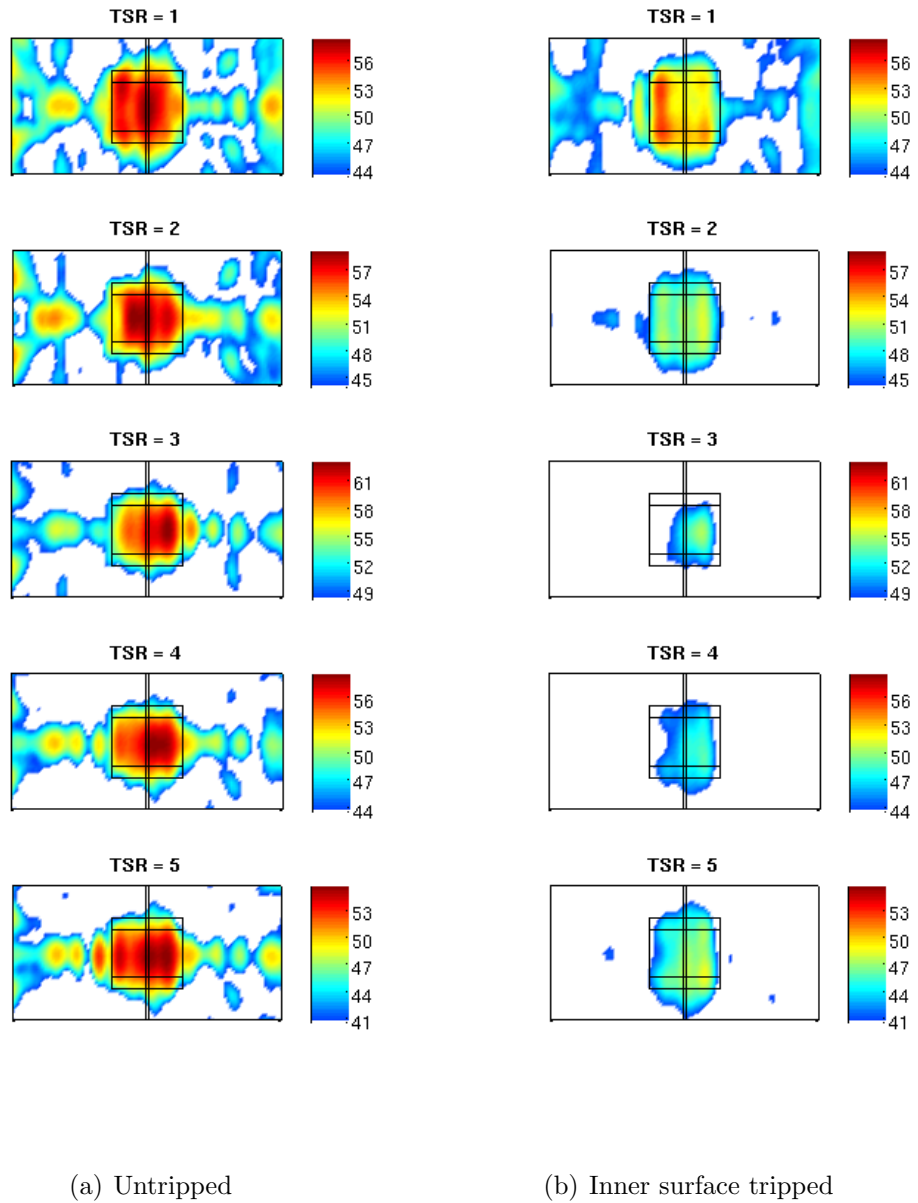
Figure 5.16: Beamforming plots at the 1/3rd octave band with centre frequency of 1600Hz for the 3-bladed rotor spinning anticlockwise, showing the effect of tripping the boundary layers on the inner surface of the blades.

(a) Clockwise (b) Anticlockwise
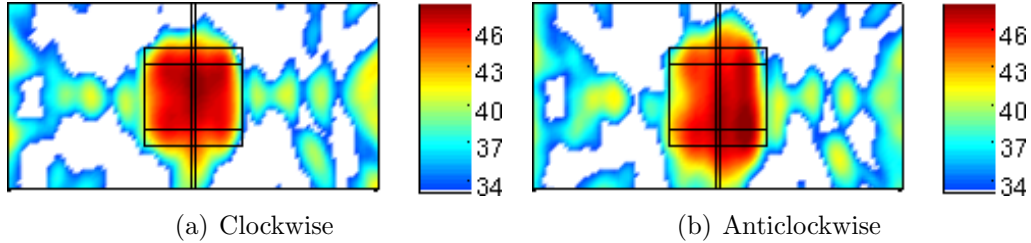
Figure 5.17: Beamforming plots, showing the impact of rotation direction. (Plots at the 1/3rd octave band with centre frequency of 1600Hz for the 3-bladed rotor at TSR=5, Ω=12.0Hz and U_∞=6.6m/s with trips on the inner surfaces of the blades.)

cases which confirms that the source is not the result of any Doppler or source directivity effects.

As for the earlier cases, there is a slightly different behaviour at TSR=5. At this operating condition the location of the dominant source was found to be different, depending on which direction the rotor was spinning. In the anticlockwise case the strongest source was observed in the downstream half of the rotor, while in the clockwise case the source strength was approximately uniform over the whole swept area. This difference is consistent with the trends observed when the blades were untripped, as shown in figure 5.14.

The downstream source that is observed once the laminar boundary layer noise was eliminated is thought to be due to blade-wake interaction. The amplitude of this source is found to peak at 53dB at TSR=3, and then decreases to around 47dB for TSR=4-5. One possible explanation for this peak in the strength of this source is that, while the intensity of the wake increases as TSR increases, the downstream velocity simultaneously decreases. The increase of the blade velocity relative to the wind speed at high TSR also means that the change in angle of attack experienced by the blades, as they pass through the wake, is much smaller at high TSR.

5.3.4 Sector Beamforming

By using the synchronised sampling mode of the data acquisition system it was possible to break the time series data into individual sectors of the blades' rotation, as described in section 4.4.2. There were two significant advantages to this method, the first of which is that it allowed the noise sources to be more definitively located since the blade positions were known in each of the sector plots. Secondly, the time averaged plots were often dominated by a source that was being radiated from only a small fraction of the blades' rotation. By isolating

these sectors it was possible to observe some of the quieter sources in the sectors where the dominant source in the time averaged plots was not radiating.

A sequence of six 22.5° narrowband sector beamforming plots for the 3-bladed rotor operating at TSR=3 are shown in figure 5.18(a) with the blade locations indicated alongside. These plots show that the sector beamforming method is clearly capable of locating the blade as it moves around the hub and indicate that there is a strong source in the downstream half of the rotor as is expected for the TSR=3 case. A strong source is also identified in the final sector when the blade reaches the most upstream location. This is also in agreement with the existing data which suggest that dynamic stall will occur in this region and should be a strong radiator of sound. Sector plots of the various TSR and solidity cases similarly confirmed the general conclusions drawn from the time average beamforming plots.

One other interesting feature that was noticed in the quieter sectors of the rotation was the influence of the blade spokes on the sound radiation. This is particularly evident in the upstream half of the rotor for the cases with tripped boundary layers, shown in figure 5.18(b). This noise could either be the result of vortex shedding from the spokes or due to the scattering at the trailing edge of the turbulence in the wake of the spokes. Either way, it could be at least partially mitigated by inserting an aerodynamic fairing around the spoke.

5.4 Summary and Conclusions

The key results from the analysis of the experimental data are summarised below:

1. The model-scale results are qualitatively similar to full-scale results, suggesting that the conclusions drawn from the experiments can be extended to a typical small-scale, power generating VAWT rotor.

2. At TSR=1 the noise is predominantly radiated from the upstream half and is understood to be the result of the unsteady blade loading generated during dynamic stall. The extent of this source is reduced as TSR increases. This source is also reduced by increasing solidity since the higher induction factors reduce the angles of attack on the blades in the upstream half of the rotor, thereby decreasing the extent of dynamic stall.

3. Laminar boundary layer tonal noise is a significant source, but can be eliminated by tripping the flow on the inner surfaces of the blades. This can result in significant noise reductions of up to 10dB at the relevant frequencies. This noise was found to be radiated as the blades are travelling in the upwind direction.

(a) No trip (b) Inner surface tripped

Figure 5.18: Narrowband sector beamforming plots centred on 1530Hz for the 3-bladed rotor operating at TSR=3 - flow is from left to right (narrowband frequency resolution is 192Hz).

4. At TSR greater than two the dominant source is in the downstream half of the rotor. This source is understood to be due to the downstream blades passing through the wake shed by the upstream half of the rotor. At even higher TSR the noise is radiated approximately uniformly from all locations and Doppler amplification of the noise from the approaching blades is observed.

5. Inflow turbulence disrupts the harmonic content of the sound-field, particularly at low TSR. At higher TSR the blade relative velocity is dominated by the blade velocity rather than the wind velocity, so the inflow turbulence has very little effect on the radiated sound.

6. Sector beamforming identified a source in the upstream half of the rotation from the spokes. This could potentially be mitigated by installing aerodynamic fairings around the spokes.

Chapter 6

Aeroacoustic Models

Simulation of aeroacoustic sources is a significant computational challenge. To directly model the small scale, high frequency pressure fluctuations that result in sound propagation is too computationally expensive in all but the most specialised cases. A more useful approach is to utilise analytical or empirical models of sound generation and propagation in combination with an estimate of the aerodynamic excitation.

A model using the equations derived by Lowson [1965] for the sound radiated by a moving point force was implemented, and was used to investigate some of the characteristics of the VAWT sound field. This model only predicted the harmonic component of the sound field, and was further limited by the availability of sufficiently high resolution blade loading data. This motivated the investigation of a method for determining the blade loading harmonics from the sound field.

As with many aeroacoustic problems, the limitations imposed by the lack of sufficiently high resolution input data, along with the significance of stochastic contributions, meant that an empirical approach was found to be more useful for making predictions of the noise from a VAWT rotor. Such a model was implemented using the spectral scaling laws derived by Brooks, Pope, and Marcolini [1989], as described in section 6.3. This model was still heavily dependent on certain inputs; consequently a parametric study was undertaken to establish the sensitivity of the output to these variables.

6.1   Harmonic Modelling

Experimental measurements had indicated that there was a strong harmonic component to the sound field, implying that one of the source mechanisms was periodic and deterministic. Harmonic noise models were therefore investigated to assess their ability to predict the noise from a VAWT rotor.

6.1.1 Lowson and Ollerhead Rotating Harmonics

Lowson and Ollerhead [1969] derived a model for estimating the far-field sound radiated by the unsteady loading on helicopter rotor blades. The source model used was the expression for the far-field sound radiated by a moving point force derived by [Lowson, 1965], and reproduced in equation 6.1.

$$\rho - \rho_0 = \left[\frac{x_i - y_i}{4\pi a_0^2 r^2 (1 - M_r)^2} \left\{ \frac{\partial F_i}{\partial t} - \frac{F_i}{1 - M_r} \frac{\partial M_r}{\partial t} \right\} \right]_{ret} \tag{6.1}$$

For a rotating source, such as the blade loads on a helicopter or VAWT, this loading can be represented using a Fourier series. In the derivation by Lowson and Ollerhead [1969] the force is defined in cylindrical polar coordinates and is split into thrust, drag and radial components as defined in equations 6.2, 6.3 and 6.4 (see also figure 6.1).

$$F_T(\tau) = a_{0T} + \sum_{\lambda=1}^{\infty} a_{\lambda T} \cos(\Omega\tau) + b_{\lambda T} \sin(\Omega\tau) \qquad \text{Thrust Component} \tag{6.2}$$

$$F_D(\tau) = a_{0D} + \sum_{\lambda=1}^{\infty} a_{\lambda D} \cos(\Omega\tau) + b_{\lambda D} \sin(\Omega\tau) \qquad \text{Drag Component} \tag{6.3}$$

$$F_C(\tau) = a_{0C} + \sum_{\lambda=1}^{\infty} a_{\lambda C} \cos(\Omega\tau) + b_{\lambda C} \sin(\Omega\tau) \qquad \text{Radial Component} \tag{6.4}$$

The Fourier series definitions are then inserted into the source expression, and the equation is integrated to determine its complex Fourier coefficients, c_n, as defined in equation 6.5.

$$\rho - \rho_0 = f(r_1, \phi, t) = \sum_{n=-\Omega}^{\Omega} c_n(r_1, \phi) e^{in\Omega t} \tag{6.5}$$

The result is the expression, given in equation 6.6, for the complex amplitude of the nth sound harmonic, c_n, as a result of summation over all of the blade loading harmonics between $\lambda = \pm\infty$.

$$c_n = \sum_{\lambda=0}^{\infty} \frac{i^{-(n-\lambda)}}{4\pi} \left\{ \frac{n\Omega x}{a_0 r_1^2} \left\{ +ia_{\lambda T}(J_{n-\lambda} + (-1)^\lambda J_{n+\lambda}) - b_{\lambda T}(J_{n-\lambda} - (-1)^\lambda J_{n+\lambda}) \right\} \right.$$

$$- \left\{ \frac{ia_{\lambda D}}{Rr_1} \left((n-\lambda)J_{n-\lambda} + (-1)^\lambda(n+\lambda)J_{n+\lambda} \right) - \frac{b_{\lambda D}}{Rr_1} \left((n-\lambda)J_{n-\lambda} - (-1)^\lambda(n+\lambda)J_{n+\lambda} \right) \right\}$$

$$\left. + \frac{n\Omega Y}{a_0 r_1^2} \left\{ a_{\lambda C}(J'_{n-\lambda} + (-1)^\lambda J'_{n+\lambda}) + b_{\lambda C}(J'_{n-\lambda} - (-1)^\lambda J'_{n+\lambda}) \right\} \right\} \tag{6.6}$$
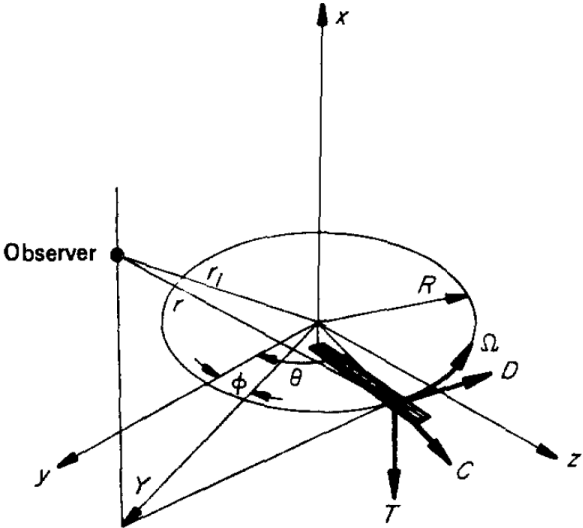
Figure 6.1: Schematic of the geometric parameters used by Lowson and Ollerhead [1969] in their rotating harmonics model

The integration utilised a Bessel function identity, and in the expression above J_n is the Bessel function of order n and J'_n is the first differential of the Bessel function. The argument of all of the Bessel functions is nMy/r_1.

This method can easily be adapted to a multiple blade scenario by substituting $n = mB$ where B is the number of blades. This method works due to the fact that the harmonics which are not multiples of B will cancel out, while those that are multiples of B will add. In this case the blade loading harmonics must be specified as the values for the whole rotor, which are B times the values for the individual blades. This model was validated against experimental data for helicopter noise and was shown to make good predictions of the harmonic noise from the rotor blades [Lowson and Ollerhead, 1969].

6.1.2   New Rotating Harmonic Model

The expression derived by Lowson and Ollerhead [1969] appears very complicated, and it was felt that the equation could be presented in a form that was more convenient for modelling a VAWT, rather than a helicopter. The starting point for the re-derivation of the rotating harmonic model was the same as that used by Lowson and Ollerhead [1969], but the Fourier series definitions of the forces were left in Cartesian coordinates. The same approach of integrating to find the Fourier coefficients of the sound field was then adopted, and it was found that a number of terms cancelled to leave a much more simple final result. The full derivation is presented in appendix A, but the key result is repeated here in

equation 6.7.

$$c_n = \sum_{\lambda=-\infty}^{\infty} 2\pi \frac{e^{-in\Omega\frac{r_1}{a_0}+i(\lambda-n)\phi}}{8\pi^2 a_0^3 r_1^2} c_{\lambda i} x_i \Omega n i^{(\lambda-n+1)} J_{(\lambda-n)} \left(\frac{nY M_B}{r_1} \right) \qquad (6.7)$$

In the above expression, all of the geometric parameters are as defined in figure 6.1 and the subscripted i denotes the Einstein summation convention over the three Cartesian coordinates. Comparison of the two models was undertaken as described in section 6.1.4, and it was shown that, despite appearing very different, both expressions produced nearly identical results.

Like equation 6.6, this solution only applies in the far-field. What constitutes the far-field is not always straightforward to determine, since the point at which the far-field terms become dominant depends on the frequency at which the force is fluctuating. It should also be noted that, in the wind tunnel experiments, the array microphones are sometimes less than 0.4m from the source, which almost certainly places them within the near-field. These far-field harmonic expressions are therefore not suitable for modelling the sound radiated from the VAWT model to the array microphones. A more general calculation, which includes the near-field contribution, is described in the next section. The impact and extent of the near-field terms is examined in section 6.1.5.

6.1.3 Time Domain Modelling

The result originally derived by Lowson [1965] for the sound field from a moving point force includes exact expressions for both the near-field (equation 2.5) and far-field (equation 2.6) sound. By solving these equations numerically in the time domain it was possible to derive a relationship between the blade loading harmonics and the radiated sound field at any point in space, whether near-field or far-field.

These equations for the complete sound field were solved in Matlab and a discrete Fourier transform was performed on the output, such that the predicted sound harmonics could be compared with the results from the analytical rotating harmonic methods. An outline of how the Matlab program operated is given below.

1. The normal and tangential forces on the blades around one revolution are specified using a Fourier series approximation, before being converted into the Cartesian coordinate system. The Fourier series representation allows the exact derivative of the force to be calculated.

2. The parameters relating the source and the observer at each point for one blade revolution are calculated. These include the distance between the

source and observer, and the angle from the blade to the observer. The acceleration term $\partial M_r/\partial t$ is difficult to compute analytically without using far-field assumptions, so was calculated using a second order central difference relation.

3. The sound reception time is calculated for each value of source time.

4. The acoustic pressure fluctuations are calculated for each azimuthal blade location using Lowson's equation.

5. In order to allow the sound waves from multiple sources to be superimposed, an interpolation method is used to determine the received sound wave at fixed points in receiver time. This has no effect on the actual pressure signal.

This process could be repeated for multiple source locations along the blade span, or for multiple blades, with the resulting sound fields being superimposed to give the overall field. One case of particular interest was the multiple blade scenario. This case was modelled by calculating the sound propagation from a single blade, and rotating the output by $360/B$ (where B is the number of blades) then summing the results.

6.1.4 Model Validation

The Lowson and Ollerhead model, the newly derived rotating harmonic model, and the time-domain model were all run with identical input data, and the outputs were compared for a number of cases (see list of test cases in table 6.1). Some simple test cases with a single blade loading harmonic were initially simulated in order to confirm that the three models all predicted the same sound spectra for a given source frequency. Figures 6.2(a), 6.2(b) and 6.2(c) show the predicted spectra for cases 1-3, where the observer is located 10m from the hub, and is therefore considered to be in the far-field. It can be seen that there is good agreement between the three methods in this condition. The two analytical models only compute harmonics of the blade passage frequency, whereas the numerical model computes all harmonics of the angular velocity. The non-zero values returned by the numerical model at harmonics which are not multiples of the blade passage frequency were thought to be due to the small errors introduced by the numerical computation.

The difference between the two analytical harmonic models, was thought to be due to the slightly different application of the far-field assumptions in the derivation of the two models. The numerical model did not utilise any far-field

Parameter	Case1	Case2	Case3
x_0 (m)	[10,0,0]	[10,0,0]	[10,0,0]
Ω (rad/s)	75	75	75
F_N (N)	$10sin(5\Omega t)$	0	$10sin(20\Omega t)$
F_T (N)	0	$10sin(10\Omega t)$	$10cos(5\Omega t)$
	Case4	**Case5**	**Case6**
x_0 (m)	[10,0,0]	[1,0,0]	[0.6,0,0]
Ω (rad/s)	75	75	75
F_N (N)	$10sin(3\Omega t)$	$10sin(3\Omega t)$	$10sin(3\Omega t)$
F_T (N)	0	0	0
	Case7	**Case8**	**Case9**
x_0 (m)	[0.6,0,0]	[0.6,0,0]	[0.6,0,0]
Ω (rad/s)	75	75	75
F_N (N)	$10sin(\Omega t)$	$10sin(10\Omega t)$	$10sin(20\Omega t)$
F_T (N)	0	0	0

Table 6.1: Details of rotating harmonic test cases run. For all cases the rotor radius was 0.265m and the number of blades was 3.

assumptions, so it is perhaps not surprising that the predicted spectra were different from the two analytical models. The relatively good agreement of the two new models with the earlier method allowed them to be used to investigate some of the potential characteristics of the sound radiated by a VAWT rotor.

Cases 4-6 investigated the impact of moving the observer closer to the source (see figures 6.2(d), 6.2(e) and 6.2(f)). As expected the numerical model, which includes the near-field components, increasingly diverges from the far-field-only models as the observer approached the rotor. The differential term in the expression for the far-field sound suggested however that, for higher blade loading harmonics, the far-field component could dominate the near-field component of the sound field even for close observer locations. Cases 7-9 investigated this behaviour by simulating increasingly high blade loading harmonics for an observer placed 0.6m from the rotor hub. The numerical model, which includes the near-field terms, predicted spectra much more similar to the far-field-only models for the simulations of high harmonics, thus qualitatively confirming this assumption.

The test cases with the observer located 0.6m from the rotor hub were chosen to represent the location of the closest microphone in the acoustic array. For this observer location the near-field terms were found to make a significant contribution to the sound field. In order to assess the extent of the impact of the
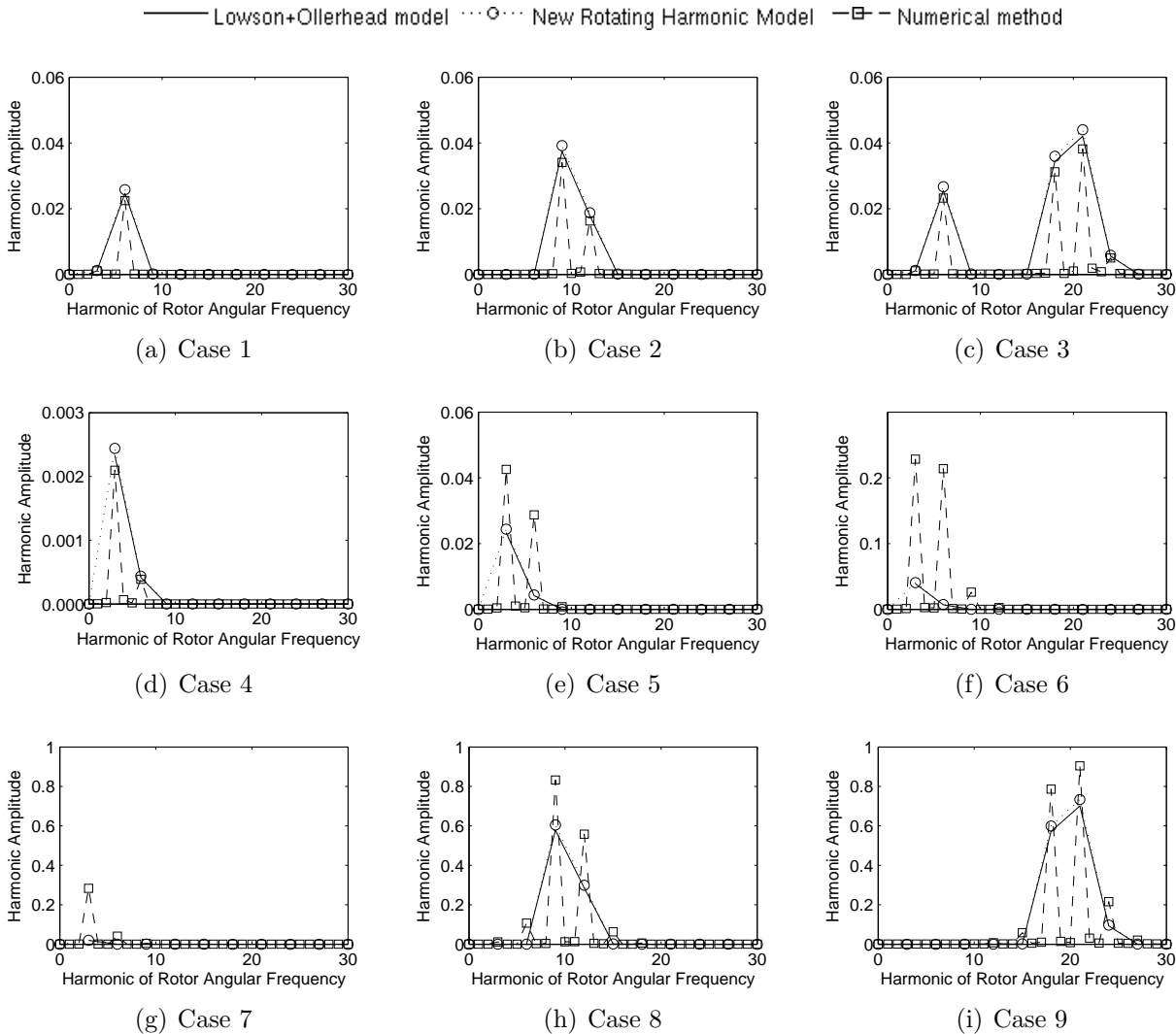
Figure 6.2: Spectra computed by the Lowson + Ollerhead model, the new rotating harmonic model and the numerical simulation for the nine test cases. Note that the spectra for the new rotating harmonic model and the Lowson + Ollerhead model are overlapping in all cases.

near-field terms on the array measurements presented in the previous chapter, a more detailed investigation of their contribution to the sound field was conducted using the numerical model.

6.1.5   Near-Field versus Far-Field

The numerical model computed the near- and far-field components of the sound field separately, using the expressions derived by Lowson [1965] (equations 2.5 and 2.6). This allowed the two components to be separated out and compared.
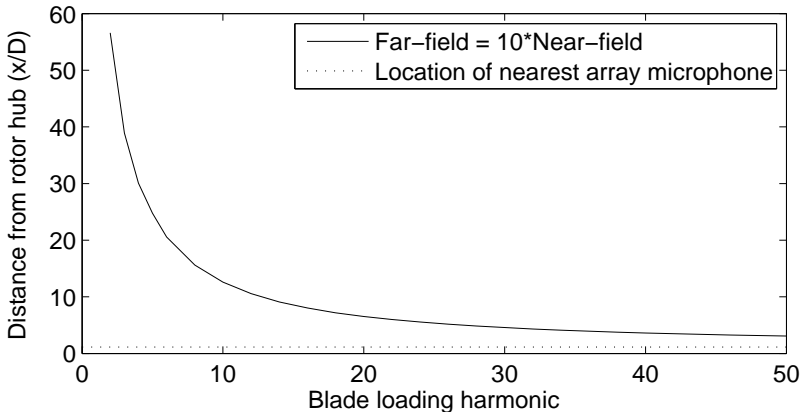
Figure 6.3: Plot of the distance from the rotor hub at which the RMS value of the near-field component is 10% of the far-field components of the sound field as a function of blade loading harmonic

A simulation was carried out to evaluate the change in the size of the region where the near-field terms made a significant contribution to the sound field, as a function of increasing blade loading frequency. Each blade loading harmonic was individually simulated for an observer directly upstream of the rotor and a simple iterative process was used to determine the location where the far-field signal's RMS amplitude was ten times greater than that of the near-field signal. The results of this calculation are presented in figure 6.3. For any observer location below the solid line it was deemed necessary to include the near-field terms in a model of the sound field in order to make accurately predictions. In figure 6.3 the dashed line is at 0.6m, which is the smallest distance between the rotor hub and an array microphone in the wind tunnel experiments. Even for the sound field radiated by the 50th blade loading harmonic, the RMS amplitude of the near-field signal is more than 10% of the RMS far-field signal at 0.6m from the hub. This demonstrates the importance of including the near-field terms in any model for predicting the noise from the wind tunnel experiments.

(a) Normal force profile

(b) Tangential force profile

(c)   Normal force Fourier series harmonics

(d)   Tangential force Fourier series harmonics
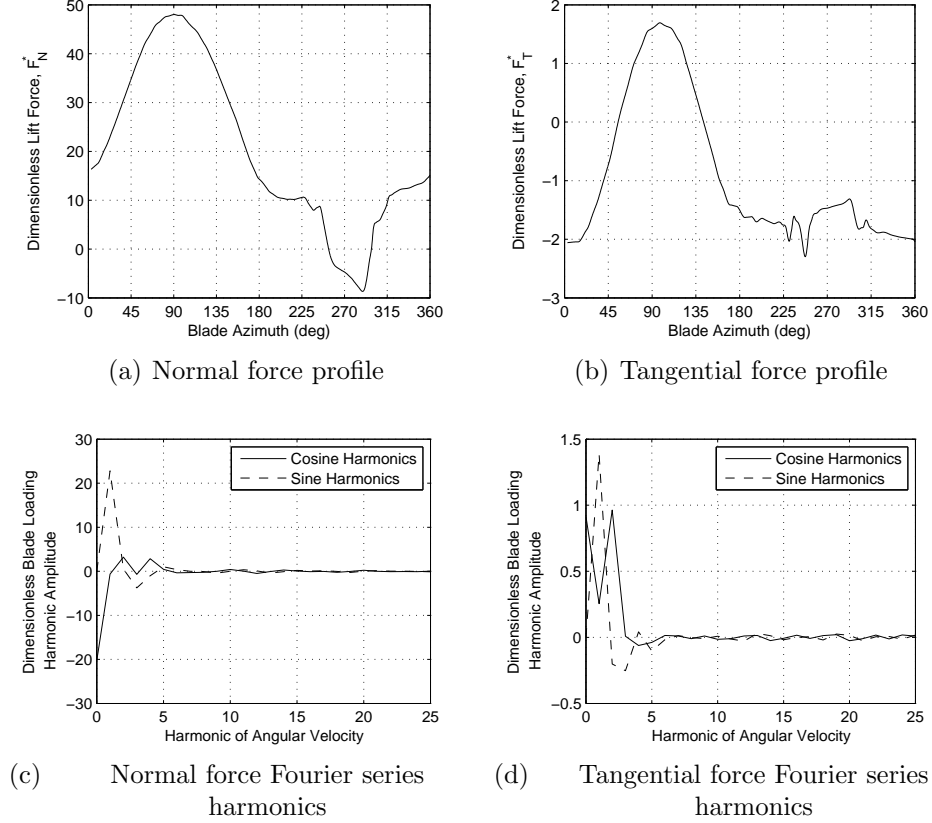
Figure 6.4: Normal and tangential non-dimensional blade loads computed by Scheurich [2011] using a vortex transport model, and the associated Fourier series harmonics.

A further test case was simulated using the blade loading data calculated by Scheurich [2011] for a VAWT operating at TSR=7.5. This blade loading profile and the associated Fourier series components of the normal and tangential forces are presented in figure 6.4. The blade forces are expressed as dimensionless, sectional lift coefficients, which are defined as follows:

$$F_N^* = \frac{F_N}{\frac{1}{2}\rho c U_\infty^2}$$
$$F_T^* = \frac{F_T}{\frac{1}{2}\rho c U_\infty^2}$$

The autopowers of the near- and far-field components of the sound radiated to the array microphone located 0.6m from the rotor hub were computed sepa-
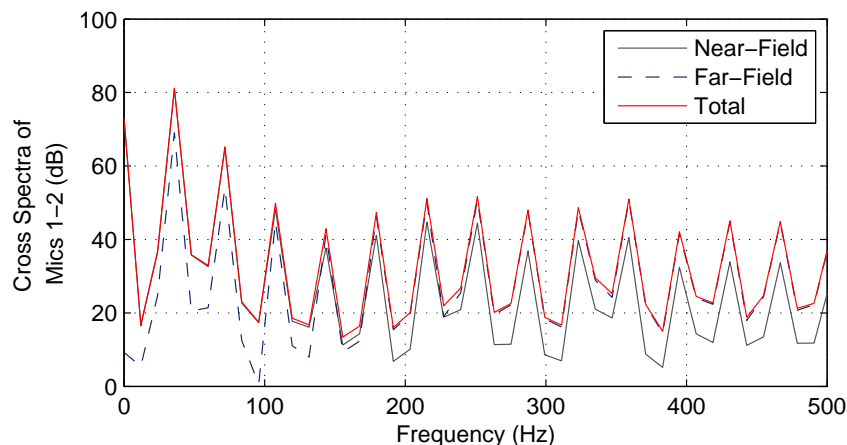
Figure 6.5: Plot of the near-field, far-field and total autopowers radiated to array microphone 1 by the simulated blade loading profile calculated by Scheurich [2011].

rately to assess their relative contribution to the sound field. The results of this calculation are plotted in figure 6.5.

This data partly confirms the result of the simulations presented in figure 6.3. The near-field terms are seen to dominate the shape of the total spectrum up to the 3rd harmonic of the blade passage frequency (9th harmonic of the angular velocity), and are seen to still be within 10dB of the far-field terms up to the 40th harmonic of the angular velocity (478Hz).

One further key result from this simulation is that the total spectrum always exceeds the spectra of its component parts, i.e. the near- and far-field contributions do not destructively interfere with each other. This result means that the spectra measured by the acoustic array represent an upper bound on the far-field contribution at this location.

6.1.6 Harmonic Sound Radiation

One further result that can be derived from this simple model is the relative contribution of the various blade loading harmonics to the radiated sound. The differential term in the expression for the far-field sound means that a high blade loading harmonic will contribute more to the sound field than a lower harmonic of the same amplitude. To account for this, the simulated blade loading harmonic values (shown in figures 6.4(c) and 6.4(d)) were scaled by their respective frequencies. This gave an estimate of which blade loading harmonics were most significant from the point of view of sound radiation. The results of this calculation are plotted in figure 6.6.
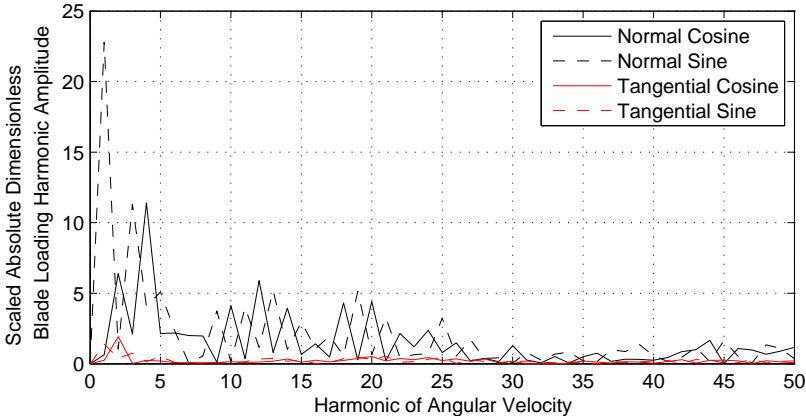
Figure 6.6: Plot showing blade loading harmonic amplitudes, scaled by the harmonic of the angular velocity.

This plot indicates that, from the point of view of noise radiation, the higher blade loading harmonics contribute more to the sound field than is initially apparent. This is consistent with the results of Wright [1971] who found that fluctuating forces weaker than one-thousandth of the steady loading component can dominate the radiation due to the steady component (see section 2.4.3). This highlights the necessity of high resolution blade loading data for accurate prediction of the radiated harmonic noise.

This scaling process shows that the higher harmonics are more important than they initially appear, but they are still very low above the 30th harmonic of the angular velocity; this corresponds to approximately 130Hz on the full-scale rotor. In the investigation of the experimental results (section 5.2.1.4) it was shown that the harmonic sound needs to be significantly louder than the broadband component to dominate the spectra. This analysis therefore suggests that the harmonic component of the sound radiated by the full-scale rotor is unlikely to be significant above around 100Hz. Given the low sensitivity of the human ear at such low frequencies, the stochastic component of the sound field is likely to dominate the perceived sound. This was the motivation for investigating the broadband noise model presented in section 6.3.

Since the harmonic models were of limited use for making predictions of the sound, an alternative use was investigated to see whether it was possible to determine the blade loading harmonics from the harmonic component of the sound field.

6.2   Inverse Harmonic Method

The sound propagation model gave a linear relationship between the blade loading harmonics and the radiated sound harmonics. Given that such a linear relationship between the two exists, it should be possible to estimate the former from the latter. This represented an interesting opportunity for determining the blade loads on a VAWT, which are otherwise very difficult to obtain.

6.2.1   Implementation

The first step was to compute the transfer functions that related the blade loading harmonics to the sound harmonics at the microphones. The acoustic pressures due to the sine and cosine components of both the normal and tangential blade force Fourier series were separately determined, giving four elements for each harmonic of the rotor angular frequency. The sound harmonics for each blade loading harmonic were then entered into the columns of a transfer matrix. This process was repeated for each of the microphones in the acoustic array.

The result is an overdetermined set of linear equations of the form:

$$\mathbf{Gc} = \mathbf{p} \tag{6.8}$$

where $\mathbf{G}$ is the transfer matrix, $\mathbf{c}$ are the blade loading harmonic amplitudes and $\mathbf{p}$ is a vector of the sound harmonics at each microphone location. This set of equations could be solved using a least squares method and, since the transfer matrix is not rank deficient, an exact solution would be obtained if there were no noise in the microphone signals. The transfer matrix is not very well conditioned, however, which makes the simple least squares method very sensitive to noise.

An alternative to the least squares method was to use a singular value decomposition of the transfer matrix. This method was potentially effective at dealing with noise as one could extract the dominant components by simply setting the small singular values to zero. This process of removing the small singular values can be thought of as improving the condition of the transfer matrix [Press et al., 1992]. The exact definition of what constitutes a 'small' singular value is flexible: setting a high threshold for 'small' values gave good noise rejection, but also gave less accurate absolute results. A lower threshold would do the opposite, hence there was a trade-off between noise rejection and accuracy.

Another potential method for solving the set of equations was to use a quadratic limited least squares program. This allowed limits to be set on the possible values of the objectives (the blade loading harmonic amplitudes), which meant that the solution could be constrained to only those cases that were physically reasonable. This method was implemented in Matlab using the convex optimisation package, CVX, developed by Stephen Boyd [Boyd and Vandenberghe, 2004].

A comparison of these three methods for solving the inverse problem is presented in the next section.

6.2.2 Testing

The numerical model of the rotating point force was used as described in section 6.1.3 to compute the sound spectra radiated from the model VAWT to the array microphones. The inverse model was then run to see if the blade loading harmonics could be calculated from the predicted microphone signals.

The blade loading profile computed by Scheurich [2011], and shown in figure 6.4, was used as the test case for assessing the performance of the three inverse solutions. In the absence of noise, all three models were shown to be able to exactly compute the blade loading harmonics from the simulated sound harmonics. To achieve this exact solution, no limits were placed on either the SVD or CVX methods.

A zero-mean, complex, Gaussian random noise signal with a standard deviation of one was then added to the simulated microphone spectra. The amplitude of the noise was scaled by a percentage of the maximum harmonic amplitude radiated to any of the array microphones. This same random noise component was added to all harmonics of all the microphone signals, which was equivalent to adding a uniform amplitude white noise signal to all of the microphone signals in the time domain. The error in the estimation of the blade loading harmonics for each of the three solution methods was computed for noise amplitudes between 0% and 10% of the maximum harmonic amplitude, and the results are plotted in figure 6.7.

The absolute error in the solution for the blade harmonics was estimated by computing the L2 norm of the difference between the estimated and actual blade loading harmonics. This difference was then scaled by the magnitude of the vector of blade loading harmonics. A second error value that accounted for relative error was found by computing the L2 norm of the vector of relative errors for each harmonic. For both of these methods each case was simulated ten times with a different random error added. The mean error was then recorded along with the maximum and minimum error values.

It is important to note that, since the blade loading harmonics must be real, the least squares and SVD solutions needed to be constrained to give real solutions. This was done by separating out the real and imaginary components of both the transfer matrix and the microphone spectra and then stacking them on top of one another. The least squares solution in Matlab then became:

```
c = [real(G); imag(G)] \ [real(p); imag(p)];
```

(a) Absolute error   (b) Relative error
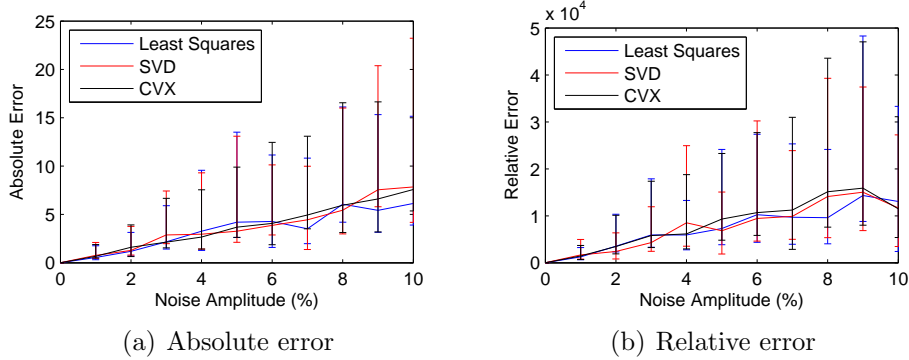
Figure 6.7: Plots of the relative and absolute error for each of the inverse
solution methods as a function of the amount of random noise added.

For the SVD solution, the transfer matrix G was split into real and imaginary
components, as shown above, before the decomposition was performed. The
solution then proceeded in the normal way, with the pressure spectra also split
into their real and imaginary components.

As expected, all three methods return similar solutions when no limits are
imposed on the output. The SVD and CVX solutions can potentially be improved
by respectively removing some of the smaller singular values or by imposing limits
on the output. The CVX method is particularly attractive in this regard since the
limits on the solution can be determined from the physics of VAWT operation.
The SVD solution could potentially be improved by setting the singular values
below a certain threshold to zero. The optimal level for this threshold is very
difficult to determine however, and would be dependent on the amplitude of the
noise added to the signal. Due to its much more simple application, only the
CVX solution was carried forward for further investigation.

6.2.3 Blade Loading Harmonic Limits

The CVX method used to generate the data in figure 6.7 was implemented with-
out any limits imposed on the possible values of the estimated blade loading
harmonics. The choice of suitable limits was not obvious, but, since both the
normal and tangential loading profiles were dominated by a strong sine wave
shape, it was decided to constrain the cosine harmonics. It should be noted that
the sine wave shape of the blade loading profiles is fundamentally determined by
the aerodynamics of a VAWT rotor.

In order to ensure that the blade loading profile had a sine wave shape, a limit
was imposed that forced the sum of the cosine harmonics to zero. The zero-th
cosine harmonic was omitted from this limit to allow the loading profiles to have a

(a) Absolute error
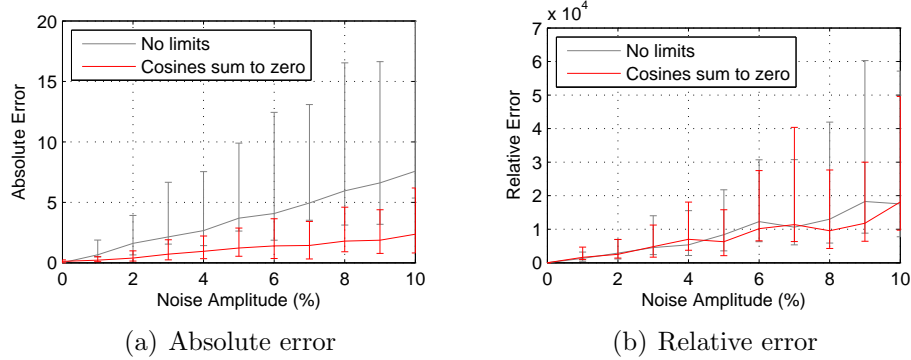
(b) Relative error

Figure 6.8: Error in the CVX solution with and without limits imposed.

DC offset. A comparison of the absolute and relative errors for the CVX method with and without limits are presented in figure 6.8.

Adding these limits to the CVX method produced a significant reduction in the magnitude of the absolute error, while the relative error remained approximately the same. The implication is that the absolute error is dominated by small relative errors in large amplitude harmonics, and the relative error is dominated by small absolute errors in low amplitude harmonics. Despite the fact that the relative error is not improved by these limits, the reduction in the absolute error represents a worthwhile improvement in the solution.

6.2.4   Harmonic Sensitivity

Further investigation of the error in the CVX solution was carried out to determine the ability of the method to determine individual harmonics. The test case described above was carried out with a 10% noise signal added to the microphone spectra and the absolute and relative error in the estimation of each harmonic was calculated. The simulation was repeated 50 times and the mean error values were computed. The results of these calculations are presented in figure 6.9.

The absolute error data plotted in figure 6.9(a) shows that there is significantly more error in the estimation of the low frequency harmonics than the higher frequency harmonics. The relative error in the estimation of the low frequency harmonics however, was small. Further investigation found that the spikes observed in the relative error data were due to single simulations giving very high relative errors that were still evident after many averages. The spikes were seen to persist when the simulation was repeated, but were observed at different blade loading harmonics, demonstrating that there was no systematic error in the estimation of specific blade loading harmonics.

(a) Absolute error　　　　　　　　(b) Relative error
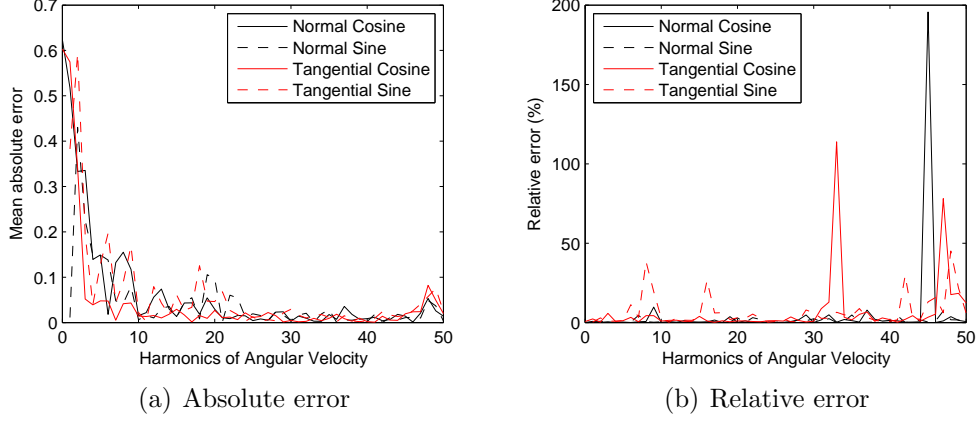
Figure 6.9: Error in the estimation of each blade loading harmonic.

6.2.5　Singular Value Decomposition of the Transfer Matrix

Further investigation of the sensitivity of the model to different blade loading harmonics was carried out via the singular value decomposition of the transfer matrix, which provides its range and the null space. The relative magnitude of the biggest and smallest singular values is also a useful indicator of the 'condition' of the matrix. If the inverse of this ratio is close to the machine precision, then the method will be susceptible to computational errors.

For the acoustic transfer matrices calculated none of the singular values was equal to zero, implying that the matrices had no null space. In addition the inverse of the ratio of the biggest and smallest singular values was 10^{-6}, which is much greater than the resolution of a double precision floating point number (10^{-12}). This confirmed that the inverse method should be able to identify any combination of blade loading harmonics if there were no errors in either the measurements or the method, as was seen in the test cases shown in figure 6.7.

$$\mathbf{G} = \mathbf{UWV^H} \tag{6.9}$$

$$\sum_k G_{jk}V_{ki} = w_i U_{ji} \tag{6.10}$$

Singular value decomposition breaks the transfer matrix into the components shown in equation 6.9. When this is written in the form of equation 6.10 it can be seen that the ith column of the V matrix multiplied by the transfer matrix is equal to the ith column of U matrix scaled by the ith singular value. Therefore

(a) Largest singular value   (b) Smallest singular value
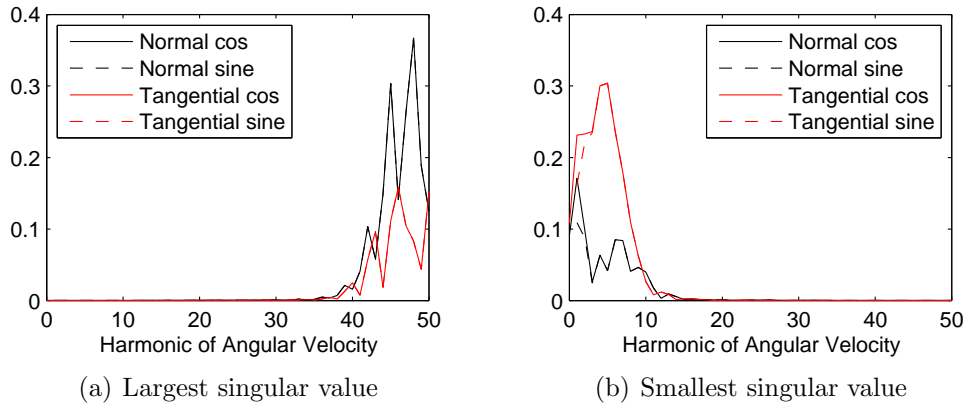
Figure 6.10: Plot showing blade loading harmonic vectors associated with the largest and smallest singular values

any column vector of V which is associated with a small singular value only produces a small output. The vectors associated with the largest singular values were found to include only the higher blade loading harmonics. At the same time the vectors associated with the smallest singular values only contained the lower blade loading harmonics (see figure 6.10). This is equivalent to the conclusions of Wright [1971], who noted that a high blade loading harmonic will contribute much more to the sound field than a low frequency harmonic of the same amplitude.

The implication for the inverse model is that a small error in the low frequency data measured by the microphones would result in a large change in the estimated blade loading harmonics. For the simulated test cases, where a uniform amplitude noise signal was added to all frequencies, this could explain why the inverse method produced larger errors in the estimation of the low frequency harmonics.

The inverse method's low sensitivity at low frequencies was also thought to be a function of the geometry of the acoustic array. For long wavelength sound, the microphone spacing means that it is difficult to accurately determine the phase difference between the waves arriving at each microphone, particularly in the presence of random noise. By increasing the spacing between the microphones the phase difference will increase, making it easier to accurately resolve. In the beamforming process a larger array will enable better resolution of low frequency sources, and this same behaviour should result in the inverse method being better able to resolve low frequency harmonics.

To investigate this, the sound propagation model and the inverse model were run with all the microphone coordinates within the array plane doubled. A comparison of the mean absolute error in the estimation of each harmonic (for the TSR=7.5 test case with 10% noise added) for the baseline array and the
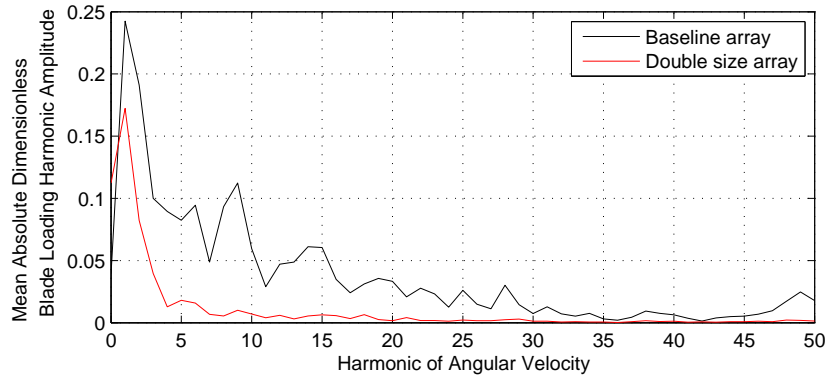
Figure 6.11: Comparison of the error in the estimation of blade loading
harmonics for the baseline array and the double size array.

double size array is shown in figure 6.11. For clarity of presentation the sine and
cosine components of both the normal and tangential forces have been averaged.
As expected, the increase in array size clearly improves the resolution of the low
frequency harmonics.

6.3 Empirical Noise Models

The empirical self-noise models developed by Brooks et al. [1989] are commonly
used for predicting the noise radiated by HAWTs, as discussed in chapter 2. Their
method provides a means of estimating the sound radiated by a moving aerofoil
without knowing the full detail of the flow.

Due to the unsteadiness of the aerodynamics on a VAWT rotor, it was uncertain whether this method would be capable of making realistic predictions of the
noise radiation. The first objective was therefore to establish whether this approach was able to generate sound spectra that were in agreement with measured
spectra.

The Brooks, Pope and Marcolini (BPM) scaling laws were implemented in
Matlab along with the turbulence inflow model developed by Lowson [1992], which
itself is based on the results of Amiet [1975]. For this initial assessment of the
method, the blade velocities and angles of attack were derived from a simple model
of a VAWT rotor assuming a uniform inflow. The boundary layer parameters were
then estimated from the equations specified by Brooks et al. [1989, pp.9-14]. A
test case was required for comparison, but, since all of the scaling laws are for
the far-field, the wind tunnel data were not suitable. As such the 1/3rd octave
spectra from the QR5 rotor were used.
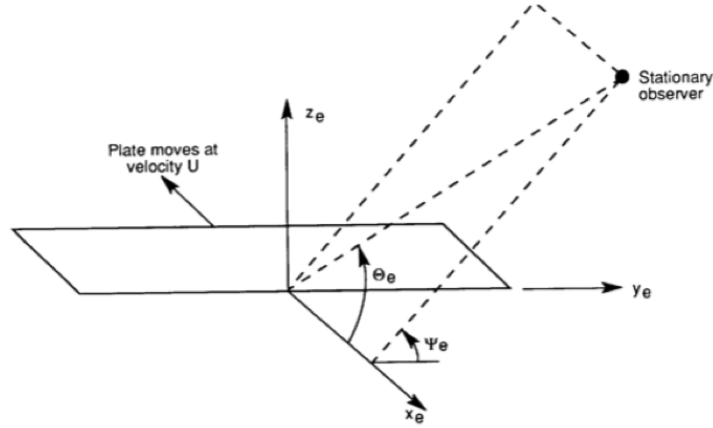
Figure 6.12: Repeat of schematic illustrating the angles required for calculating the trailing edge noise directivity

6.3.1 Coordinate and Doppler Corrections

Correctly computing the time averaged spectra radiated to an observer by a rotating blade using the BPM spectral scaling laws requires care. The methods for determining the transformations are clearly described in Sinayoko et al. [2013] and a summary of the key points is given here.

The BPM results are all derived relative to the source at its emission position, $\mathbf{x_e}$, which means that the observer location, $\mathbf{x_0}$, must first be specified in the blade coordinate system, shown in figure 6.12. The next task is to find the distance from the retarded source location to the observer, r_e. This is related to the time taken for the sound to propagate to the observer, T_e, by $r_e = c_0 T_e$. In order to account for the effect of the mean flow, this distance is actually calculated as being the distance from the convected source position, $\mathbf{x_c}$, to the observer: $|\mathbf{x_0} - \mathbf{x_c}| = c_0 T_e$. The convected source position is the emission location convected at the free stream Mach number, $\mathbf{M_\infty}$, by a distance $\mathbf{x_c} - \mathbf{x_e} = \mathbf{M_\infty} c_0 T_e$. Combining these results gives the equation,

$$c_o T_e = |\mathbf{x_0} - \mathbf{x_e} - \mathbf{M_\infty} c_0 T_e| \tag{6.11}$$

Squaring this result and defining $\mathbf{x_0} - \mathbf{x_e} = \mathbf{R_0}$ gives a second order polynomial in $r_e \equiv c_o T_e$ which can be solved to give the result of equation 6.12. In this equation, Θ is defined as the angle between $\mathbf{M_\infty}$ and $\mathbf{R_0}$.

$$r_e = \frac{R_0 \left(-M_\infty \cos \Theta + \sqrt{1 - M_\infty^2 \sin^2 \Theta} \right)}{1 - M_\infty^2} \tag{6.12}$$

As the VAWT blade rotates, the spectrum it radiates to the observer changes. These spectra need to be summed together in order to compute an estimate of the overall sound spectrum. The spectrum radiated from the source to the observer will be Doppler shifted to either higher or lower frequencies if the source is moving towards or away from the observer. In addition, if the source spectra are summed over uniform intervals of 'source time', Sinayoko et al. [2013] showed that each spectrum needs to be scaled again by the Doppler factor. The resulting integral is given in equation 6.13, where the Doppler factor is as defined in equation 6.14.

$$SPL_{obs,tot}(\mathbf{x_0}, \omega) = \frac{1}{2\pi} \int_0^{2\pi} \left(\frac{\omega'}{\omega}\right)^2 SPL_{source}(r_e, \omega', \theta) d\theta \tag{6.13}$$

$$\frac{\omega}{\omega'} = 1 + \frac{\mathbf{M_B} \cdot \widehat{\mathbf{EO}}}{1 + (\mathbf{M_\infty} - \mathbf{M_B}) \cdot \widehat{\mathbf{EO}}} \tag{6.14}$$

In the expressions above θ is the blade azimuth, ω is the angular frequency and the terms in bold type are vector quantities. $\widehat{\mathbf{EO}}$ is the vector from the source emission location to the observer.

6.3.2 Initial Results

The empirical noise model was run to simulate the QR5 rotor operating at TSR=3.5 in a wind speed of 10m/s. The observer was placed 22.5m downstream of the hub, which was the location of the microphone in the QR5 noise tests. The swept blades of the QR5 rotor were modelled using vertical aerofoils with a span equal to the vertical height of the QR5 rotor.

Parameter	Value
Blade Span	5m
Rotor Diameter	3m
Blade Chord	175mm
Blade Thickness	30mm
Trailing Edge Thickness	1mm
Wind Speed	10m/s
TSR	3.5
Turbulence Length Scale	100mm
Turbulence Intensity	10%

Table 6.2: Empirical model input parameters used to simulate the noise radiated by the QR5 rotor.

Most of the input parameters were fixed by the operating condition and the geometry (see table 6.2), but the turbulence data had to be estimated. It should be noted that, in the case of a VAWT rotor, the turbulence data are not necessarily the atmospheric parameters, since the input conditions need to somehow account for the turbulence shed by the upstream blades into the downstream half of the rotor. In the simulations, the turbulence parameters were adjusted to achieve a good match between the measured and predicted spectra, which resulted in the values for the turbulence length scale and intensity specified in the table of input parameters.
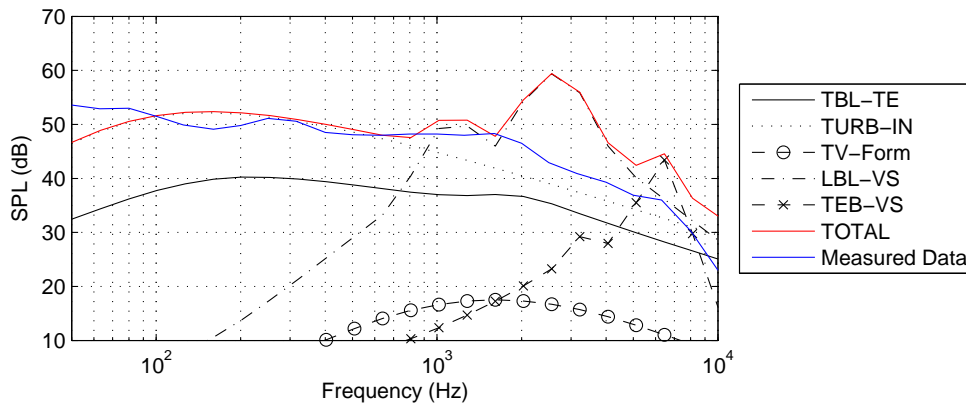
Figure 6.13: Comparison of the measured spectra with the spectra estimated from the empirical noise models. (TBL-TE = Turbulent boundary layer - trailing edge noise, TURB-IN = Turbulent inflow noise, TV-Form = Tip vortex formation noise, LBL-VS = Laminar boundary layer - vortex shedding noise, TEB-VS = Trailing edge bluntness - vortex shedding noise)

The predicted spectra for each of the self-noise sources, together with the total simulated and measured spectra, are plotted in figure 6.13. Below 1kHz there is a relatively good agreement between the measured and predicted spectra. It should be noted that the predicted spectrum in this region is dominated by turbulent inflow noise and this source is the one affected by tuning the turbulence parameters.

The predicted spectrum is dominated by laminar boundary layer (LBL) noise above 1kHz and is substantially different from the measured spectrum. The measured spectrum does deviate from the turbulent inflow noise in this region however, and approximately follows the first of the two peaks in the predicted LBL noise spectrum at around 1050Hz. The overestimation of the noise from LBL noise is possibly because this simple model assumes that the flow is steady and remains attached and laminar on the pressure surface around the entire revolution of the blade. The effect of blade-wake interactions and dynamic stall make this

(a) Vary length scale - Intensity = 10%

(b) Vary intensity - Length scale = 0.1m
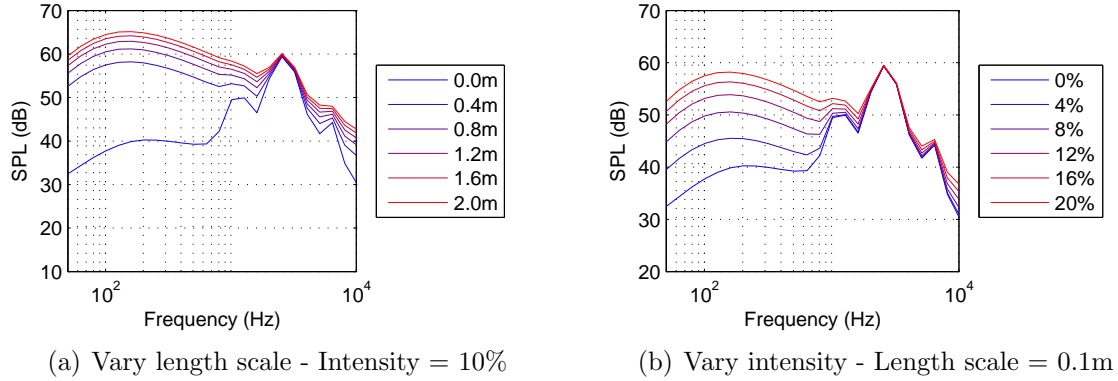
Figure 6.14: Parameter investigations of the impact of turbulence intensity and length scale on the spectra predicted by the BPM model.

extremely unlikely in practice, so it is perhaps not surprising that the LBL noise estimate is too high.

As a proof of concept this comparison was encouraging, as it appeared to be possible to use the simple scaling laws to predict the spectra with a reasonable degree of accuracy. In order to assess the robustness of these predictions a parametric study of the unknown turbulence input variables was carried out as described in section 6.3.3. In addition, certain details of the noise source mechanisms had been established from the experimental measurements and this information could be incorporated into the BPM model. The way in which this was done, and its impact on the noise predictions are described in section 6.3.4.

6.3.3 Turbulence Parameter Investigation

The preliminary investigation had shown that it was possible to obtain good agreement between the measured and predicted spectra, provided that the turbulence length scale and intensity were deliberately chosen to achieve this. In order to assess the impact of varying the turbulence statistics, the values of the turbulence inflow and length scale were varied and the predicted spectra were compared.

First, the turbulence length scale was varied from 0.0m to 2.0m in steps of 0.4m at a constant turbulence intensity of 10%. The turbulence intensity was then varied between 0% and 20% in steps of 4% for a constant length scale of 0.1m. All of the other model input parameters were as specified in table 6.2. The output data from these two simulations are presented in figure 6.14.

From these two plots it is clear that the choice of turbulence parameters has a significant effect on the amplitude of the spectra predicted by the BPM
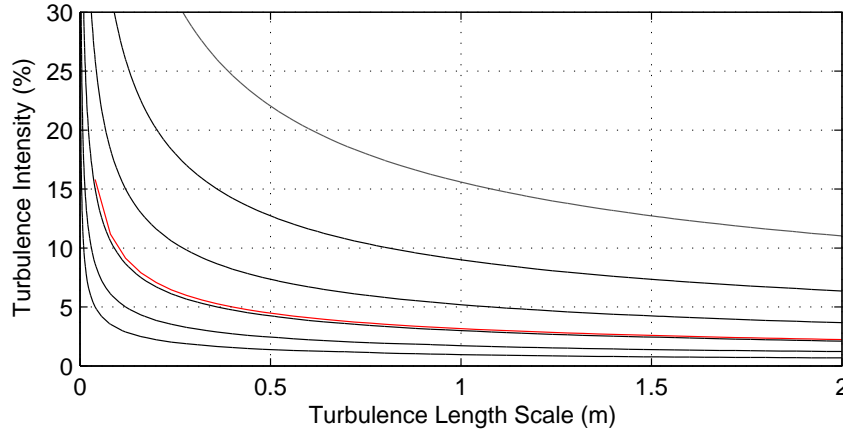
Figure 6.15: Contours of turbulence parameters that produce the same spectral level. The red curve indicates the levels adopted in the initial simulation.

model. Another interesting result is that there is a range of pairs of turbulence parameters that can produce any given spectral level. These sets of parameters can be determined from the spectral scaling function, where the amplitude is proportional to $Intensity^2 \times Lengthscale$. A contour plot showing the locii of points that give a constant turbulence inflow level is shown in figure 6.15, where the red curve indicates the level adopted in the initial simulation.

Given the data plotted in figures 6.14 and 6.15, it is worth considering what can be learnt from the range of possible values that were identified as giving the best fit with the measured spectra. Of particular interest is whether the turbulence inflow conditions are consistent with the expected levels of atmospheric turbulence, or whether the turbulence inflow noise is due to the VAWT interacting with its own wake.

McIntosh [2009] investigated the unsteady wind conditions that a VAWT might expect to encounter when installed in a typical urban environment. Even in what he describes as the 'worst case' (shortest gust length), the turbulence length scale at a hub height of 15m was predicted to be of the order of 50m[1]. Since this is much greater than the dimensions of the VAWT rotor, he found that the flow can be treated as being quasi-steady.

In the documentation accompanying the measurements of the noise from the full-scale rotor, the site around the turbine was described as being "flat and predominantly grass, but with a metalled track passing close by" [Dyne, 2007]. In these flat surroundings it might therefore be expected that the inflow turbulence during these measurements was consistent with the flow being treated as quasi-

---

[1]This length scale was derived from the Kaimal distribution for the wind power spectrum [Kaimal et al., 1972], assuming a roughness height of 1m and a mean wind speed of 4.2m/s.
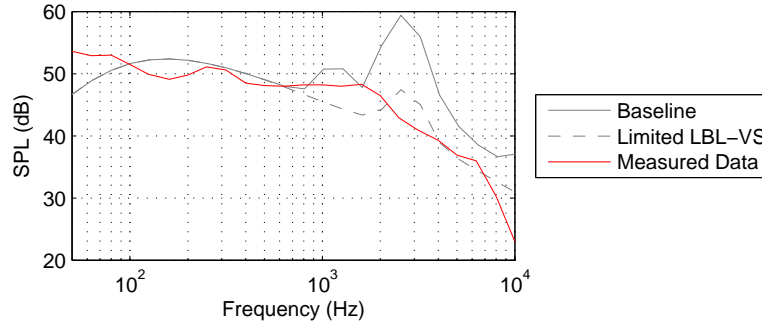
Figure 6.16: Comparison of the measured spectrum with the total spectra from the baseline calculation and the case with the LBL-VS constrained.

steady. It should be noted that the turbulence cascade means that, even though the dominant length scale is 50m, there will be smaller scales in the flow.

Regardless of the atmospheric turbulence level, the wake will always cause this turbulence level to increase. Assuming that the turbulence intensity in the wake is unlikely to be less than 5%, to achieve the required spectral amplitude this restricts the length scale to be less than 0.4m, which is approximately twice the blade chord length. The implication is that the turbulence parameters are more likely to be due to the wake from the upstream half of the rotor than from atmospheric turbulence. This supports the hypothesis that blade-wake interaction is one of the dominant sources of noise from a VAWT rotor.

6.3.4 Inclusion of Experimental Conclusions

The preliminary predictions were found to deviate significantly from the measured data above 2kHz. The BPM model hugely overestimates the noise radiated by LBL-VS noise, and it was suggested that this was due to the inaccurate assumption that the flow remains steady and attached for the whole revolution of the blades. The experimental investigations had indicated that laminar boundary layer noise was predominantly radiated as the blades travel in the upstream direction. The BPM model was therefore run with the LBL-VS term constrained such that it was only included when the blade was at azimuths between 350°-10°. The input parameters specified in table 6.2 were used in all the calculations described in this section.

A comparison of the measured spectrum with the total spectrum from the baseline calculation and the case with the LBL-VS constrained is presented in figure 6.16. The amplitude of the LBL-VS peak has been reduced to a level consistent with the measured spectra, but is not at the same frequency as the peak in the measured spectrum. The current implementation of the BPM model

(a)   Flow field computed by McIntosh [2009] at TSR=4

(b) Constrained BPM model output
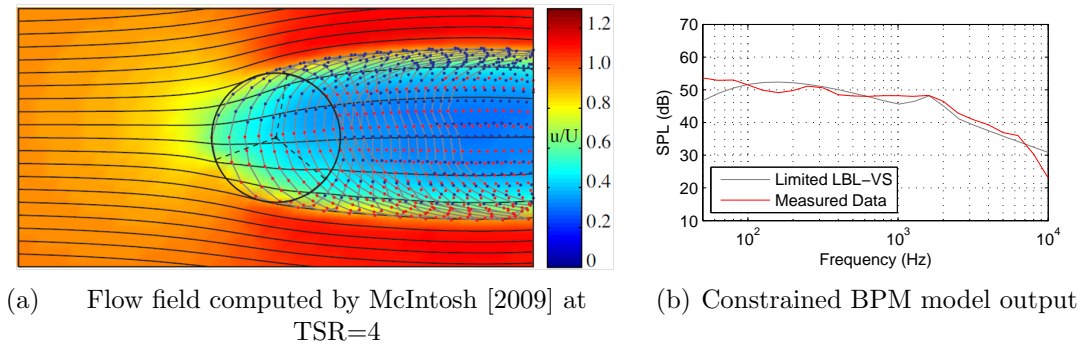
Figure 6.17: Velocity data computed by McIntosh [2009], and the spectra predicting using the constrained LBL-VS location and reduced velocity.

does not account for the effect of the induction factor so a further alteration was made that reduced the free stream velocity used in the computation of the LBL-VS contribution. McIntosh [2009] estimated the effect of induction factor on VAWT operating at TSR=4 using a VTM method (see figure 6.17(a)). Based on his data, a velocity that was 0.6 times the free-stream was used in the calculation of the LBL-VS noise. The results of this calculation are presented in figure 6.17(b).

The spectra in figure 6.17(b) show good agreement between the measured and the predicted data. In particular, the LBL-VS peaks are closely matched in terms of both amplitude and frequency. This highlights the importance of good quality aerodynamic input data for making accurate predictions of noise radiation from a VAWT with this model.

Including more detailed aerodynamic information, such as induction factor effects, into the noise prediction code will clearly have an impact on the other noise sources modelled. For example, when induction effects are included the turbulence inflow parameters would have to be changed to obtain agreement between the measured and predicted spectra. This should not, however, invalidate the conclusion that the rotor wake is the dominant source of inflow turbulence.

6.4   Summary

The harmonic content of the measured spectra motivated the implementation of two models for predicting the sound radiated by periodic blade loading fluctuations. An analytical far-field model was derived, based on the approach of Lowson and Ollerhead [1969]. A simpler result for the harmonic component of the sound field was found, and was shown to produce nearly identical results to the model derived by Lowson and Ollerhead [1969].

For modelling the propagation of sound from the wind tunnel model to the acoustic array, it was shown to be essential to include near-field terms. These were included in a numerical solution of the equations derived by Lowson [1965] for the sound radiated by a moving point force. The numerical model showed that the near-field terms make a significant contribution to the sound field radiated to the nearest microphones in the acoustic array, even at frequencies up to the 50th harmonic of the angular velocity. It was further demonstrated that there was no destructive interference between the near- and far-field components of the sound field, implying that the harmonic noise levels measured by the acoustic array represent an upper bound on the components radiated to the far-field.

The linear relationship between the blade loading harmonics and the sound harmonics meant that it was theoretically possible to estimate the blade loads from the sound harmonics. A numerical study was conducted to assess the feasibility of this inversion process. The limited least squares solution implemented using the convex optimisation package, CVX, developed by Boyd and Vandenberghe [2004], was found to produce good solutions even when significant noise was added to the harmonic components of the microphone spectra. The solution was found to struggle to resolve the amplitude of the lowest harmonics, and singular value decomposition of the transfer matrix showed this to be a fundamental property of the problem, due to the array geometry. In the same way that a larger array improves the low frequency resolution of the beamforming algorithm, a larger array was shown to improve the ability of the inverse method to accurately determine the low frequency blade loading harmonics.

The harmonic analysis highlighted the importance of high resolution blade loading data for making accurate noise predictions using analytical methods, but these data are rarely available. The experimental work had also shown that, apart from at frequencies below 100Hz, the spectra radiated by a full-scale rotor were likely to be dominated by stochastic noise. The harmonic model was therefore of limited use as a predictive tool. Consequently an empirical noise model was developed based on the spectral scaling laws derived by Brooks, Pope, and Marcolini [1989]. The empirical self-noise model implemented was able to produce estimates of the sound field that were in broad agreement with the measured sound spectra. This agreement was only achieved however, when the turbulence parameters were deliberately adjusted to match the predicted and measured spectra, and the model output was found to be sensitive to the exact turbulence statistics used. This model sensitivity allowed information to be inferred about the source however, since it indicated that the inflow turbulence was unlikely to be due to atmospheric turbulence. Instead, the turbulence inflow parameters required to obtain agreement between the measured and predicted spectra suggested that the interaction of the VAWT with its own wake was the source of the inflow turbulence noise.

The inclusion of further information about the sources in the BPM model further improved the predictions made. In the experiments, the LBL-VS source was found to predominantly radiate noise as the blades travelled in the upstream direction. By constraining the LBL-VS source to only radiate in this region, better agreement was found between the measured and predicted spectra. Furthermore, including the effect of induction factor on the velocity experienced by the blades for LBL-VS noise resulted in very good agreement between the measured and predicted spectra in the region of the LBL-VS peak. This result demonstrated that good quality aerodynamic data is necessary to make accurate predictions. At the same time however, it also showed that, if such data is available, the BPM method is capable of estimating the radiated noise.

Chapter 7

Conclusions and Future Work

The aim of this study was to gather noise data from a model-scale VAWT, using an acoustic array to locate and identify the sources of noise. A range of tip speed ratios, rotor solidities and inflow turbulence levels were tested to investigate the impact of these parameters on the radiated noise. In addition to the experimental measurements, the possibility of predicting the noise radiation was examined.

The conclusions from these investigations are summarised below and some guidelines for designing a low noise VAWT rotor are suggested. The chapter concludes with a number of ideas for future work that would significantly aid the understanding of the noise radiation from VAWT rotors.

7.1 Analysis Techniques

Using the conventional beamforming algorithm for investigating the noise from a VAWT had a number of limitations as discussed in chapter 4. It was found that, while not much could be learnt by looking at individual cases, by comparing a series of cases, some general trends in the noise radiation could be clearly observed.

In the presence of uncorrelated noise, the diagonal terms of the cross-spectra matrix can be set to zero to improve the performance of the beamforming algorithm. An alternative method was trialled, which used the Matlab convex optimisation package developed by Boyd and Vandenberghe [2004] to estimate the noise on the diagonal of the CSM, then subtract it to give a noise-free CSM. Beamforming carried out using this technique was seen to give a slight improvement relative to the normal method. It was decided, however, that the improvement in beamforming performance was not sufficient to warrant the significant increase in processing time incurred.

By using the synchronised sampling capability of the VIPER data acquisition system, it was possible to break the microphone signals into a series of blocks corresponding to certain sectors of the rotor's revolution. This allowed the beam-forming algorithm to be used to examine a series of 'snapshots' of the blades as they rotated. For a moving source, which is also unsteady, this was an effective way to separate the different source mechanisms that occur as the blades rotate. Even without accounting for Doppler effects the method was found to work well, and provided useful information about the noise sources on the model VAWT rotor.

One particularly useful feature of the sector beamforming process was that it allowed previously unidentified sources to be located. This was because loud sources, which only occurred at certain blade azimuths, dominated the time-averaged beamforming. When the blades were not at these locations it was possible to identify other quieter sources, such as the noise generated by the spokes.

Spectral analysis, and scaling methods in particular, proved very useful for determining the noise sources. The scaling relationships for trailing edge scattering and laminar boundary layer tonal noise were applied to the measured spectra. By examining the convergence of certain components of the spectra under the application of the scaling it was possible to definitively identify the extent of these two source mechanisms.

7.2 Experimental Results

The first important result from the experiments was the good, qualitative agreement between the broadband spectra measured from the model-scale rotor and those measured from the full-scale QR5 rotor. This result gave confidence that the conclusions drawn from the experiments could be extended to a full-scale rotor, as long as the necessary scaling of the sound sources was carried out.

The experiments revealed a number of different noise source mechanisms on the model VAWT. The characteristics of each of these mechanisms and their extent across the range of operating conditions tested is outlined below.

Dynamic Stall Noise: The beamforming analysis indicated that at low TSR there was a strong source in the upstream half of the rotor that disappeared as the TSR increased. In addition, the TSR at which this source disappeared was found to increase as rotor solidity decreased. This evidence was all consistent with the source being due to dynamic stall on the blades, since this phenomenon was only anticipated at low TSR. Similar

trends were observed in the spectral analysis. In particular, the harmonic content of the spectra was seen to reduce with both increasing TSR and increasing solidity, which implied that the harmonic sound was largely due to periodic, unsteady loading during dynamic stall.

In a smooth inflow, the harmonic peaks in the spectra from the 3-bladed model rotor were observed up to the 40th harmonic of the angular frequency at TSR=3. On the full-scale QR5 rotor at TSR=3 in a wind speed of 10m/s, the 40th harmonic of the angular velocity is at approximately 130Hz.

Laminar Boundary Layer Tonal Noise: Spectral scaling was carried out on the measured 1/3rd octave spectra, according to the method described by Brooks et al. [1989] for predicting laminar boundary layer tonal noise. This scaling process indicated that the broadband peak observer in the spectra of both the full- and model-scale rotors was almost certainly due to this source mechanism. To investigate this further, boundary layer trips were added to the blades, and it was found that a trip on the inner surface of the blades did dramatically reduce the amplitude of the peak.

Both the scaling process and the beamforming analysis indicated that the LBL noise was predominantly radiated as the blades were travelling in the upwind direction. To remove this source the trip was required to be on the pressure surface. The fact that the trip had to be on the inner surface to eliminate the noise source was consistent with the source location identified, since the inner surface was indeed the pressure surface at that location.

Removing the LBL noise made a significant difference to the beamforming analysis since it allowed other, quieter sources to be observed. In combination with the sector beamforming technique, it allowed a relatively complete picture of the sound radiation from the rotating blades to be established. The noise from the spokes as the blades travelled upstream was particularly clearly highlighted.

Trailing Edge Noise: The 1/3rd octave spectra for both the full-scale and model-scale rotor contained a region below 1kHz where the amplitude was shown to scale with the fifth power of the relative blade velocity as they travelled upstream. The theoretical work of Ffowcs Williams and Hall [1970] showed that this scaling is consistent with the scattering of sound from a sharp edge, such as the trailing edge of the blades.

By contrast the LBL noise peak only increased in amplitude with blade velocity to the power 3/2. This means that at high relative blade velocities the trailing edge noise could become the dominant source. This relative scaling is clearly observed in the 1/3 octave spectra shown in figure 5.1,

where the LBL peak nearly falls below the TE noise level for the QR5 rotor when the wind speed is 10m/s.

Blade-Wake Interaction Noise: When laminar boundary layer noise and dynamic stall noise were not dominating the sound field, the strongest source was observed to be in the downstream half of the rotor, as the blades were travelling upwind. It was suggested that this source was due to blade-wake interactions, but in order to explain the detailed behaviour of this source it would be necessary to understand the wake flow in much more detail. The experiments with the wide shaft did confirm, however, that the interaction of the blades with the wake from the rotor shaft has little or no impact on the sound field.

Inflow Turbulence: Inflow turbulence was found to reduce the importance of the harmonic sound due to dynamic stall. It was suggested that this was partly due to the turbulent inflow disrupting the flow over the blades, thereby reducing the amplitude of the sound radiated by periodic blade loading. At the same time the stochastic loading due to the turbulent inflow was seen to increase the levels of broadband sound, thus further reducing the importance of harmonic noise.

The impact of inflow turbulence on the broadband component of the sound was different at different TSR. At low TSR the amplitude of the sound below 1kHz was increased and the strength of the LBL peak was reduced. At high TSR, however, the different levels of inflow turbulence had almost no effect on the spectra. It was suggested that this was because, at high TSR, the wind velocity only has a small impact on the relative velocity of the flow over the blades due to the absolute blade velocity being proportionally greater.

Harmonic versus Broadband Sound: Except at low TSR, the deterministic component of the sound field was found to only extend up to around the 30th harmonic of the rotor angular velocity. In addition, it was shown that the harmonic levels had to be much greater than the broadband level if they were to be the dominant source of radiated sound energy. It was concluded that, on the full-scale QR5 rotor during normal operation, the harmonic sound would probably only be measurable below 100Hz. Due to the low sensitivity of the human ear at such low frequencies, the broadband sound was identified as being the more significant component of the sound field.

7.3 Noise Modelling

Harmonic Noise Models: Two models were developed to predict the harmonic component of the sound field radiated by the fluctuating loads on the blades. The first model was based on the work of Lowson and Ollerhead [1969], and was a purely analytical model of the far-field component of the harmonic sound. By adopting a slightly different approach from earlier studies, a very simple expression for the noise radiated by a periodic, rotating point force was derived. This result was shown to produce results that were almost identical to the more complex earlier result.

A second, numerical method was developed that modelled both the near- and far-field expressions derived by Lowson [1965] for the sound radiated by a moving point force. This model was validated in the far-field by comparison with the analytical method and was found to give good agreement. For modelling the harmonic sound radiated by the wind tunnel model to the acoustic array it was shown that near-field terms needed to be included. One key conclusion from this model was that the total sound field always exceeded the amplitude of its component near- and far-field terms. This implied that the sound amplitudes measured by the acoustic array represented an upper bound on the sound radiated to the far-field.

Analysis of the harmonic models highlighted the necessity of high resolution blade loading data for making accurate predictions of the radiated sound. Since this data is often not available, and due to the limited contribution of deterministic sources to the measured sound field, the harmonic models were found to be of limited use as predictive tools. The linear relationship that was derived between the blade loading harmonics and the sound field harmonics did, however, highlight the possibility of inverting this relationship to estimate the blade loads from the sound field harmonics.

Inverse Model: Measuring or simulating the blade loads to a sufficient level of detail to make accurate sound predictions is not easy. It was suggested that the blade loads could be determined by inverting the expression relating the blade loading harmonics to the sound harmonics measured using the acoustic array.

This approach was implemented in Matlab and was found to work well for a range of simulated test cases, even in the presence of random noise. The best solutions were generated by the 'limited least squares' method, which was implemented using the convex optimisation package developed by Boyd and Vandenberghe [2004]. This method was particularly attractive since, unlike the singular value decomposition method, the limits imposed on the

solution could be easily determined from the physics of VAWT operation.

The inverse method struggled to identify the amplitude of the lower frequency harmonics. Singular value decomposition of the transfer matrix indicated that this was a fundamental property of the way the problem was framed, and it was suggested that this limitation was similar to the low resolution of the beamforming algorithm at low frequencies due to the geometry of the array. A test case was simulated with a double size array, and was found to improve the ability of the inverse method to identify the low frequency harmonic amplitudes, thereby supporting the assumption regarding the importance of array geometry.

Empirical Model: The empirical aerofoil self-noise model of Brooks, Pope, and Marcolini [1989] was implemented along with the turbulence inflow model described by Lowson [1992]. Since these models only account for far-field terms, the predictions were compared with the data measured from the full-scale QR5 rotor. Initial simulations, using very basic aerodynamic data, indicated that it was possible to produce estimates of the spectra that were in agreement with the measured data.

These predictions were contingent on carefully chosen values for the turbulence intensity and length scale. A parametric study was conducted to investigate the sensitivity of the model to these variables and it was shown that the spectral amplitudes were significantly altered by small changes in the turbulence parameters. It was found that this was actually a useful result, as it allowed information to be inferred about the nature of the inflow turbulence. Specifically, it was suggested that the turbulence levels required to obtain agreement between the measured and predicted spectra were unlikely to be due to atmospheric boundary layer turbulence. Instead they were more consistent with those expected in the wake shed by the upstream blades. The implicit conclusion, that blade-wake interaction is a significant source of noise on a full-scale VAWT rotor, is consistent with the results from the model-scale experiments.

The laminar boundary layer noise levels predicted by the BPM model with the basic aerodynamic data were much greater than the measured levels. The experiments had suggested that this source only radiated as the blades were travelling upstream, so the source was subsequently constrained in the model to only radiate at this location. The basic aerodynamics also ignored the impact of induction factor effects, which would reduce the relative velocities experienced by the blades. As such, the laminar boundary layer source was adjusted so that the relative velocity was in line with the value predicted by McIntosh [2009] using a VTM model. With the inclusion

of these extra aerodynamic data the spectra predicted by the BPM model were in much better agreement with the measured data.

The evaluation of the BPM model indicated the importance of good aerodynamic data for making accurate predictions of the radiated sound spectra. It was concluded, however, that if such data is available, then it would be possible to make realistic predictions of the sound radiated by a VAWT rotor.

7.4 Design Recommendations

This section describes some recommendations for designing a low noise VAWT rotor. Some of these suggestions are expected to work unambiguously, while others are more speculative, and further work would be necessary to definitively prove their usefulness.

1. The first design recommendation is to add boundary layer trips to the inner surfaces of the blades. While there might be a slight loss in performance due to the increased drag on the blades, there is the possibility of significant reductions in noise radiation. This will be especially true at lower wind speeds where the laminar boundary layer noise component is relatively more significant.

2. Running the rotor at high TSR appears to be a good option for noise minimisation. High TSR means that dynamic stall noise is avoided and also potentially reduces the impact of turbulent inflow on the aerodynamic and aeroacoustic performance.

3. Blade-wake interaction was identified as a significant source of noise. The simulations of Scheurich [2011] suggested that curving the blade tips in towards the hub could help to reduce the extent of this interaction.

4. At higher wind speeds trailing edge noise becomes more significant. The work of Ffowcs Williams and Hall [1970] showed that the noise is proportional to the fifth power of the *chordwise* velocity. This means that the noise radiated by this mechanism can potentially be reduced by sweeping the blades. It may also be possible to reduce the radiated noise by adding serrated trailing edges to the blades although, at present, the optimal geometry for the serrations is an ongoing area of research.

7.5 Future Work

There are a number of additions and extensions to the current study that would aid the understanding of the sound field of VAWT rotors. Some possible options are listed below:

1. The noise from dynamic stall was found to be a significant component of the sound radiated by a VAWT rotor, particularly at low TSR. At present there is very little information about the noise radiated from an aerofoil that is experiencing dynamic stall, which made it difficult to definitively determine the components of the measured spectra that were due to this mechanism. Identifying the characteristics of the sound radiated during dynamic stall would provide useful information for determining when this type of source is present.

2. In the TSR range that is expected to be near the peak power coefficient, it was found that the downstream blade-wake interaction noise was a strong source. In order to better understand this noise source it would first be necessary to obtain a better understanding of the wake flow. Detailed PIV, LDA or hotwire measurements would provide a very interesting body of data that would hopefully elucidate aspects of both the aerodynamic and aeroacoustic performance.

3. Some ideas about the effect of changing the rotor geometry on the noise output were suggested in chapter 3. It would be interesting to investigate the impact of features such as blade curvature, sweep and preset pitch to establish whether they have the expected impact on the sound-field. If it was established that the tip vortices from the upstream blades were a significant contributor to the blade-wake interaction noise, it would also be interesting to investigate the impact of including some of the advanced blade tip geometries used to reduce helicopter BVI noise.

4. It has been shown that it is possible to obtain good quality acoustic array data from a full-scale HAWT (e.g. Oerlemans et al. [2007]). Now that beamforming has been shown to be effective for investigating the noise sources on a VAWT, it would be interesting to attempt similar array measurements on a full-scale VAWT.

5. Sector beamforming was shown to be a useful tool for examining the sound field radiated by the unsteady, moving sources on a VAWT rotor. This method could be improved by using a source model in the beamforming process that accounted for the effects of Doppler shift and amplification.

Better results might also be obtained by accounting for the propagation time from the blades to the microphones, as this would potentially improve the correlation between the microphone signals.

6. VAWTs have often been installed on the roofs of buildings, where the limited space available means that they may be closely spaced. There is the possibility that one turbine may be operating in the wake of another, and this may have implications for noise generation. Once the noise sources on a single rotor are better understood, it may be useful to investigate the noise resulting from rotor to rotor interaction.

Appendices

Appendix A

Derivation of Rotating Harmonic Model

The starting point for the re-derivation of the rotating harmonic model was the expression given by Lowson [1965] for the far-field acoustic density fluctuations due to a moving point force (Eq.2.5), which is repeated below.

$$\rho - \rho_0 = \left[\frac{x_i - y_i}{4\pi a_0^2 r^2 (1 - M_r)^2} \left\{ \frac{\partial F_i}{\partial t} - \frac{F_i}{1 - M_r} \frac{\partial M_r}{\partial t} \right\} \right]_{ret} \tag{2.5}$$

Note that in all the subsequent expressions τ is the retarded time coordinate and t is the observer time coordinate.

The force components were defined using the Fourier series $F_i(\tau)$ where $i = 1, 2, 3$ are the three Cartesian axes. To avoid confusion, imaginary numbers are denoted by j.

$$F_i(\tau) = \sum_{\lambda = -\infty}^{\infty} c_{\lambda i} e^{j\lambda\Omega\tau} \tag{A.1}$$

$$\frac{\partial F_i(\tau)}{\partial \tau} = \sum_{\lambda = -\infty}^{\infty} c_{\lambda i} j\lambda\Omega e^{j\lambda\Omega\tau} \tag{A.2}$$

The equation for the density fluctuation, $\rho - \rho_0$, was then integrated to find the Fourier coefficients for the sound field harmonics. This Fourier integral was

converted to retarded time coordinates using the two relationships presented below,

$$t = \tau + r/a_0$$
$$dt = d\tau(1 - M_r) \tag{A.3}$$

Putting all of these components together the intermediate result for the nth harmonic of the sound field is:

$$c_n = \frac{\Omega}{8\pi^2 a_0^3} \int\limits_0^{2\pi/\Omega} \frac{(x_i - y_i)}{(1 - M_r)r^2} \sum_{\lambda=-\infty}^{\infty} c_{\lambda i} e^{j\lambda\Omega\tau} \left\{ j\lambda\Omega - \frac{1}{1 - M_r}\frac{\partial M_r}{\partial \tau} \right\} \times$$
$$e^{-jn\Omega(\tau + r/a_0)} d\tau \tag{A.4}$$

At this point, the far-field assumption $r \gg R$ was introduced in order to facilitate an analytic solution.

$$r = r_1 - \frac{RY}{r_1}\cos(\theta - \phi) \qquad \text{(in the phase term)}$$
$$r = r_1 \qquad \text{(in the magnitude term)}$$
$$M_r = -\frac{Y M_B}{r_1}\sin(\theta - \phi)$$
$$\frac{\partial M_r}{\partial \tau} = -\frac{Y M_B}{r_1}\cos(\theta - \phi)\Omega$$

where r_1 is the distance from the hub to the observer location, $\theta = \Omega\tau$ is the blade azimuthal location, ϕ is the angle to the observer in the horizontal plane, R is the rotor radius, M_B is the blade Mach number and Y is the horizontal distance from the hub to the observer (see figure A.1). Since it has been assumed that $r = r_1$ in the far field, at the same order of approximation $x_i - y_i \approx x_i$.

The integral was then redefined in angular coordinates rather than time coordinates using the following change of variable.

$$d\tau = \frac{d(\Omega\tau - \phi)}{\Omega} \tag{A.5}$$
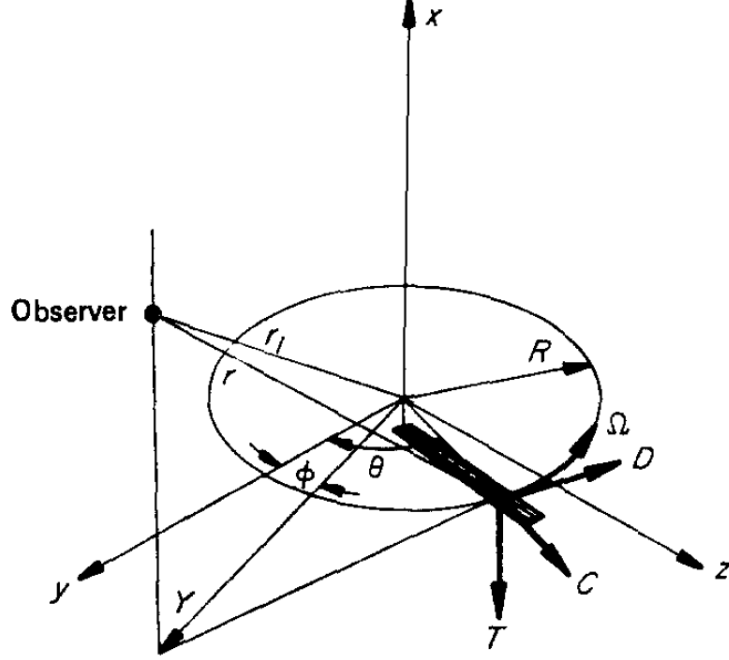
Figure A.1: Schematic of the geometric parameters used by Lowson and Ollerhead [1969] in their rotating harmonics model

To simplify the final integral the following variables were defined:

$$k = \frac{e^{-jn\Omega\frac{r_1}{a_0}+j(\lambda-n)\phi}}{8\pi^2 a_0^3 r_1^2}$$

$$\alpha = \Omega\tau - \phi$$

$$A = \frac{YM_b}{r_1}$$

The final integral then became the following:

$$c_n = \int_0^{2\pi} \frac{x_i}{(1 + A\sin\alpha)} \sum_{\lambda=-\infty}^{\infty} kc_{\lambda i}e^{j[\alpha(\lambda n)+nA\cos\alpha]}\left\{j\lambda\Omega + \frac{A\Omega\cos\alpha}{1 + A\sin\alpha}\right\}d\alpha \quad \text{(A.6)}$$

Integration was performed by separating out the second term in the integral and solving it independently and then substituting it back into the original

equation. This term was integrated by parts and the resulting integral term was substituted back into the original integral, equation A.6. After some rearrangement this gave:

$$c_n = \int_0^{2\pi} \sum_{\lambda=-\infty}^{\infty} kc_{\lambda i} x_i j\Omega n e^{j[\alpha(\lambda n)+nA\cos\alpha]} d\alpha$$

This equation was then solved using the following Bessel function identity, which is a rearrangement of equation 9.1.21 of Abramowitz and Stegun [1965, p.360]:

$$J_m(z) = \frac{1}{2\pi j^m} \int_0^{2\pi} e^{j[m\phi+z\cos\phi]} d\phi$$

The final result for the far-field sound harmonics radiated by a rotating point force was as follows:

$$c_n = \sum_{\lambda=-\infty}^{\infty} 2\pi kc_{\lambda i} x_i \Omega n j^{(\lambda-n+1)} J_{(\lambda-n)}(nA) \tag{A.7}$$

References

M. Abramowitz and I.A. Stegun. *Handbook of Mathematical Functions: with formulas, graphs, and mathematical tables.* Dover, New York, sixth edition, 1965. ISBN 0486612724. 160

MH Akbari and SJ Price. Simulation of dynamic stall for a naca 0012 airfoil using a vortex method. *Journal of Fluids and Structures*, 17:855–874, 2003. 39

RK Amiet. Acoustic radiation from an airfoil in a turbulent stream. *Journal of Sound and Vibration*, 41(4):407–420, August 1975. 20, 21, 23, 137

RK Amiet. Noise due to turbulent flow past a trailing edge. *Journal of Sound and Vibration*, 47(3):387–393, 1976. 16, 79

H Arbey and J Bataille. Noise generated by airfoil profiles placed in a uniform laminar flow. *Journal of Fluid Mechanics*, 134:33–47, 1983. ix, 17

RH Bakker, E Pedersen, GP van den Berg, RE Stewart, W Lok, and J Bouma. Impact of wind turbine sound on annoyance, self-reported sleep disturbance and psychological distress. *Science of the total Environment*, 425:42–51, 2012. 7

T Beddoes and J Leishman. A semi-empirical model for dynamic stall. *Journal of the American Helicopter Society*, 34, 1989. 39

D. E. Berg, editor. *Improved double-multiple streamtube model for the Darrieus-type vertical axis wind turbine*, 1983. 39

A. Betz. *Wind-Energie und ihre Ausnützung durch Windmühlen.* Ökobuch-Reprint. ökobuch, 1926. ISBN 9783922964117. 3

V Blandeau. *Aerodynamic Broadband Noise from Contra-Rotating Open Rotors.* PhD thesis, University of Southampton, Faculty of Engineering and the Environment, March 2011. 16

K Boorsma and Schepers. Enhanced wind turbine noise prediction tool SILANT. In *4th International Wind Turbine Noise Conference, Rome*, 2011. 20, 23

S Boyd and L Vandenberghe. *Convex Optimization*. Cambridge University Press, first edition, 2004. 70, 131, 145, 147, 151

A Brocklehurst and AC Pike. Reduction of BVI noise using a vane tip. In *American Helicopter Society Aeromechanics Specialists Conference*, San Francisco, CA, 1989. ix, 29, 30

T Brooks. Studies of blade-vortex interaction noise reduction by rotor blade modification. *NASA STI/Recon Technical Report A*, 959:90093, 1993. ix, 29

T Brooks and CL Burley. Rotor broadband noise prediction with comparison to model data. In *AIAA Paper*, number 2210, 2001. 24

T Brooks, S Pope, and M Marcolini. Airfoil self-noise and prediction. NASA Reference Publication 1218, NASA, July 1989. iv, ix, 18, 19, 21, 23, 32, 79, 81, 105, 106, 120, 137, 145, 149, 152

KT Brown. Measurements of the noise characteristics of the qr5 wind turbine. Consultancy Report 7644-R01, ISVR Consulting, 2007. 92

R Brown. Rotor wake modelling for flight dynamic simulation of helicopters. *AIAA Journal*, 38(1):57–63, 2000. 53

R Brown and A Line. Efficient high-resolution wake modeling using the vorticity transport equation. *AIAA Journal*, 43:1434–1443, July 2005. doi: 10.2514/1. 13679. 53

LW Carr, KW McAlister, and WJ McCroskey. Analysis of the development of dynamic stall based on oscillating airfoil experiments. NASA Technical Note TN D-8382, Ames Research Center and US Army Air Mobility Research and Development Laboratory, Moffett Field, Calif. 94035, 1977. 36, 37

M Castelli, A Villa, and E Bernini. CFD Analysis of the Influence of Central Shaft on Vertical Axis Wind Turbine Noise Emission. In *International Wind Turbine Noise Conference, Rome*, 2011. x, 52, 56

M Castelli, S De Betta, and E Bernini. Effect of blade number on a straight-bladed vertical axis wind turbine. *World Academy of Science, Engineering and Technology*, 61:305–311, 2012. 87

T.Y. Chen and L.R. Liou. Blockage corrections in wind tunnel tests of small horizontal-axis wind turbines. *Experimental Thermal and Fluid Science*, 35(3):565 – 569, 2011. ISSN 0894-1777. doi: 10.1016/j.expthermflusci. 2010.12.005. URL http://www.sciencedirect.com/science/article/pii/ S0894177710002438. 60

TP Chong, PF Joseph, and M Gruber. Airfoil noise reduction by non-flat plate type trailing edge serrations. *Applied Acoustics*, 74:607–613, 2013. 17, 26

FN Coton, RA Galbraith, and D Jiang. The influence of detailed blade design on the aerodynamic performance of straight-bladed vertical axis wind turbines. In *Proceedings of the Institution of Mechanical Engineers, Part A: Journal of Power and Energy*, volume 210, pages 65–74, 1996. 47, 48

N Curle. The influence of solid boundaries upon aerodynamic sound. *Proceedings of the Royal Society (London)*, A(231):505–514, 1955. 11

L Danao. *The Influence of Unsteady Wind on the Performance and Aerodynamics of Vertical Axis Wind Turbines*. PhD thesis, University of Sheffield Department of Mechanical Engineering, 2012. 51, 52

AP Dowling and JE Ffowcs Williams. *Sound and Sources of Sound*. Ellis Horwood, first edition, 1983. 73

SJC Dyne. Wind turbine noise measurements. Consultancy Report 7837-R01, ISVR Consulting, December 2007. 142

J Edwards. *The Influence of Aerodynamic Stall on the Performance of Vertical Axis Wind Turbines*. PhD thesis, University of Sheffield Department of Mechanical Engineering, August 2012. x, 40, 41, 43, 106

J Edwards, L Danao, and R Howell. Novel experimental power curve determination and computational methods for the performance analysis of vertical axis wind turbines. *Journal of Solar Energy Engineering*, 134(031008), 2012. 40, 42, 45

JA Ekaterinaris and MF Platzer. Computational prediction of airfoil dynamic stall. *Progress in Aerospace Sciences*, 33:759–846, 1997. 39

ESDU. *Characteristics of Atmospheric Turbulence Near the Ground*. Engineering Sciences Data Unit, 1974. URL http://books.google.co.uk/books?id= kNO7GwAACAAJ. 23

F Farassat. Derivation of Formulations 1 and 1A of Farassat. Technical Memorandum TM-2007-214853, NASA, 2007. 14, 15

F Farassat and GP Succi. Theory of noise generation from moving bodies with and application to helicopter rotors. Technical Report R-451, NASA, 1975. 14

F Farassat and GP Succi. A review of propeller discrete frequency noise prediction technology with emphasis on two current methods for time domain calculations. *Journal of Sound and Vibration*, 71(3):399–419, February 1980. 14

C Ferreira. *The near wake of the VAWT: 2D and 3D views of the VAWT aerodynamics.* PhD thesis, Technische Universiteit Delft, 2009. 6, 36, 40, 51, 53

C Ferreira, H Bijl, G van Bussel, and G van Kuik. Simulating dynamic stall in a 2d vawt: Modeling strategy, verification and validation with particle image velocimetry data. In *Journal of Physics: Conference Series*, volume 75, 2007. 39

JE Ffowcs Williams and LH Hall. Aerodynamic sound generation by turbulent flow in the vicinity of a scattering half plane. *Journal of Fluid Mechanics*, 40 (4):657–670, 1970. 15, 80, 149, 153

JE Ffowcs Williams and DL Hawkings. Sound generation by turbulence and surfaces in arbitrary motion. *Philosophical Transactions of the Royal Society of London*, 264(A1151):321–342, 1969. 13

MR Fink and DA Bailey. Airframe noise reduction studies and clean-airframe noise investigation. Technical Report NASA-CR-159311, NASA, 1980. 20

P Fuglsang and H A Madsen. Implementation and verification of an aeroacoustic noise prediction model for wind turbines. RISO Report R-867(EN), RISO, Riso National Laboratory, Roskilde, Denmark, March 1996. 20, 21, 23

N Fujisawa and S Shibuya. Observations of dynamic stall on darrieus wind turbine blades. *Journal of Wind Engineering and Industrial Aerodynamics*, 89(2):201–214, February 2001. x, 40

H. Glauert. *The Analysis of Experimental Results in the Windmill Brake and Vortex Ring States of an Airscrew.* Reports and memoranda. H.M. Stationery Office, 1926. URL `http://books.google.co.uk/books?id=_JfFtgAACAAJ`. 50

H. Glauert. *The Elements of Aerofoil and Airscrew Theory.* Cambridge Science Classics. Cambridge University Press, 1948. ISBN 9780521274944. 50

SAL Glegg, SM Baxter, and AG Glendinning. The prediction of broadband noise from wind turbines. *Journal of Sound and Vibration*, 118(2):217–239, 1986. 16, 21, 22, 23

FR Hama. An efficient tripping device. *Journal of the Aeronautical Sciences*, 24: 236–237, March 1957. 62

R Howell, N Qin, J Edwards, and N Durrani. Wind tunnel and numerical study of a small vertical axis wind turbine. *Renewable Energy*, 35:412–422, 2010. 60

DS Jones. *The Theory of Electromagnetism.* Pergamon Press, 1964. 14

JC Kaimal, JC Wyngaard, Y Izumi, and OR Coté. Spectral Characteristics of Surface Layer Turbulence. *Quarterly Journal of the Royal Meteorological Society*, 98, 1972. 142

M Kamruzzaman, TH Lutz, K Nuebler, and E Kraemer. Implementation and verification of an aeroacoustic wind turbine blade analysis tool. In *International Wind Turbine Noise Conference, Rome*, 2011. 23

MJ Kingan and JR Pearse. Laminar boundary layer instability noise produced by an aerofoil. *Journal of Sound and Vibration*, 322:808–828, 2009. 17

B K Kirke. *Evaluation of Self-starting Vertical Axis Wind Turbines for Stand-alone Applications.* PhD thesis, Griffith University, Australia, 1998. x, 44

PC Klimas. Tailored airfoils for vertical axis wind turbines. Sandia Report SAND84-1062, Sandia National Laboratories, February 1992. 45

PC Klimas and M Worstell. Effects of blade preset pitch/offset on curved-blade Darrieus vertical axis wind turbine performance. Technical Report SAND-81-1762, Sandia National Laboratories, October 1981. 47

J Leishman. Dynamic stall experiments on the NACA 23012 aerofoil. *Experiments in Fluids*, 9:49–58, 1990. 39

J Leishman. *Principles of Helicopter Aerodynamics, Second Edition.* Cambridge University Press, 2006. x, 36, 38, 49

MJ Lighthill. On Sound Generated Aerodynamically I. Fundamental Theory. *Proceedings of the Royal Society (London)*, 211:564–587, 1952. 10, 13

MJ Lighthill. Sound Generated Aerodynamically (Bakerian Lecture). *Proceedings of the Royal Society London A*, 267:147–182, 1962. 12

MV Lowson. The sound field for singularities in motion. *Proceedings of the Royal Society (London)*, A286:559–572, 1965. 12, 13, 21, 27, 31, 32, 120, 121, 123, 127, 145, 151, 157

MV Lowson. Assessment and prediction of wind turbine noise. Contractor Report ETSU W/13/00284/REP, Flow Solutions, 1992. 137, 152

MV Lowson. A new prediction model for wind turbine noise. *Wind Engineering*, 18(2):51–61, 1994. 21, 23

MV Lowson. Focusing of helicopter BVI noise. *Journal of Sound and Vibration*, 190(3):477–494, February 1996. 29

MV Lowson and JB Ollerhead. A theoretical study of helicopter noise. *Journal of Sound and Vibration*, 9(2):197–222, 1969. xii, xiii, 27, 29, 31, 121, 122, 144, 151, 159

C Masson, C Leclerc, and I Paraschivoiu. Appropriate dynamic-stall models for performance predictions of vawts with nlf blades. *International Journal of Rotating Machinery*, 4(2):129–139, 1998. 39

WJ McCroskey. Measurement of boundary layer transition, separation and streamline direction on rotating blades. Technical Note TN D-6321, NASA, April 1971. 17

WJ McCroskey, KW McAlister, and LW Carr. An Experimental Study of Dynamic Stall on Advanced Airfoil Sections Volume 1. Summary of the Experiment. Technical Memorandum 84245, NASA, 1982. 46

S McIntosh. *Wind Energy for the Built Environment.* PhD thesis, University of Cambridge, June 2009. x, xiii, 3, 20, 21, 36, 38, 39, 42, 45, 46, 49, 53, 88, 142, 144, 152

S McIntosh, H Babinsky, and T Bertenyi. Convergence failure and stall hysteresis in actuator-disk momentum models applied fo vertical axis wind turbines. *Journal of Solar Energy Engineering*, 131, August 2009. 51

PJ Moriarty and AC Hansen. AeroDyn theory manual. Technical Report TP-500-36881, NREL, January 2005. 50

PJ Moriarty and P Migliore. Semi-empirical aeroacoustic noise prediction code for wind turbines. Technical Paper TP-500-34478, NREL, 2003. 20

PJ Morris, LN Long, and KS Brentner. An aeroacoustic analysis of wind turbines. In *42nd AIAA Aerospace Sciences Meeting and Exhibit*, number 1184. Penn State University, January 2004. 23

S Oelermans, M Fisher, T Maeder, and K Kögler. Reduction of wind turbine noise using optimized airfoils and trailing-edge serrations. Technical Paper NLR-TP-2009-401, NLR, 2009. 26

S Oerlemans, P Sijtsma, and B Mendez-Lopez. Location and quantification of noise sources on a wind turbine. *Journal of Sound and Vibration*, 299(4-5): 869–883, February 2007. ix, 15, 24, 25, 26, 32, 154

I Paraschivoiu. Aerodynamic loads and performance of the darrieus rotor. *Journal of Energy*, 7:610–615, 1981. 51

I Paraschivoiu. *Wind Turbine Design: With Emphasis on Darrieus Concept.* Polytechnic International Press, 2002. 6

I. Paraschivoiu and A. Allet. Aerodynamic analysis of the Darrieus wind turbines including dynamic-stall effects. In *IECEC '87; Proceedings of the Twenty-second Intersociety Energy Conversion Engineering Conference*, pages 911–917, 1987. 39

RW Paterson and RK Amiet. Noise of a model helicopter rotor due to ingestion of isotropic trubulence. *Journal of Sound and Vibration*, 85(4):551–577, 1982. 62

RW Paterson, PG Vogt, and MR Fink. Vortex noise of isolated airfoils. *Journal of the Aircraft*, 10(5):296–302, May 1973. 16, 17, 18, 20, 81, 105, 107

E Pederson and KP Waye. Perception and annoyance due to wind turbine noise - a dose-response relationship. *Journal of the Acoustical Society of America*, 116(6):3460–70, 2004. ix, 7

L Prandtl. Tragflügeltheorie. *I. Mitteilung. Nachrichten der Königlichen Gesellschaft der Wissenschaften Göttingen, Math-Phys. Klasse*, pages 451–477, 1918. 53

WH Press, SA Teukolsky, WT Vetterling, and BP Flannery. *Numerical Recipes in C - The Art of Scientific Computing.* Cambridge University Press, second edition, 1992. 131

A Quayle. *Landing Gear for Silent Aircraft.* PhD thesis, University of Cambridge, 2008. xi, 58, 68, 71, 73, 76

Rakesh C Ramachandran and Ganesh Raman. Evaluation of various beamforming algorithms for wind turbine noise measurement. *49th AIAA Aerospace Sciences Meeting*, Orlando, Florida(AIAA 2011-722), January 2011. 23

Renewable UK. *Small and Medium Wind: UK Market Report.* April 2012a. URL `http://www.renewableuk.com/en/publications/reports.cfm/SMMR2012`. 2

Renewable UK. *Wind Energy in the UK: State of the Industry Report.* October 2012b. URL `http://www.renewableuk.com/en/publications/reports.cfm/SMMR2012`. ix, 2

Renewable UK. UK Wind Energy Database, 2013. URL `http://www.renewableuk.com/en/renewable-energy/wind-energy/uk-wind-energy-database/`. 2

F Scheurich. *Modelling the Aerodynamics of Vertical-Axis Wind Turbines.* PhD thesis, University of Glasgow, School of Engineering, September 2011. x, xiii, 6, 36, 48, 53, 54, 55, 56, 96, 128, 129, 132, 153

MT Schiff, SR Magari, CE Smith, and AC Rohr. Evaluation of wind turbine-related noise in western New York State. In *Internoise 2012, 19-22 August, New York City*, number IN12-323, 2012. 7

RH Schlinker and RK Amiet. Helicopter rotor trailing edge noise. Contractor Report 3470, NASA, October 1981. 16, 21

FH Schmitz and YH Yu. Helicopter impulsive noise: Theoretical and experimental status. *Journal of Sound and Vibration*, 109(3):361–422, 1986. 27, 28, 53

HC Shin, WR Graham, P Sijtsma, C Andreou, and AC Faszer. Implementation of a phased microphone array in a closed-section wind tunnel. *AIAA Journal*, 45(12):2897–2909, December 2007. 58, 68, 76

GA Shockey, JW Williamson, and CR Cox. Helicopter aerodynamics and structural loads survey. In *American Helicopter Society, 32nd Annual National Forum*, pages 1060–1 to 1060–10, Washington DC, 1976. American Helicopter Society. 30

P Sijtsma. Experimental techniques for identification and characterisation of noise sources. Technical Paper NLR-TP-2004-165, NLR, 2004a. 58, 59

P Sijtsma. Elements of acoustic array data processing. Technical Report NLR-TR-2006-440, NLR, 2004b. 79

P Sijtsma, S Oerlemans, and H Holthusen. Location of rotating sources by phased array measurements. Technical Report NLR-TP-2001-135, NLR, National Aerospace Laboratory NLR, 8300 AD Emmeloord, The Netherlands, 2001. ix, 24, 26, 67, 77

S Sinayoko, M Kingan, and A Agarwal. Trailing edge noise theory for rotating blades in uniform flow. *Proceedings of the Royal Society London A*, pages 1–27, January 2013. 22, 138, 139

BO Sondergaard. Testing the new version of iec 61400-11. In *4th International Wind Turbine Noise Conference, Rome*, 2011. 24

JH Strickland. The Darrieus Turbine: A Performance Prediction Model Using Multiple Streamtubes. Technical Report SAND75 0431, Sandia National Laboratories, 1975. 51

JH Strickland, T Smith, and K Sun. A vortex model of the Darrieus turbine: an analytical and experimental study. Technical Report SAND81-7017, Sandia National Laboratories, 1981. 53

SM Swanson, SA Jacklin, SA Blaas, G Niesl, and R Kube. Acoustic results from a full-scle wind tunnel test, evaluating individual blade control. In *51st Annual Forum of the American Helicopter Society*, Fort Worth, TX, 1995. 31

A Tadamasa and M Zangeneh. Numerical prediction of wind turbine noise. *Renewable Energy*, 36:1902–1912, January 2011. 23

CKW Tam. Discrete tones of isolated airfoils. *Journal of the Acoustical Society of America*, 55(6):1173–1177, 1974. 16, 17

J Taylor. *The Characteristics and Perception of Small Wind System Noise*. PhD thesis, University of Nottingham, 2011. 7

RJ Templin. The NRC Double Multiple Streamtube Theory for Vertical Axis Wind Turbines. Technical Report TM WE 023, National Research Council of Canada, 1985. 51

H Tennekes and JL Lumley. *A First Course in Turbulence*. The Massachusetts Institute of Technology, 1972. ISBN 978-0-262-2019-6. 90

AF Tinetti. *On the Use of Surface Porosity to Reduce Wake-Stator Interaction Noise*. PhD thesis, Virginia Polytechnical Institute and State University, September 2001. 30

KKY Tsang, RMC So, RCK Leung, and XQ Wang. Dynamic stall behaviour from unsteady force measurements. *Journal of Fluids and Structures*, 24:129–150, 2008. 39, 41

UK Department of Energy and Climate Change. *The Carbon Plan: Delivering our low carbon future.* December 2011. URL https://www.gov.uk/government/uploads/system/uploads/attachment_data/file/47613/3702-the-carbon-plan-delivering-our-low-carbon-future.pdf. 1

UK Department of Energy and Climate Change. *Energy Trends.* A National Statistic Publication, December 2012. URL https://www.gov.uk/government/publications/energy-trends-december-2012. 1

UK Government. *Climate Change Act 2008.* Number pt. 27. Stationery Office, 2008. ISBN 9780105427087. URL http://www.legislation.gov.uk/ukpga/2008/27/pdfs/ukpga_20080027_en.pdf. 1

HMM van der Wal and P Sijtsma. Flap noise measurements in a closed section wind tunnel with a phased array. Technical Report NLR-TP-2001-632, NLR, 2001. xi, 69

S Wang, DB Ingham, L Ma, M Pourkashanian, and Z Tao. Numerical investigation on dynamic stall of low reynolds number flow around oscillating airfoils. *Computers and Fluids*, 39:1529–1541, 2010. 39, 40, 51

GR Whitehouse, AH Boschitsch, MJ Smith, CE Lynch, and Richard Brown. Investigation of mixed element hybrid grid-based CFD methods for rotorcraft flow analysis. In *American Helicopter Society, 66th Annual Forum*, Phoenix, AZ, 11-13 May 2010. 53

SE Wright. Sound radiation from a lifting rotor generated by assymetric disk loading. *Journal of Sound and Vibration*, 9(2):223–240, 1969. 31

SE Wright. Discrete radiation from rotating periodic sources. *Journal of Sound and Vibration*, 17(4):437–498, 1971. 32, 130, 136

S Xue, J Wu, and M Summers. Integrated airfoil/blade aeroacoustics modelling and validation. In *International Wind Turbine Noise Conference, Rome*, 2011. 23

YH Yu, B Gmelin, W Splettstoesser, JJ Philippe, JP, and T Brooks. Reduction of helicopter blade-vortex interaction noise by active rotor control technology. *Progress in Aerospace Sciences*, 33:647–687, 1997. 30